The Dissertation Committee for Manasi Doshi
certifies that this is the approved version of the following dissertation:

Computational Design of Carbon Nanotube Sensors for Gas Phase Explosives Detection

Committee:

Eric P. Fahrenthold, Supervisor

Dragan Djurdjanovic

Kamy Sepehrnoori

Eric Taleff

Yuanyue Liu

Computational Design of Carbon Nanotube Sensors for Gas Phase Explosives Detection

by

Manasi Doshi

DISSERTATION

Presented to the Faculty of the Graduate School of

The University of Texas at Austin

in Partial Fulfillment

of the Requirements

for the Degree of

DOCTOR OF PHILOSOPHY

THE UNIVERSITY OF TEXAS AT AUSTIN

August 2021

Dedicated to

my grandparents.

Acknowledgments

First and foremost, gratitude to my advisor, Dr. Eric Fahrenthold without whom this research would never have reached fruition. His constant advice, support and guidance were cardinal throughout my PhD, for research as well as for personal growth. Among the many things that I learned from him are discipline, persistence and humility.

Gratitude to my dissertation committee members: Dr. Eric Taleff, Dr. Kamy Sepehrnoori, Dr. Yuanyue Liu, and Dr. Dragan Djurdjanovic for their patience and guidance.

I am thankful to my parents for encouraging me to pave my own career path and for supporting every life decision I make; to my sister for pushing me to apply to UT and for always being there for me; to Harshal for dealing with my hunger pangs and tantrums; and to my cats Euclid, Luna and Moony for ensuring that I manage my schedule according to their meal times.

This research was supported by the Office of Naval Research (Grant numbers N00014-16-2357 and N00014-20-1-2465). Computer time support was provided by the Texas Advanced Computing Center at the University of Texas at Austin and the Department of Defense High Performance Computing Modernization Program.

Computational Design of Carbon Nanotube Sensors for Gas Phase Explosives Detection

Publication No. _____

Manasi Doshi, Ph.D.
The University of Texas at Austin, 2021

Supervisor: Eric P. Fahrenthold

Gas phase detection of explosive molecules is a sensing application of wide interest. Light weight, low power sensors are needed for mobility and wide dissemination, however low vapor pressures and the presence of similar functional groups in a variety of explosive molecules make the development of sensitive and selective detection systems difficult. Experimental research has reported some success in the development of carbon nanotube based explosives sensors, however safety considerations and strict controls on the distribution of explosive materials hamper experimental progress. In this dissertation, ab initio computational models are developed for metallic and semiconducting carbon nanotube sensors, in a variety of device configurations. Their chemiresistive sensing performance is investigated in the detection of three common explosives. The effects of doping, lattice defects, and functionalizations on

sensing performance are analyzed. Their performance in sensor arrays is also analyzed; array selectivity is improved by capitalizing upon the nonlinear current-voltage characteristics of the CNT sensors. A new ab initio molecular dynamics formulation is developed, for spin polarized systems. It employs a novel nonholonomic Hamiltonian modeling methodology to couple a quantum model of the electronic structure to a molecular model of the nuclear dynamics, and quantifies the modeled nanoscale systems interaction with the external thermal and electromagnetic environment. This theoretical model offers future opportunities for the simulation of finite temperature dynamics in carbon nanotube based sensors, under applied electric and magnetic fields.

Table of Contents

List of Tables

List of Figures

Chapter 1

Introduction

1.1 Motivation

Advances in sensing systems for gas phase detection of explosives are of wide military and security interest; however, the design of explosives sensors is a particularly complex and challenging task. Experiments on explosive gas sensing are difficult, since explosives are both hazardous materials and controlled materials. Light weight, low power sensors are needed to replace the bulky and expensive sensing devices now in common use. Since carbon nanotubes (CNTs) have a high surface area per unit mass, they are attractive candidates for light weight, low power gas sensors. Published experimental studies have tested carbon nanotube based devices in gas sensing applications, and reported considerable success in detecting a wide range of molecules.

In published experiments, Chen et al. [1] fabricated field effect transistors (FETs) using single walled carbon nanotubes on a polyethylene coated fabric substrate with titanium and palladium electrodes. These FETs were employed as chemiresistive sensors to detect TNT vapor. Zhang et al. [2] fabricated thin films of carbon nanotubes coated in Tg-Car (carbazolylethynylene) oligomer and used the thin films as chemiresistive sensors for NT (4-

nitrotoluene), DNT (2,4- dinitrotoluene) and TNT (2,4,6-trinitrotoluene). They showed good sensitivity, especially towards NT. Wei et al. [3] functionalized single walled carbon nanotubes with PMA (1-pyrenemethylamine) and used them as chemiresistive sensors for TNT in water. They showed good sensitivity and very quick response time for TNT sensing.

Recognizing the difficulties of a purely experimental approach to explosive sensors design, this dissertation develops a complimentary, computational approach to the design of CNT based sensor arrays for the trace detection of explosives. The approach combines ab initio analysis of the chemiresistive sensing performance of individual nanotubes, including metallic and semiconducting types, in a variety of sensing configurations, with principal component analysis of their collective performance when deployed as a sensing array.

The computational results suggest that CNT based sensing arrays can: (a) distinguish common background gases from both nitroaromatic and nitramine explosives, (b) distinguish between nitroaromatic and nitramine explosives, and (c) distinguish similar nitramine explosives from each other. These results indicate that CNT based sensing offers important opportunities for future experimental research, and suggests the sensor types, configurations, and array compositions that may lead to fundamental improvements in explosive detection systems.

Although the modeling results described here demonstrate the utility of computational research, as a complement to experiment, in the development of new explosive sensors, it is also the case that improved computational models

are needed. In particular, there is a strong need to extend nanoscale computer aided sensor design to the finite temperature domain. This dissertation develops a new formulation of ab initio molecular dynamics, for spin polarized systems, for future research in the study of mixed energy domain dynamics of explosive sensors. The theoretical formulation is complete; numerical implementation will support future research on finite temperature based sensor design under electromagnetic loading.

1.2 Computational details

The ab initio modeling work described in this dissertation employed the 4.0 version of the open source code suite SIESTA [4]. SIESTA incorporates a Kohn-Sham self-consistent density functional theory (DFT) formulation, which is used to compute equilibrium configurations for the modeled systems. It uses norm-conserving (fully nonlocal) Kleinman-Bylander pseudopotentials and employs linear combination of atomic orbitals (LCAO) basis sets. The matrix elements of the Hartree and exchange-correlation potentials are calculated by projecting the electron wavefunctions and density onto a real-space grid. SIESTA is an order-N method for which the computational time and memory are linearly related to the size of the system.

In this dissertation, exchange correlations for the equilibrium and conductance calculations were obtained using a generalized gradient approximation (GGA) method parameterized by Perdew-Burke-Ernzerhof (PBE). A double-zeta polarized (DZP) basis set was used for all of the atoms. All of

the modeling results were computed at zero temperature. The k-grid mesh for equilibrium calculations was $1 \times 1 \times 1$, while that for the transport calculations was $1 \times 1 \times 5$. The k-points for the Brillouin zone were sampled using a Monkhorst-Pack mesh with a cutoff energy of 300 Ry. Convergence was defined by setting the force tolerance to 0.04 eV Å^{-1}. In the non-transport directions, the computational supercell boundaries were set at least 20Å away from the closest scattering zone nucleus, in order to avoid interactions with neighboring supercells.

The electrical transport properties of the modeled systems were determined using the TranSIESTA [5] module of the SIESTA code suite, which employs a non-equilibrium Greens function (NEGF) method to compute the quantum conductance [6]

$$G = G_0 \int (-\frac{\partial f\,(E)}{\partial E})\, T(E)\, dE, \quad T(E) = \text{Tr}\left[t\,(E)^{\dagger}\, t\,(E)\right] \tag{1.1}$$

where T is the transmission, f is the Fermi-Dirac distribution function, 't(E)' is a matrix of transmission coefficients for waves propagating along the conductor, and E is the wave energy. At zero temperature,

$$-\frac{\partial f\,(E)}{\partial E} = \delta(E - E_f) \tag{1.2}$$

where δ is the Dirac delta function and E_f is Fermi energy, so that

$$G = G_0\, T(E_f), \quad G_0 = 2\frac{e^2}{h} \tag{1.3}$$

where G_0 is the quantum conductance unit, e is the charge on an electron, and h is Planck's constant. For an ideal metallic carbon nanotube, $T(E_f) = 2$

and $G = 2G_0$ [7]. The effects of van der Waals interactions on the optimized geometry were found to be negligible, and are discussed in the Appendix.

SIESTA and TranSIESTA have shown good accuracy and consistency when validated against experiments, as well as established computational methods, for a variety of applications and materials [4, 5, 8]. Validation data for SIESTA include bond length and bond angle for water molecules; lattice constant, cohesive energy, and bulk modulus of silicon; and pressure in bulk iron [4]. TranSIESTA was validated against experiments for the current voltage characteristics of atomic wires made from gold and platinum [5]. Other studies have also shown good agreement with experiments using SIESTA and TranSIESTA for the electronic transport properties of germanium [9], electrostatic properties of protein molecules [10], and the chemical reactivity of metallic nanoparticles [11].

The computations in this dissertation were performed on the Lonestar5 and Stampede2 supercomputers deployed by Texas Advanced Computing Center (TACC) at the University of Texas at Austin. The Intel Xeon E5-2690 v3 (Haswell) nodes on Lonestar5 and the Intel Xeon Platinum 8160 (Skylake) nodes on Stampede2 were used. The Haswell nodes consist of 24 cores per node with a 2.6 GHz clock rate and 64 GB RAM while the Skylake nodes consist of 48 cores per node with a 2.67 GHz clock rate and 192 GB RAM. Typical equilibrium calculations took 24 to 96 hours using 2 to 4 nodes in parallel and typical conductance calculations (at each bias voltage) took 24 to 48 hours using 4 to 6 nodes. The most computationally intensive calculations

took ∼216 hours on 6 nodes.

1.3 Chemiresistive performance metrics

In the chemiresistive sensing discussion which follows, three performance metrics are employed to quantify the effects of target molecule adsorption on the modeled sensor configurations.

The first metric quantifies the change in conductance (ΔG) due to analyte molecule adsorption

$$\Delta \mathrm{G} = \mathrm{G}_{\mathrm{sensor+analyte}} - \mathrm{G}_{\mathrm{sensor}} \tag{1.4}$$

where G_{sensor} is the conductance of the doped nanotube and $G_{sensor+analyte}$ is the conductance of the sensor after adsorption of the analyte.

The second metric quantifies the change in energy (ΔE) associated with target molecule adsorption

$$\Delta \mathrm{E} = \mathrm{E}_{\mathrm{total}} - \mathrm{E}_{\mathrm{sensor}} - \mathrm{E}_{\mathrm{analyte}} \tag{1.5}$$

where E_{total} denotes the energy of the sensor with the adsorbed analyte, E_{sensor} denotes the energy of the doped nanotube in isolation, and $E_{analyte}$ denotes the energy of the analyte (explosive molecule, hazardous gas molecule, or background gas molecule) in isolation.

The third metric is defined as the change in nanotube current associated with adsorption of an analyte, and is computed for each combination of analyte

and sensor, as a function of the bias voltage (V)

$$\Delta I = I(V, sensor, analyte) - I_{ref}(V, sensor) \tag{1.6}$$

where $I_{ref}(V, sensor)$ is the current in a sensor under bias voltage V in the absence of an adsorbed analyte.

1.4 Principal component analysis

Principal Component Analysis (PCA) is widely used [12, 13, 14, 15, 16, 1] to analyze the performance of sensor arrays which, like the olfactory system, rely on "pattern recognition" [17] to identify analytes. PCA forms linear combinations of the original (in this case nine dimensional) sensor data space, which are the new coordinates (principal components) of a reduced order description of the sensing data. If sufficient principal components are retained to account for (typically) 95 percent [18, 19, 17] of the variance in the sensor data, and if the analyte coordinates are sufficiently separated in principal component space, PCA may be used to estimate the performance of an array sensing scheme.

Each of the data sets was analyzed as follows: (1) a principal component analysis of the data set was performed using commercially available software, (2) the cumulative variance of the data set, as a function of the number of principal components included in the reduced order model, was plotted for a principal component count ranging from one to the minimum number (n) of principal components required to account for at least 95 percent of the variance

in the data set, (3) an illustrative plot of analyte separation in the first and second principal component (PC1-PC2) subspace was constructed, (4) a color Distance Metric plot depicting the Euclidean 'separation distance' [17] of the analytes in the n-dimensional principal component space was constructed, and (5) a 'classification' threshold [17] was applied to the Distance Metric plot to evaluate the performance of the sensor array. The Distance metric (D_{jk}) employed here to describe the separation of the jth and kth analytes in an n-dimensional principal component subspace is

$$D_{jk} = \sqrt{\frac{1}{n}\sum_{i=1}^{n}\left(x_i^{(j)} - x_i^{(k)}\right)^2} \tag{1.7}$$

where $x_i^{(j)}$ and $x_i^{(k)}$ denote the ith principal component coordinates of the jth and kth analytes.

In this dissertation, principal component analysis is used as a design tool. The ability of a sensor array to discriminate between any two analytes was estimated by applying a classification threshold to the analyte separation distances in principal component space; this estimates the selectivity of the sensor arrays. By applying the same classification threshold to the PCA results for various sensor arrays, the most selective array configuration can be identified.

The remaining chapters are organized as follows: Chapter 2 discusses the disparate effects of various dopant classes on the conductance of carbon nanotubes, of critical interest in chemiresistive sensing. Chapter 3 investigates

the chemiresistive sensing performance of nine different internally doped carbon nanotube configurations, for the detection of explosives and hazardous gases. Chapter 4 investigates the chemiresistive sensing performance of five different defective or substitutionally doped carbon nanotube configurations, for the detection of explosives and hazardous gases. Chapter 5 investigates the chemiresistive sensing performance of metallic carbon nanotubes with four different covalent functionalizations. Chapter 6 investigates the chemiresistive sensing performance of semiconducting carbon nanotubes with four different covalent functionalizations. Chapter 7 formulates a new ab initio molecular dynamics (AIMD) model of spin polarized sensor dynamics, including electric and magnetic field loading. Chapter 8 summarizes the contributions of this dissertation, and suggests possible directions for future work.

Schematics of the analyte molecules studied in this dissertation are shown in Table 1.1.

Table 1.1: Schematic graphs of studied molecules

Target Molecules

HMX	RDX	TNT
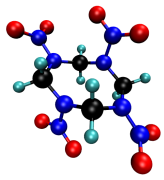	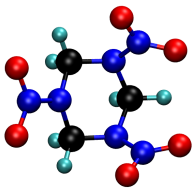	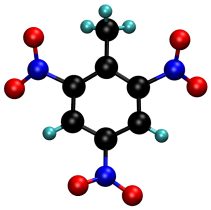

Gas Molecules

N_2	O_2	H_2O	CO_2	NO_2	NH_3
				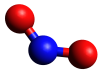	

Chapter 2

Mass Specific Performance of Halogen and Alkali Metal Based Dopants in Carbon Nanotube Wiring

2.1 Introduction

The remarkable properties of some one and two dimensional nanocarbons, in particular graphene nanoribbons and carbon nanotubes, have motivated research on their application to a variety of engineering problems. One problem of wide interest is the development of improved electrical wiring. Low mass density [20], high electrical conductivity [21], and compatibility with spin fabrication processes have made carbon nanotubes (CNTs) a prime candidate in the search for next generation conductors. Although theoretical calculations have suggested that the electrical conductivity of CNTs can be much higher than that of copper or aluminum [22], experiments on CNT based wiring have measured electrical conductivities which are much less than the theoretical maximum. Despite these difficulties, strong interest in the development of high mass specific conductivity wiring for weight sensitive applications, such as vehicles, ships, and aircraft, has encouraged continued research.

A variety of intrinsic (e.g. substitutional or vacancy defects) and extrinsic (e.g. alignment and packing) factors [23] have limited the performance

of CNT based wiring. Although some important mechanical processing steps [24, 25] have been developed to improve the conductivity of CNT wiring, they have not led to a mass specific performance which exceeds that of copper. The most promising route to high mass specific conductivity appears to be chemical doping [26]. Published experimental research on chemical doping of CNTs has considered both n and p type dopants, as well as combinations of the two types. Common n-type dopants include alkali metals [27], transition metals, and their compounds [28]. The most commonly used p-type dopants include halogens [27, 26], interhalogens [29], and acids [30, 25]. Chemical species which notionally incorporate both n and p type dopants have also been investigated, including alkali metal halides (LiCl, LiBr, LiI, KI, CsI) [25].

Recognizing the considerable challenges inherent in the experimental development of nanocarbon wiring, complementary computational research has attempted to gain a better understanding of dopant performance. Much computational work has been limited to relatively simple models and described changes in nanotube [29, 31, 32] or nanotube junction [33] conductance due to particular dopants. For example Janas et al. [29] computed the conductance and the density of states for I_2, ICl, and IBr doping of metallic (5,5) and semiconducting (10,0) CNTs. The modeled CNTs were very short (3 to 5 unit cells) and were suspended between bulk copper electrodes, producing baseline conductance results for pristine CNTs which did not match those widely accepted in the literature. Ciraci et al. [34] investigated the effects of tube rotation, junction overlap length, and relative tube axis orientations on junc-

tion conductance. Similarly, Li et al. [33] performed a computational study of CNT junctions, with a single atom of various transition metals serving as the dopant. The overlap of the junctions was limited to one half a unit cell, and the best results were observed with a Cr atom as the linker. Recent computational work has extended these basic models, to include important effects which appear at the nanowire scale. Li et al. [35] modeled the effects of iodine doping on CNTs and CNT junctions, and Chin et al. [36, 37] developed similar models for a more complex dopant ($KAuBr_4$). Consistent with experiment, the last three cited works estimated specific conductivities for the doped CNT systems which were lower than that for copper.

Although previous computational work on doped CNT wiring has provided important insights, a broader view is needed to assist future experimental work. This chapter extends previous computational studies of CNT based wiring, modeling four material classes (halogens, interhalogens, alkali metals, and alkali metal halides) in a unified framework. The objective is to provide an integrated view of the strengths and weaknesses of the various doping strategies considered to date, and to suggest the most promising approaches for the experimental pursuit of improved mass specific performance. The new ab initio modeling work described in this chapter indicates that the four dopant material classes most prominent in the experimental literature have inherent performance limitations when applied to the metallic-semiconducting nanotube mix typical of current experimental research. It appears that spatial separation of the metallic/semiconducting nanotubes or spatial control of the dopant

distribution would likely be necessary in order to fundamentally improve the mass specific performance of these dopants.

2.2 Computational models

In this chapter, in the transport direction, the scattering region was bounded by CNT electrodes whose nuclear coordinates were constrained to avoid shape distortion of the electrode cross sections. The electrodes were modeled using dopant distributions like those applied to the modeled device, simulating an infinitely long conductor. No constraints were applied in the scattering region.

The three geometry models considered in this chapter are depicted in Fig. 2.1, where they are shown with both monatomic and diatomic dopants. The choice of these three model geometries is motivated by: (1) published experimental work on gas adsorption [38] and dopant adhesion [26] in CNT bundles, which suggests that dopant atoms will be predominately distributed in interstitial channels and therefore largely aligned with the nanotube axes, and (2) published computational work on iodine doping of CNTs [35] which concluded that randomly distributed dopant atoms are ineffective at improving conductance and serve primarily to add parasitic mass to the system. The top row of Fig. 2.1 shows an 'aligned' dopant configuration, in which the dopant atoms are equilibrated in one or more columns along the nanotube axis; it represents a best case dopant distribution for a single nanotube and may be expected to produce an upper bound result for the mass specific performance

of the doped system. The middle row of Fig. 2.1 shows an 'interstitial' dopant configuration, in which the dopant atoms are again equilibrated in one or more columns along the nanotube axis, the columns this time defined by a 'three-body' (CNT-dopant-CNT) interaction which determines both the CNT separation distance and the dopant standoff from the nanotube surface. In this instance it appears that the size of the dopant atoms, for some given nanotube chirality and dopant class, is an important factor in determining dopant effectiveness. The lower row of Fig. 2.1 shows a nanotube interface or 'junction' with interstitial doping. All of the junction models considered here are commensurate, that is the hexagons of the parallel CNTs are precisely aligned (no offset in either the lateral displacement or the rotational alignment). Junctions are an essential feature of wiring constructed from CNT bundles, and dopant atom size can also be important in determining junction performance.

Four performance metrics were defined in order to: compare the relative performance of the various modeled dopants, compare the performance of the doped nanotubes to that of a pristine nanotube, and compare the modeled nanoscale system performance to macroscopic test data. The four metrics are defined as follows: (1) *specific conductance* is the ratio of the computed conductance of a device to its mass per unit length, (2) *relative specific conductance* is the ratio of the specific conductance of a device to the specific conductance of a pristine metallic (5,5) nanotube, (3) *specific conductivity* is the ratio of electrical conductivity (σ) to mass density (ρ), and (4) *relative specific conductivity* is the ratio of the specific conductivity of a device to the

specific conductivity of copper. In the case of a doped device, dopant mass is included in the mass per unit length calculation. Note that in the case of a one dimensional electrical conductor with conductance G, mass M, and length L, the mass specific conductivity (Γ) is [35]

$$\Gamma = \frac{\sigma}{\rho} = \frac{G\,L^2}{M} \tag{2.1}$$

and no estimate is needed for the cross sectional area of the CNT conductor. The performance metrics defined here are of particular importance since the focus of the experimental literature has been on increasing conductivity, as opposed to mass specific conductivity.

2.3 Results and discussion

This section describes the ab initio modeling results for four dopant classes: halogens (chlorine, bromine and iodine), alkali metals (lithium and sodium), interhalogens (iodine monochloride and iodine monobromide), and alkali metal halides (lithium bromide and potassium iodide). The performance of each dopant was analyzed at two or three different doping densities and in the aligned, interstitial, and interstitial junction configurations. Since the nanotube bundles normally used to produce CNT wiring are typically composed of a mix of metallic and semiconducting tubes, ab initio calculations were performed for both metallic (5,5) and semiconducting (8,0) nanotubes, hereafter referred to as CNT(M) and CNT(S).

2.3.1 Analysis of the doped nanotubes

The first set of analyses modeled aligned and interstitial doping configurations for both metallic and semiconducting nanotubes. Fig. 2.2 shows the relative specific conductance results for the halogen and the alkali metal dopants. Among the halogens, bromine offers the best performance, but the doped CNT exceeds the mass specific conductance of a pristine metallic CNT by (at best) only about ten percent. The alkali metals show better peak performance, exceeding (in the case of lithium) the specific conductance of a pristine metallic nanotube by a factor of almost three. However, the preceding best case results for both the halogens and the alkali metals are obtained in an idealized 'aligned' dopant configuration. In an interstitial dopant configuration, all five of the modeled halogen and alkali metal dopants produce an average specific conductance (average of the metallic and semiconducting nanotube performance) which is approximately half that of a pristine metallic CNT. Fig. 2.3 shows the relative specific conductance results for the interhalogens and the alkali metal halides. In these cases, the modeled 'diatomic' dopants offer at best a specific conductance slightly better than that of a pristine metallic CNT. As in the case of the 'monatomic' dopants, the diatomic dopants produce (in the interstitial configuration) an average specific conductance which is roughly half that of a pristine metallic CNT.

Fig. 2.4 provides illustrative charge transfer data (estimated using three different metrics), density of states (DOS) plots, and charge density difference plots for the best performing halogen (bromine) and the best performing al-

kali metal (lithium) dopants. The charge transfer data indicates p-doping of a metallic nanotube by bromine and n-doping of a metallic nanotube by lithium; the two DOS plots both indicate an increase in the density of states at the Fermi energy, due to the dopant partial density of states (PDOS). The charge density difference plots of Fig. 2.4 suggest that the best performing halogen and alkali metal configurations, which are obtained with aligned dopant atoms, may incorporate significant electron transmission through the dopant. A similar conduction mechanism has been previously suggested in ab initio modeling work performed on iodine doped nanotubes [35]. Figs. 2.5 and 2.6 provide illustrative charge transfer data, density of states plots, and charge density difference plots for particular interhalogen and alkali metal halide doped cases, which depict a number of important features of the doping process. Fig. 2.5 indicates that the conductance changes induced by the interhalogens are associated with p-doping and a substantial increase in the Fermi energy density of states, for both metallic and semiconducting nanotubes. In the case of the IBr doped CNT(M) shown in Fig. 2.5, the dopant appears to be polarized; it increases the conductance of the system by approximately fifty percent. However since the mass per unit length increases by a similar percentage, the specific conductance of the doped nanotube is similar to that of a pristine CNT(M). In the case of the ICl doped CNT(S) shown in Fig. 2.5, the charge density difference plot depicts a complex multibody interaction between the CNTs and the dopant atoms. Although the ICl doped CNT(S) does show a nonzero transmission, the specific conductance falls far below that of a pristine metallic CNT.

Fig. 2.6 indicates that the improved conductance induced by the alkali metal halides is associated with p-doping for the metallic nanotube and n-doping for the semiconducting nanotube. In the case of LiBr doping of a CNT(M) the DOS is however unaffected by the presence of dopant. The CNT(M) conductance is unchanged, and the addition of a parasitic dopant mass serves only to reduce the specific conductance of the system. In the case of KI doping of a CNT(S), both the Fermi energy DOS and and the conductance are substantially increased. However, given the well known effectiveness of potassium as a CNT dopant [27, 37], it appears that the iodine atoms degrade the doping performance of the potassium, reducing the specific conductance of the system to a level well below that of a pristine metallic CNT.

Fig. 2.2 summarizes the results of the nanotube doping analysis, plotting the relative specific conductance for all nine dopant types considered in this chapter. For each dopant, the plotted bar represents the average performance over the range of doping densities considered in the analysis (density ranges in dopant atoms or molecules per unit cell are shown in Figs. 2.2 and 2.3). The results shown in Fig. 2.2 are for the interstitial doping configuration only, and the results for metallic and semiconducting nanotubes are presented separately. None of the doped nanotubes show a specific conductance which exceeds that of pristine metallic CNT. In the CNT(M) case, all three of the halogen dopants produced similar results, all four of the diatomic dopants produced similar results, and the two alkali metals showed the most variation, representing both the best case and and the worst case performance. If the

effects of potassium doping (analyzed in a recently published work [37]) are also considered, the alkali metals show a strong dependence of dopant effectiveness on dopant atom size, with the smallest dopant atom being the least effective. The CNT(S) doping results shown in Fig. 2.2 indicate an overall lower performance, as compared to the CNT(M) case, with the best CNT(S) performance lower than the worst CNT(M) performance. The CNT(S) doping results also show a much greater variation in performance with dopant type. The alkali metals show the best CNT(S) doping performance, the halogens are on average less effective, and the performance of the diatomic dopants varies widely with dopant type. Note that CNT(S) doping with halogens shows, like the CNT(M) doping with alkali metals, a strong dependence on dopant atom size, with the smallest dopant atom again being the least effective.

The models discussed here consider only the interaction of metallic or semiconducting nanotubes, which are assumed to represent the best and worst case performance.

2.3.2 Analysis of the doped junctions

The second set of analyses modeled doping of the nanotube junctions, with the dopant distributed in an interstitial configuration, at the higher of the two doping densities considered in the doped nanotube analyses. Fig. 2.8 shows the variation of junction conductance with nanotube overlap (in unit cells) for both metallic and semiconducting nanotube junctions, for all nine modeled dopants. Since the unit cell lengths for the metallic (5,5) and semiconducting

(8,0) nanotubes are 2.46 Å and 4.26 Å respectively, the unit cell overlap ranges shown for the CNT(M) and the CNT(S) calculations in Fig. 2.8 differ by factor of two and hence represent similar overlap distances. As indicated in Fig. 2.8, the modeling results show that junction performance varies with overlap, and is also a strong function of the dopant type.

The CNT(M) junctions show a general trend in which the junction conductance increases with overlap, albeit with oscillations. The period of the oscillations is two unit cells, for all of the dopants except LiBr and KI; a similar trend was also observed by Ciraci et al. [34] in their analysis of pristine metallic CNT junctions. The interhalogen dopants are exceptional, in that they show 'perfect' conductance ($G = 2G_o$) at all overlaps. The only other dopant which produces a perfect junction is bromine, which does so at an at an eight unit cell overlap. The two modeled alkali metals show surprisingly poor metallic junction conductance. Charge transfer data and DOS plots for the lithium and sodium doped CNT(M) junctions are shown in Fig. 2.9. Although the charge transfer magnitudes for these two dopants are large and similar, in both cases the Fermi energy DOS is quite small and the junction transmission is negligible. The performance difference between the lithium and sodium doping cases appears to be due to a larger equilibrium separation distance for the interacting nanotubes (3.87 Å vs 3.34 Å) in the lithium case, a three-body (CNT-dopant-CNT) effect which is dopant atom size dependent.

In the CNT(S) junction case, the best dopants are the alkali metals; however no dopant offers a semiconducting junction performance which ex-

ceeds 25 percent of that of a pristine metallic CNT. Fig. 2.10 summarizes the results of the nanotube junction analysis, plotting the average (over the modeled overlaps) of the relative specific conductance for both CNT(M) and CNT(S) junctions, for all nine dopant types considered in this chapter. Note that among the alkali metals (as an isolated group), the larger the dopant atom the more effective the doping performance (this includes potassium, analyzed in recent work [36]). A similar size effect is seen for the halogens (as an isolated group) in the CNT(S) junction case, but not in the CNT(M) junction case due to the relatively small unit cell length for the metallic CNT.

2.3.3 Nanowire model

In macroscale conductors composed of CNT bundles, both the nanotube conductance and the junction conductance results just described can be expected to influence overall wiring performance. A nanowire model developed in previous work [35, 36] may be used to estimate the macroscale CNT wiring performance of the dopants analyzed here, using the nanotube and junction conductance results described in the last two subsections (see the Supporting Information for tabulated data used in the calculations discussed in this subsection). The referenced model provides a one dimensional transmission line description of a nanowire, one mean free path (L_{MFP}) in length and incorporating nanotube junctions. The specific conductivity of the nanowire is computed as

$$\Gamma = \frac{\sigma}{\rho} = \frac{G_{eff} L_{MFP}^2}{m_{eff}} \tag{2.2}$$

where the effective conductance is the minimum of the doped nanotube (G_n) and doped junction (G_j) conductances

$$G_{eff} = min(G_n, G_j) \tag{2.3}$$

and the mass of the nanowire is

$$m_{eff} = (L_{MFP} - L_j)\,\hat{m}_n + L_j\,\hat{m}_j \tag{2.4}$$

where L_j is the junction length, $\hat{m}_n$ is the mass per unit length for the doped nanotube, and $\hat{m}_j$ is the mass per unit length for the doped junction. Analysis of the doped nanowires of interest in this chapter assumed: (1) an interstitial doping configuration for both the nanotubes and the junctions, (2) the average junction overlap distances considered in this work (shown in Fig. 2.8), and (3) a mean free path of 500nm [39]. Fig. 2.11 plots an average relative specific conductivity for each of the nine doped nanowires considered in this chapter, where average refers to relative specific conductivities computed at the two interstitial nanotube doping densities shown in Figs. 2.2 and 2.3. Recall that the relative specific conductivity metric compares the performance of the doped CNT nanowires to that of copper, whose density and electrical conductivity are taken from handbook data at standard conditions [40]. The results plotted in Fig. 2.11 show trends which clearly distinguish the metallic from the semiconducting nanowires and clearly identify characteristics of the four dopant types:

- although both the metallic and the semiconducting wires show performance dependencies on dopant type, which vary the computed results

by ±50% around their respective averages, the average performance of the metallic nanowires exceeds the average performance of the semiconducting nanowires by an approximate order of magnitude;

- the best CNT(M) dopants are the interhalogens, followed by bromine; iodine and KI offer the possibility of improving on the performance of copper, while the performance of the other dopants is inferior to that of copper;

- the best CNT(S) dopants are the alkali metals, followed by iodine; the performance of the remaining dopants is less than 20% of that for copper;

- due to poor junction conductance, lithium is ineffective as a metallic dopant and the alkali metal halides are ineffective as semiconducting dopants;

- the near-orthogonal performance characteristics of the various dopant types suggests that fabricating high mass specific conductivity wiring from metallic/semiconducting CNT mixtures may be very difficult.

The preceding conclusions appear to be qualitatively consistent with the published experimental data. A recent experimental study [25] on the conductivity (as opposed to specific conductivity) of doped single-wall CNT thin films included four of the dopants analyzed here. In measurements on mixed metallic-semiconducting systems, they showed a tripling of conductivity with iodine and IBr dopants and very modest conductivity improvements

from two alkali metal halides (LiBr and KI); note that the dopant mass loadings for the experiments were not reported. Although the same reference also reported conductivity tests on 'metallic' and 'semiconducting' thin films for the iodine and IBr dopants, the measured conductivities of the reference (undoped) samples of the metallic, semiconducting, and mixed nanotube types showed rather modest differences; this suggests that more definitive test data is needed. A second experimental study [29] on ICl and IBr doped CNT thin films similarly reported ten to thirty-five percent reductions in measured resistance due to doping, again without quantifying dopant mass loading. A tentative conclusion from these comparisons is that the computational work presented here can make relative judgments, as opposed to precise predictions, regarding the efficacy of alternative doping treatments.

Two other comparisons with experiment are provided by papers which report the specific conductivity of iodine doped [26] double-wall CNTs and the specific conductivity of ICl-doped [41] double-wall and single-wall CNTs. The first paper reported an average specific conductivity for the tested samples slightly higher than that of copper. This measurement compares favorably with the current relative specific conductivity estimates of 1.19 and 0.25 for iodine doping of CNT(M) and CNT(S) respectively. The second paper measured relative specific conductivities of 0.19 and 0.05 for double-wall and single-wall CNTs doped with ICl, less than the factors of 4.14 and 0.16 computed here for ICl doped metallic and semiconducting nanotubes. Although the available experimental data indicates only qualitative agreement with the modeling re-

sults, it does suggest that the underlying computational methodology can offer valuable insights. The models developed here for small diameter, defect-free nanotubes and junctions composed of identical, well aligned nanotube pairs do not account for a variety of non-ideal conditions present in most experiments. Most of these non-ideal conditions would tend to reduce carbon conductor performance.

2.4 Summary

Although additional experimental evaluation of the modeling approach described in this chapter is needed, it appears that the relative dopant performance estimates computed here are largely consistent with published experimental data. Hence it is appropriate to offer here some general conclusions on the performance of halogens, alkali metals, interhalogens, and alkali metal halides as CNT dopants, conclusions which rely on computational assessments of dopant performance that are not amenable to direct experimental measurement. The conclusions are guided by a comparative evaluation of the nine dopants considered in this study, on six mass specific performance criteria: effectiveness as a CNT(M) dopant (see Fig. 2.2, left hand side), effectiveness as CNT(M) junction dopant (see Fig. 2.10, left hand side), overall effectiveness as a CNT(M) dopant (see Fig. 2.11, left hand side), and three corresponding criteria applied to the semiconducting nanotubes modeled in this chapter (Figs. 2.2, 2.10, and 2.11, right hand side). For each of the six performance criteria, the associated dopant performance metrics were normalized (dividing

by the best performance metric for that criterion, among all nine dopants). In this way, all nine dopants were ranked, on a scale from zero to one, on all six performance criteria. The results are plotted in Fig. 2.12, using a color scheme in which the normalized rankings are classified as 'good' (green, 1.00-0.66), 'average' (yellow, 0.66-0.33), and 'poor' (red, 0.33-0.00). Classifying dopant performance using these bins is considered appropriate, given the qualitative agreement of the models with experiment.

The performance evaluations shown in Fig. 2.12 suggest several conclusions of general interest to the development of high specific conductivity carbon nanotube based wiring, conclusions which complement the material specific assessments made in the last section:

- all of the modeled dopants showed 'good' or 'average' mass specific performance when applied to metallic nanotubes; it is the doping of semiconducting nanotubes and the doping of junctions of both types which are the important mass specific performance discriminators;

- doped CNT based wiring tests have generally employed a single dopant and a mix of nanotube types; since all of the dopants studied here are rated 'poor' for either metallic *nanowires* or semiconducting *nanowires*, most systems tested to date have likely included considerable parasitic mass;

- either metallic/semiconducting segregation of CNTs, or the development of dopants which are adsorbed on only one CNT type, may offer large

performance improvements.

Since the conclusions offered here are based on models of one metallic and one semiconducting single-wall nanotube, both with small diameters, more research is needed. Despite this caveat, the discussion of experimental data in the last section does suggest that there is some transferability of this work to other carbon systems, including CNT based thin films and multi-wall nanotubes.

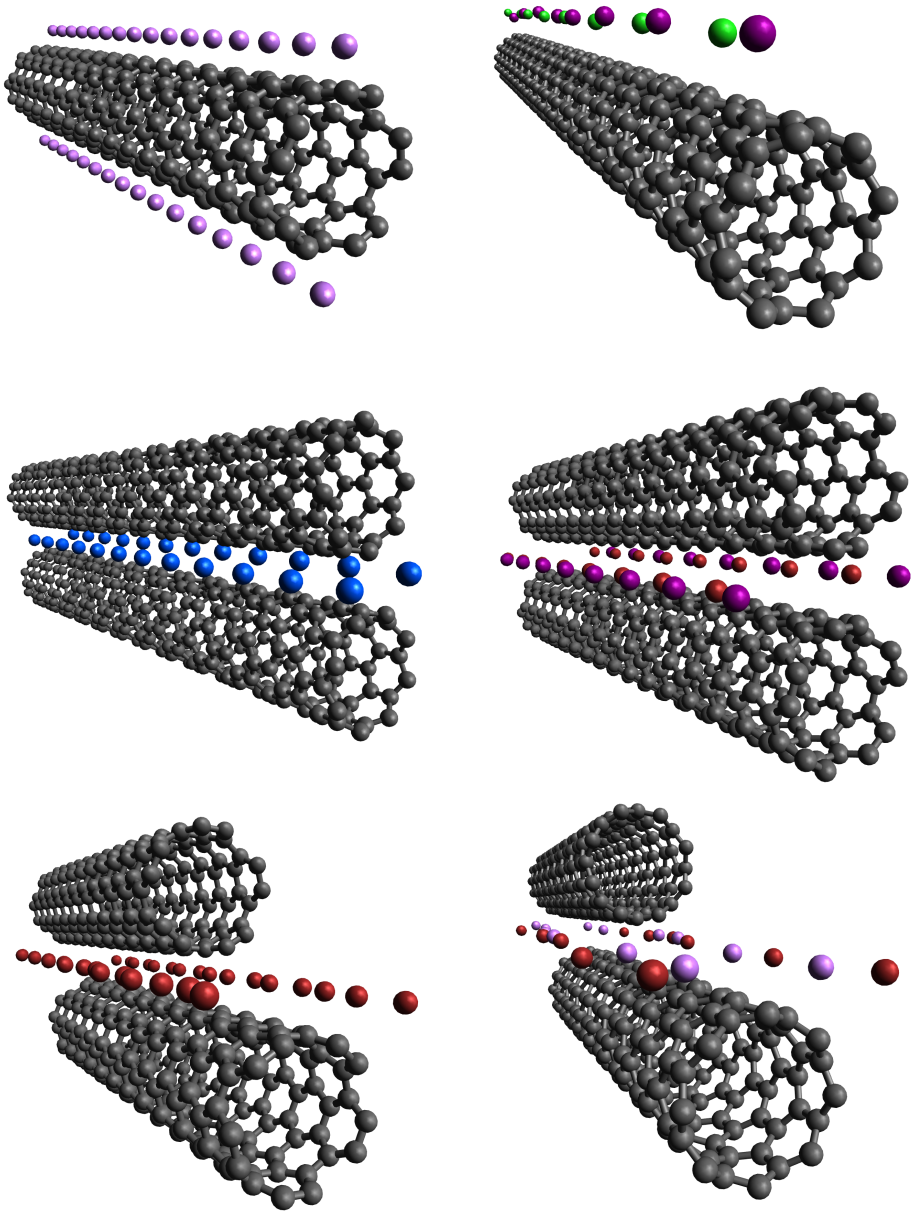

Figure 2.1: Nanotube and junction models; the top row shows a CNT(M) with aligned Li doping (left) and a CNT(S) with aligned ICl doping (right); the middle row shows a CNT(S) with interstitial Na doping (left) and a CNT(M) with interstitial IBr doping (right); the bottom row shows a CNT(M) junction with interstitial Br doping (left) and a CNT(S) junction with interstitial LiBr doping (right).

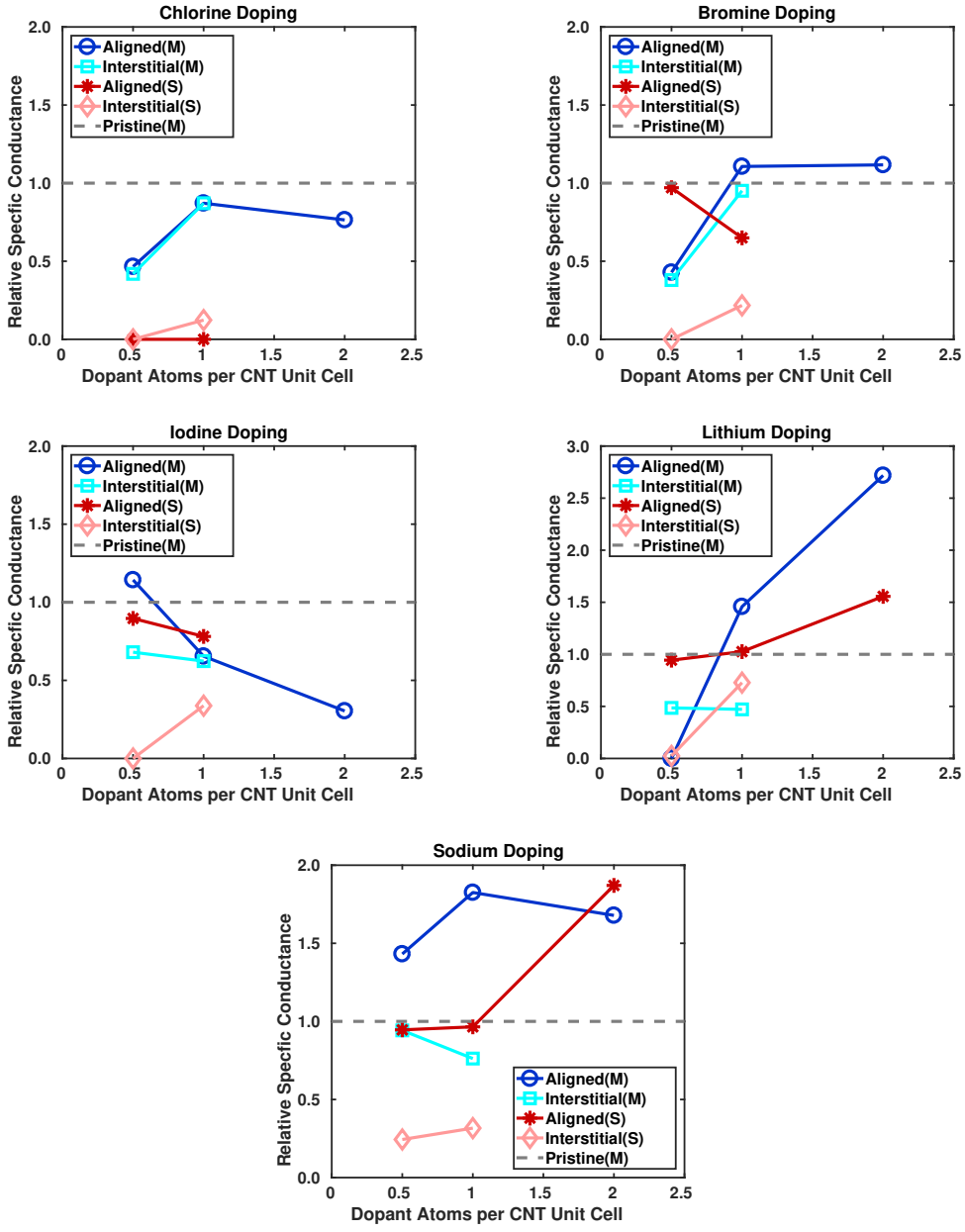

Figure 2.2: Relative specific conductance of doped CNT(M) and CNT(S), for monatomic dopants, as a function of the doping configuration and the doping density; the dashed line shows the relative specific conductance of a pristine metallic CNT.

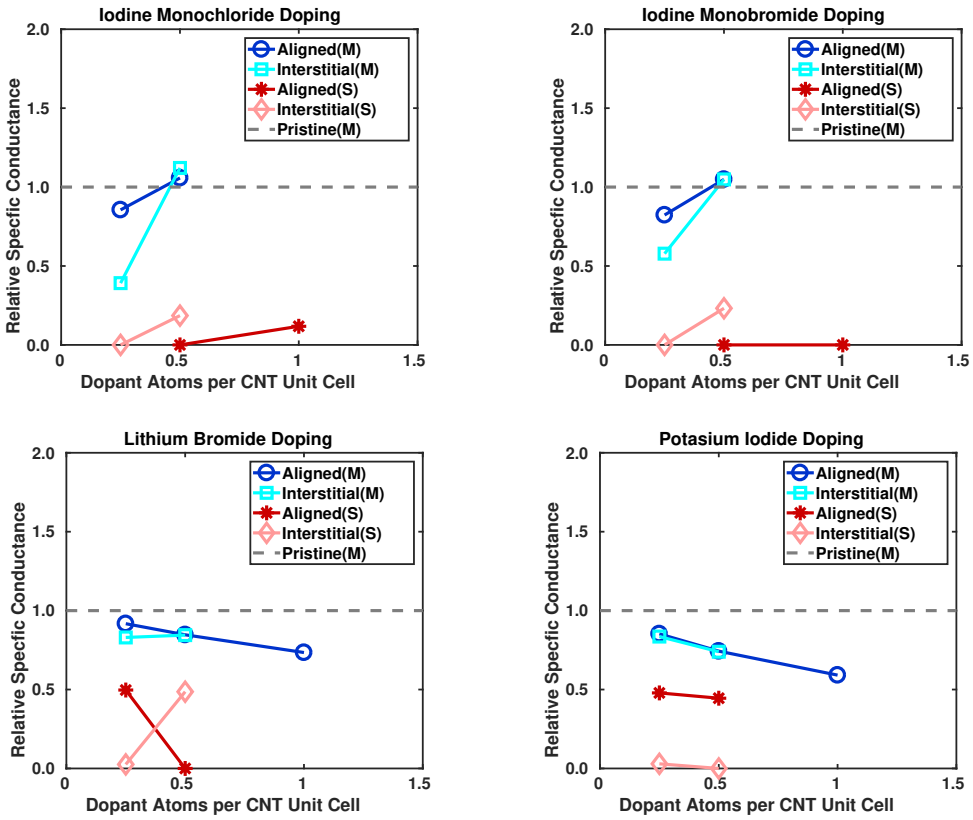

Figure 2.3: Relative specific conductance of doped CNT(M) and CNT(S), for diatomic dopants, as a function of the doping configuration and the doping density; the dashed line shows the relative specific conductance of a pristine metallic CNT.

Charge transfer (e), Br doped CNT (5,5)				Charge transfer (e), Li doped CNT (5,5)			
Mulliken	Hirshfeld	Voronoi	$\Delta G/G_0$	Mulliken	Hirshfeld	Voronoi	$\Delta G/G_0$
-1.609	-1.435	-1.455	0.95	3.610	1.973	2.500	3.75

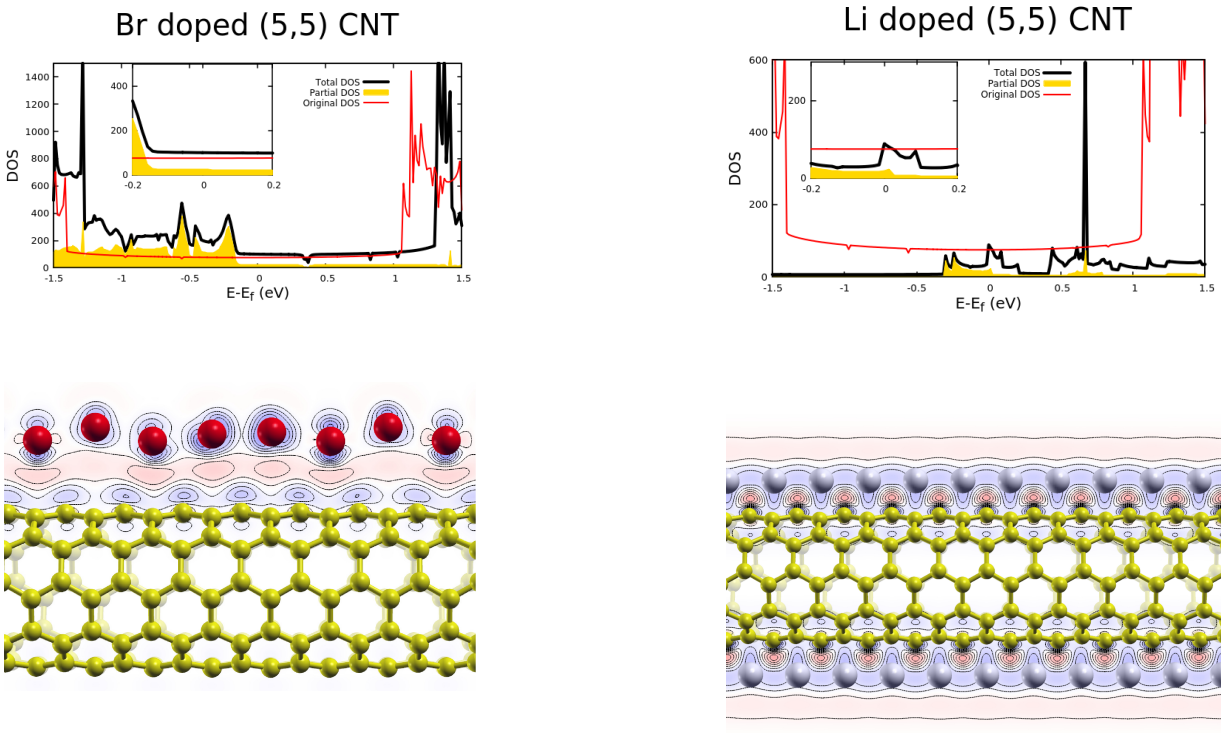

Figure 2.4: Charge transfer (top row), density of states (middle row), and charge density difference (bottom row) for Br doped CNT(M) (left side) and Li doped CNT(M) (right side). The shaded regions of the density of states plots show the partial density of states for the dopant atoms.

Charge transfer (e), IBr doped CNT (5,5)				Charge transfer (e), ICl doped CNT (8,0)			
Mulliken	Hirshfeld	Voronoi	$\Delta G/G_0$	Mulliken	Hirshfeld	Voronoi	$\Delta G/G_0$
-0.338	-0.225	-0.220	1.00	-3.27	-2.658	-2.824	0.31

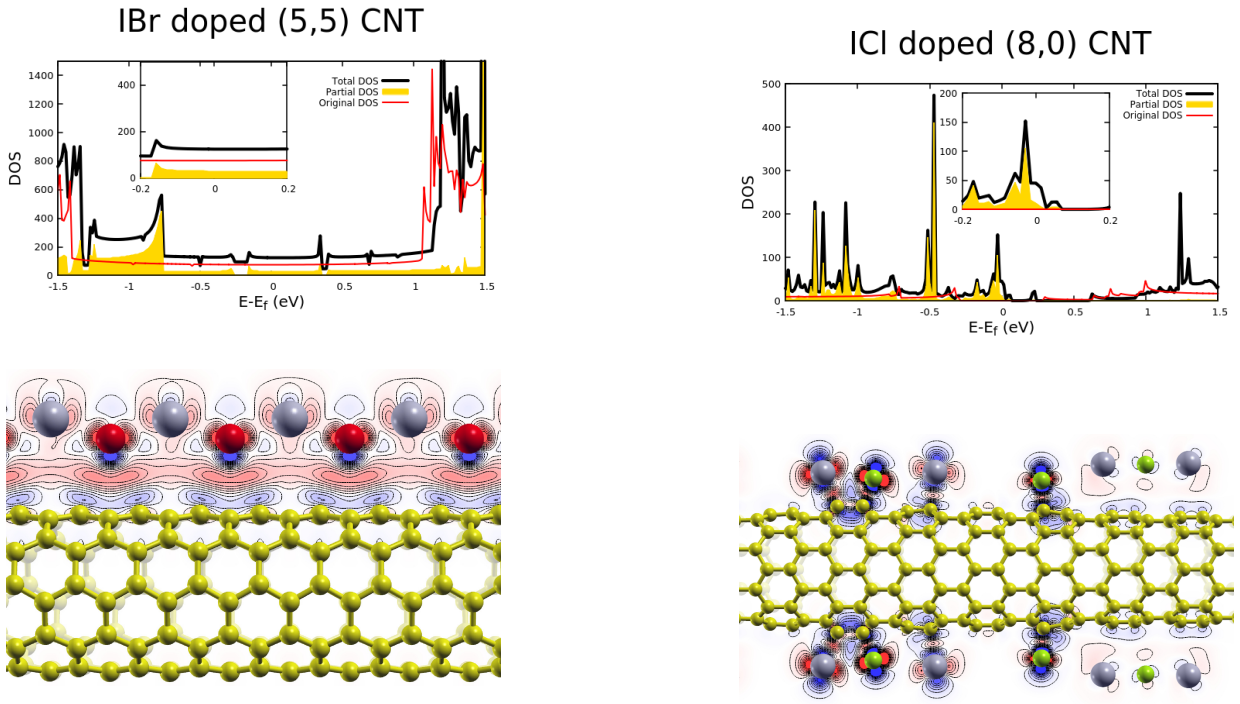

Figure 2.5: Charge transfer (top row), density of states (middle row), and charge density difference (bottom row) for IBr doped CNT(M) (left side) and ICl doped CNT(S) (right side). The shaded regions of the density of states plots show the partial density of states for the dopant atoms.

Charge transfer (e), LiBr doped CNT (5,5)				Charge transfer (e), KI doped CNT (8,0)			
Mulliken	Hirshfeld	Voronoi	$\Delta G/G_0$	Mulliken	Hirshfeld	Voronoi	$\Delta G/G_0$
-1.242	-0.864	-1.072	0.0	7.792	6.176	7.156	1.00

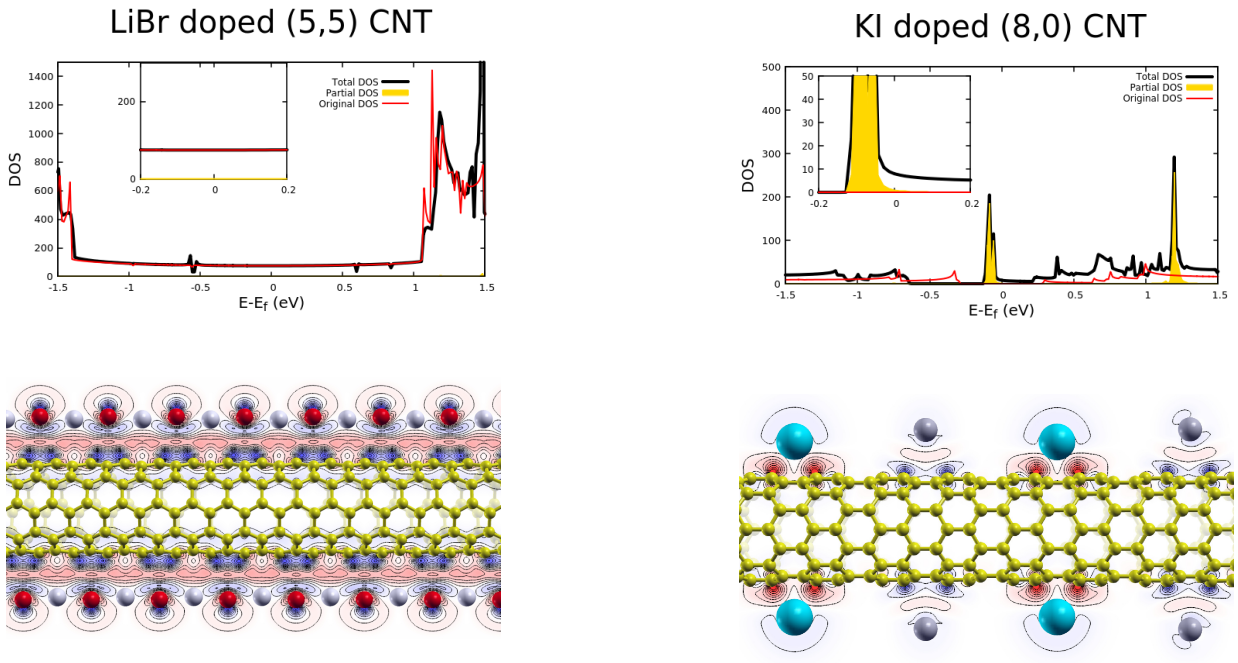

Figure 2.6: Charge transfer (top row), density of states (middle row), and charge density difference (bottom row) for LiBr doped CNT(M) (left side) and KI doped CNT(S) (right side). The shaded regions of the density of states plots show the partial density of states for the dopant atoms.

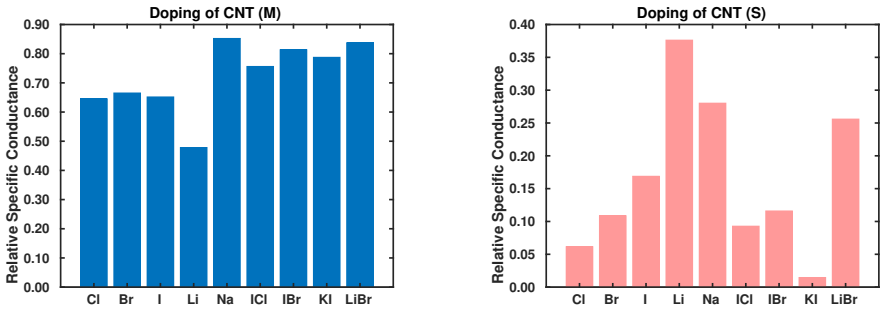

Figure 2.7: Relative specific conductance as a function of dopant type.

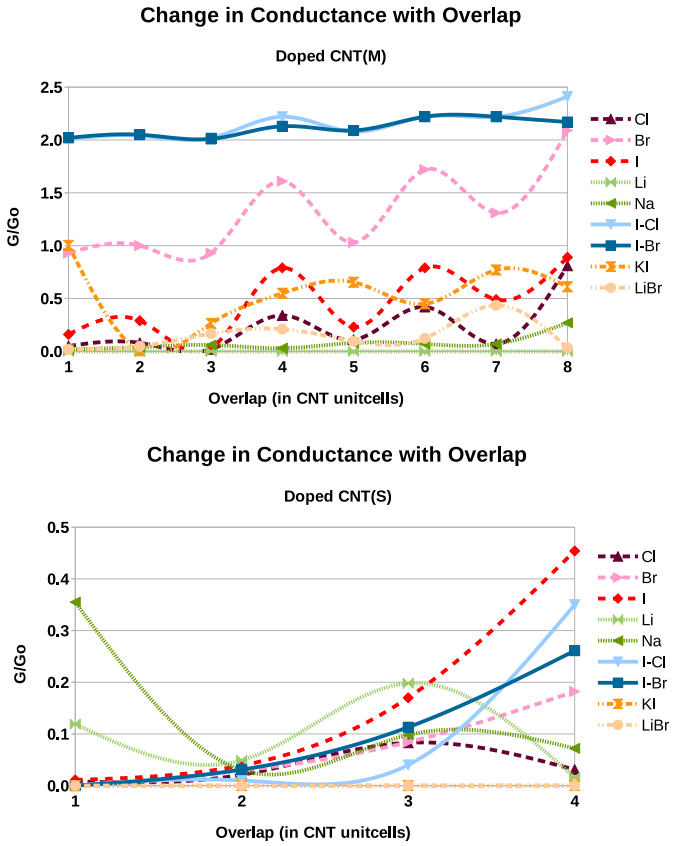

Figure 2.8: Junction conductance as a function of nanotube overlap.

Charge transfer (e)				
Dopant	Mulliken	Hirshfeld	Voronoi	G/G_0
Li	5.178	4.942	5.280	0.00
Na	4.673	4.616	4.776	0.27

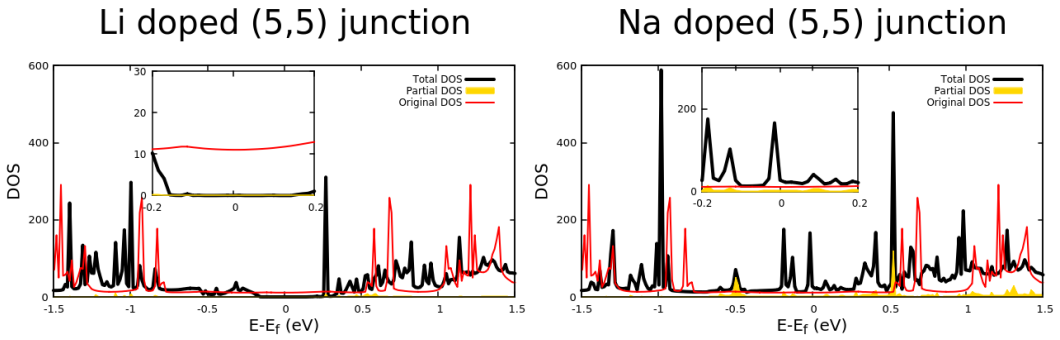

Figure 2.9: Charge transfer (top) and density of states (bottom) for Li and Na doped CNT(M) junctions. The shaded regions of the density of states plots show the partial density of states for the dopant atoms.

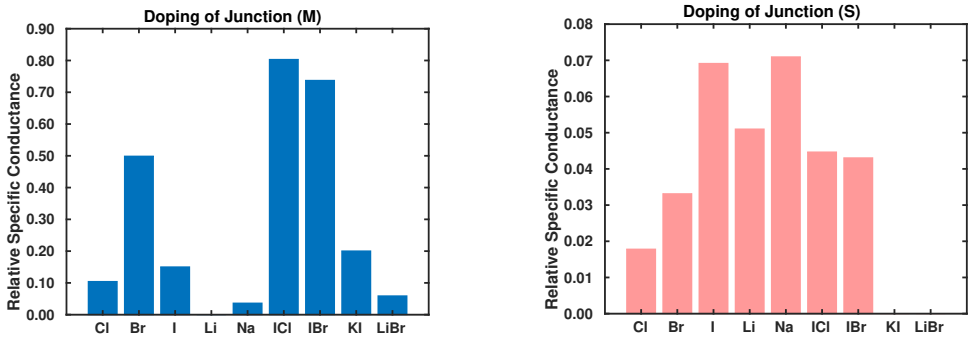

Figure 2.10: Relative specific conductance of the CNT(M) junctions (left) and the CNT(S) junctions (right) as a function of dopant type.

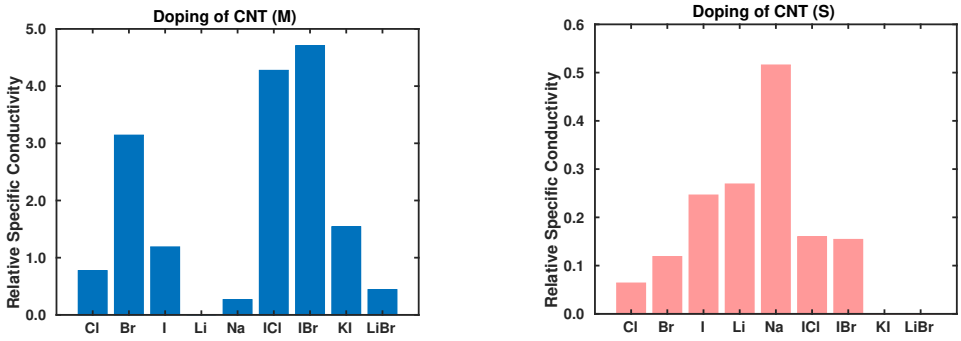

Figure 2.11: Relative specific conductivity for the CNT(M) nanowires (left) and the CNT(S) nanowires (right) as a function of dopant type.

Performance for the CNT Dopants									
	Cl	Br	I	Li	Na	ICl	IBr	KI	LiBr
CNT (M)									
CNT (M) Junction									
Nanowire Model (M)									
CNT (S)									
CNT (S) Junction									
Nanowire Model (S)									

Green = Good, Yellow = Average, Red = Poor

Figure 2.12: Comparison of the modeled halogen, alkali metal, interhalogen, and alkali metal halide dopants on six mass specific performance criteria. The colors (green, yellow, red) represent performance ratings (good, average, poor) for doping of CNT(M) and CNT(S), doping of CNT(M) and CNT(S) junctions, and current transmission in CNT(M) and CNT(S) nanowires. Note that the nanowire performance ratings depend on the transmission efficiencies of the nanotubes and the nanotube junctions.

Table 2.1: Atomic masses used in the analysis

Element	C	Cl	Br	I	Li	Na	K
Mass (amu)	12.0107	35.4460	79.9040	126.9045	6.9410	22.9900	39.0983

Table 2.2: Properties of the modeled CNTs

CNT chirality	Atoms per unit cell	Unit cell length (Å)
(5,5)	20	2.46
(8,0)	32	4.26

Table 2.3: Computed conductance values for the monatomic dopants

			Computed conductance (G/G_0)				
CNT type	Doping type	Dopant density (atoms/unit cell)	Cl	Br	I	Li	Na
(5,5)	Aligned	0.50	1.00	1.00	2.89	0.00	3.00
		1.00	2.00	2.95	2.00	3.00	4.00
		2.00	1.98	3.72	1.25	5.75	4.00
	Interstitial	0.50	1.80	1.77	3.44	1.97	3.95
		1.00	4.00	5.07	3.81	1.94	3.34
	Junction	1.00	0.24	1.33	0.46	0.00	0.08
(8,0)	Aligned	0.50	0.00	1.98	1.93	1.76	1.80
		1.00	0.00	1.45	1.92	1.93	1.89
		2.00	n.c.	n.c.	n.c.	2.98	3.87
	Interstitial	0.50	0.00	0.00	0.00	0.45	0.46
		1.00	0.50	0.97	1.66	2.74	1.24
	Junction	1.00	0.04	0.07	0.17	0.10	0.14

Notes: junction conductance values are averages over the modeled overlaps; n.c. denotes not computed

Table 2.4: Computed conductance values for the diatomic dopants.

			Computed conductance (G/G_0)			
CNT type	Doping type	Dopant density (molecules/unit cell)	ICl	IBr	KI	LiBr
(5,5)	Aligned	0.25	2.00	2.00	2.00	2.00
		0.50	2.83	3.00	2.00	2.00
		1.00	n.c.	n.c.	2.00	2.00
	Interstitial	0.25	1.83	2.81	3.92	3.62
		0.50	6.00	6.00	3.98	3.99
	Junction	0.50	2.15	2.11	0.54	0.14
(8,0)	Aligned	0.25	n.c.	n.c.	0.98	0.97
		0.50	0.00	0.00	1.00	0.00
		1.00	0.31	0.00	n.c.	n.c.
	Interstitial	0.25	0.00	0.00	0.06	0.00
		0.50	0.83	1.09	0.00	2.00
	Junction	0.50	0.10	0.10	0.00	0.00

Notes: junction conductance values are averages over the modeled overlaps; n.c. denotes not computed

Chapter 3

Internal Doping of Metallic Carbon Nanotubes for Chemiresistive Sensing of Explosive Molecules

3.1 Introduction

Carbon nanotubes (CNTs) have been the focus of much chemical sensing research [42], aimed at exploiting the unusual electrical, mechanical, optical, and chemical properties of CNTs for sensing applications. One of the most widely investigated applications has been gas sensing [43], often employing a chemiresistive mechanism [44]. Such sensors can be simple and robust, but are often not selective. Hence much chemiresistive CNT gas sensing research has evolved as a search for improved selectivity, while maintaining the simplicity and robustness of the basic chemiresistive sensing mechanism. Sensor arrays are frequently suggested as an effective means of addressing the simplicity versus selectivity tradeoff [17].

The broader topic of gas adsorption by CNTs is a subject of very wide interest [45]. Gas sensing by surface adsorption [46, 47], which is typical of chemiresistive CNT sensing, has been investigated for pristine CNTs, functionalized CNTs [48], substitutionally doped CNTs [49], and CNTs with defects

[50]. Other CNT related research, aimed at improving the electrical conductivity [27] of carbon based wiring, has also focused on surface adsorption processes. Experimental and computational work on doping for enhanced conductivity has studied the surface interaction of CNTs with acids [25], alkali metals [27], halogens [26], interhalogens [41, 29], and other dopants [28].

In addition to chemiresistive sensing and surface adsorption processes, a third process of frequent interest in CNT based research is the encapsulation of materials inside carbon nanotubes. Experimental work, validated by imaging technology, has shown that a wide range of materials can be captured inside CNTs, including solid phase materials (usually metals) and gases. The solid phase materials include Ru [51], Ag [52, 53], Au, Pt, and Pd [52], which normally form nanowires inside the nanotubes. Multiple small gas molecules have been shown to adsorb on the inner, convex surface of CNTs, including Xe, O_2 and N_2 [54, 38], and some large molecules (e.g. CCl_4) also show preferential adsorption inside the CNTs [55]. Published experiments have placed chains of potassium [56], iodine [57], and potassium iodide [58] inside CNTs. In order to deliberately encapsulate materials inside the CNTs, various (in and ex situ) methods are used. In situ methods include filling the CNT with a catalyst metal during CVD growth [59], while ex situ methods include capillary filling [51]. In the case of single-walled CNTs, the 'as produced' CNTs may be closed at both ends by fullerene-like end caps. Opening methods are however available, include mechanical cutting [60, 55], application of concentrated acids [51], and heating in the presence of lead metals [61].

Despite the large number of studies showing the possibility of internal doping of CNTs (over 150 materials have been reported inside single-wall CNTs [62]), the theoretical and experimental literature on the effects of internal doping on the electronic structure and electrical conductance of CNTs is very limited. Published studies have focused on the Raman Spectra of filled CNTs [63, 64] and computed the effects of filling on CNT band structures [65, 66]. Zhou et al. [67] computed the transport properties of Gd/Eu chains located inside single-wall CNTs, and Korsun et al. [68] computed the changes in entropy and HOMO-LUMO structures for CNTs filled with Li^+ and Mg^{2+} ions.

Although some previous research has studied the effects of combined internal and external doping on CNTs [69], it appears that no previous work has considered the chemiresistive sensing properties of CNTs with internal doping. This chapter models chemiresistive sensing via surface adsorption, for CNTs internally doped by nine materials commonly applied to enhance CNT conductivity. The internal dopants include three halogens, three alkali metals, two interhalogens, and one alkali metal halide. The target analytes include three widely used explosives [70], one nitroaromatic compound (TNT) and two nitramines (RDX and HMX). Sensor response to nitrogen dioxide and ammonia are also analyzed, due to the very wide interest in these compounds indicated by the hazardous gas detection literature, and sensor response to four background gases (N_2, CO_2, H_2O, and O_2) is also computed. Principal Component Analysis (PCA) [71, 72, 17] is used to evaluate the ability of the

full array of nine doped CNTs to distinguish the five target molecules from standard background gases, and to distinguish the three explosives from each other. The results show good sensitivity and selectivity for all of the target molecules, suggesting that chemiresistive sensing using internally doped CNTs offers a significant new opportunity in the development of simple, robust, and selective gas sensors.

3.2 Computational methods

All of the computations were performed for metallic carbon nanotubes with a (5,5) chirality and a unit cell length of 2.46 Å. Doping densities were one atom per unit cell for the monatomic dopants and one molecule per two unit cells for the diatomic dopants. The sensor models were initialized with the dopant atoms or molecules spaced uniformly along the nanotube axis. The analyte molecule orientations analyzed in the present chapter were the minimum energy orientations obtained from a preliminary analysis modeling the adsorption of each analyte on a pristine (5,5) CNT. In the third (transmitting) direction, the supercell is bounded by electrodes composed of doped nanotubes identical to the nanotube in the scattering zone, in order to represent a conductor of infinite length.

3.3 Results and discussion

The first series of calculations modeled the effects of all nine internal dopants on the conductance of metallic (5,5) CNTs; equilibrium configurations

for the iodine and potassium doped nanotubes are shown in Fig. 3.1.

3.3.1 Computational results

Fig. 3.2 shows the computed change in conductance due to the internal doping, for each of the nine dopants, expressed in terms of the quantum conductance unit (G_o). The black dashed line indicates the conductance of the pristine (5,5) CNT, before doping [7]. In the 'best' cases (iodine and potassium), conductance is doubled by the doping process. This result is consistent with published experiments that indicate that external doping with potassium [27] or iodine [26] can significantly improve the electrical conductivity of CNTs. It is also consistent with a previous computational study on internal doping with alkali metals, which used band diagrams to argue that such doping can improve CNT conductivity [66]. In the 'worst' cases (chlorine and potassium iodide), conductance is essentially unchanged by the doping; however note that this does not indicate that the doped nanotube is unsuitable as a sensor, only that its reference configuration conductivity is not modified by the doping. The remaining halogens and alkali metals, as well as the interhalogens, induce an approximate fifty percent increase in the CNT conductance. This is consistent with published experimental data on external doping of CNTs with halogens [26], alkali metals [27], and interhalogen compounds [41] which also shows significant improvements in the electrical conductivity of CNTs. Fig. 3.4 shows charge transfer data (computed using three different metrics), density of states (DOS) plots, and charge density difference plots for the CNTs doped by

iodine and potassium. The charge transfer data indicates that iodine p-dopes the CNT while potassium n-dopes the CNT. The DOS plots show a significant increase in the DOS near the Fermi energy for both the dopants, with substantial contributions from the dopant partial density of states (PDOS). The charge density difference plots suggest substantial current transmission through both the dopant atoms and the CNT.

The second series of calculations modeled the effects of analyte adsorption on the surface of the doped CNTs, for all 81 dopant/analyte combinations. Fig. 3.4 shows equilibrium configurations for RDX, HMX, and TNT molecules adsorbed on iodine, potassium, iodine monochloride, and potassium iodide doped CNTs. Figs. 3.5- 3.7 plot the change in conductance (equation 1) and the adsorption energy (equation 2) due to analyte adsorption on all nine doped CNT sensors, for halogen doping (Fig. 3.5), alkali metal doping (Fig. 3.6), and interhalogen or alkali metal halide doping (Fig. 3.7). In the case of halogen doping (Fig. 3.5), iodine shows the largest conductance sensitivities and the largest adsorption energies, but the least selectivity. Chlorine shows generally low adsorption energies, but a highly selective response to oxygen and nitrogen dioxide. Bromine is similar to chlorine in its selective response to oxygen and nitrogen dioxide, but for all other analytes its conductance change differs in sign from that of chlorine. Clearly these results include ingredients which support a sensor array based approach to selectivity. In the case of alkali metal doping (Fig. 3.6), conductance sensitivities and adsorption energies are both high. While selectivity is moderate, the large magnitudes of the con-

ductance changes induced by the analytes would in general facilitate species discrimination. In the case of the diatomic dopants (Fig. 3.7), adsorption energy is very high for potassium iodide and moderate for the interhalogens; the conductance changes also show high selectivity, including all analyte classes (explosives, background gases, and hazardous gases). Overall the ab initio modeling results suggest that, as a group, the internally doped CNTs offer good sensitivity and may offer good selectivity if deployed in a sensing array.

For convenient reference, additional plots of the adsorption energy and conductance change data shown in Figs. 3.5- 3.7 are provided, for the explosives only, re-parameterized by explosive type and by background gas type in Figs. 3.8 and 3.9. In addition, Table 3.1 provides all of the conductance change data shown in Figs. 3.5- 3.7. That data is used next in a Principal Component Analysis of the computed sensor performance characteristics.

3.3.2 Principal Component Analysis

To evaluate the collective performance of the nine doped CNTs, acting as a sensor array, a Principal Component Analysis (PCA) was performed for three data sets extracted from Figs. 3.5- 3.7. The first data set consisted of the conductance change data for the three explosives and the four background gases; the second data set consisted of the conductance change data for nitrogen dioxide and the four background gases; and the third data set consisted of the conductance change data for ammonia and the four background gases. All three data sets included the computed response for all nine sensors.

Fig. 3.10 depicts the results of the principal component analysis for the explosive molecules and background gases. The Cumulative Variance plot (top left) shows that four principal components are sufficient to capture at least 95 percent of the sensor data variance. The PC1-PC2 subspace plot (top right) illustrates the analyte separation obtained with a minimal two dimensional representation of the transformed data. The distance metric plot (lower left) plots the separation distances for all seven analytes in the four dimensional principal component subspace, indicating a maximum separation of approximately $1.8G_o$. If a classification criterion of $0.9G_o$ is applied to the distance metric plot, the resulting Classification Chart (lower right) estimates the ability (green squares) or inability (red squares) of the sensor array to discriminate between each pair of analytes. In this case the sensor array can distinguish RDX from the other two modeled explosives and all of the background gases, indicating excellent selectivity, whereas HMX and TNT are indistinguishable from each other and two of the background gases (CO_2 and H_2O). The classification criterion of $0.9G_o$, selected here to illustrate the analysis methodology, is quite conservative, recognizing that $2G_o$ is the conductance of a pristine metallic nanotube. Hence the results presented here suggest that internally doped metallic CNT arrays offer significant opportunities in explosive molecule sensing applications.

Fig. 3.11 depicts the results of the principal component analysis for nitrogen dioxide and four background gases. In this case the Cumulative Variance plot (top left) shows that only two principal components are needed to

capture at least 95 percent of the sensor data variance. The PC1-PC2 subspace plot (top right) describes analyte separation in that two dimensional space, and the distance metric plot (lower left) quantifies the separation distances for all five analytes in the two dimensional principal component subspace, indicating a maximum separation of approximately $2.5G_o$. If a classification criterion of $0.9G_o$ is again applied to the distance metric plot, the resulting Classification Chart (lower right) indicates that the sensor array can distinguish nitrogen dioxide from three of the four background gases. As noted previously, the classification criterion of $0.9G_o$ is quite conservative, suggesting that internally doped metallic CNT arrays offer significant opportunities in nitrogen dioxide sensing applications.

Finally, Fig. 3.12 depicts the results of the principal component analysis for ammonia and four background gases. In this case the Cumulative Variance plot (top left) shows that three principal components are needed to capture at least 95 percent of the sensor data variance. The PC1-PC2 subspace plot (top right) illustrates analyte separation obtained with a minimal two dimensional representation of the transformed data. The distance metric plot (lower left) quantifies the separation distances for all five analytes in the three dimensional principal component subspace, indicating a maximum separation of approximately $2.0G_o$. If a classification criterion of $0.9G_o$ is again applied to the distance metric plot, the resulting Classification Chart (lower right) indicates that the sensor array can distinguish ammonia from all four background gases, although just as in the previous two cases, water and carbon

dioxide are not distinguishable. Since the classification criterion of $0.9G_o$ is quite conservative, it appears that internally doped metallic CNT arrays offer significant opportunities in ammonia sensing applications.

3.4 Summary

Chemiresistive sensing using sensor arrays has offered a simple, robust, but often non-selective approach to the detection of explosives and hazardous gases, a subject of considerable interest in a variety of military, government, and industrial applications. Although abundant research has studied surface adsorption of various molecules on CNTs, chemical doping of CNTs to modify their electronic properties, and encapsulation of a wide variety of materials inside CNTs, it appears that no previous work has combined internal doping, external surface adsorption, and chemiresistive sensing in an attempt to produce sensitive and selective detectors for explosives and hazardous gases. The present work suggests that such sensing schemes offer significant opportunities to improve upon the state of the art in explosive sensing technology. Although a wide range of important sensor design and performance issues are not considered in this chapter, the fundamental sensor design concepts suggested in this chapter appear to warrant further investigation.

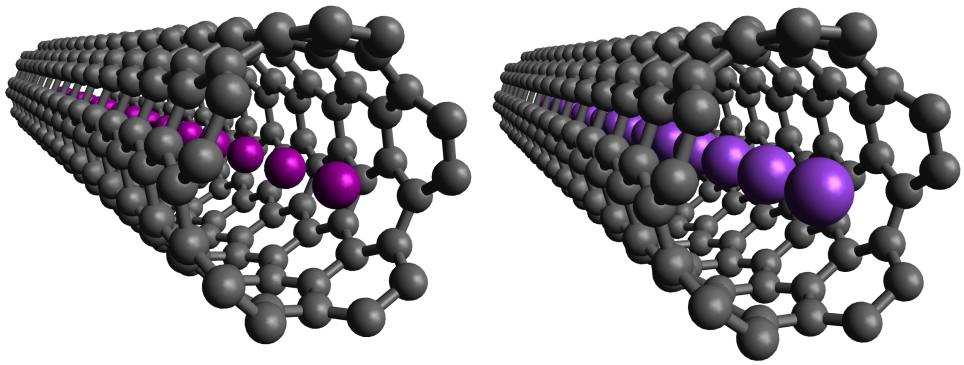

Figure 3.1: Internal doping of a CNT(5,5): iodine (left) and potassium (right).

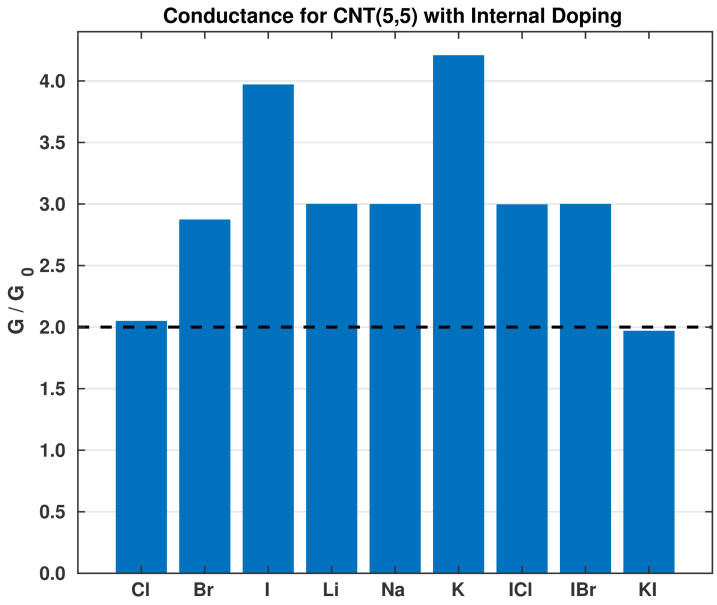

Figure 3.2: Conductance of a CNT(5,5) with nine different internal dopants. Dashed line indicates the conductance of a pristine CNT(5,5).

Charge transfer (e), I doped CNT (5,5)				Charge transfer (e), K doped CNT (5,5)			
Mulliken	Hirshfeld	Voronoi	$\Delta G/G_0$	Mulliken	Hirshfeld	Voronoi	$\Delta G/G_0$
-0.335	-1.283	-0.696	1.970	6.871	4.695	4.174	2.207

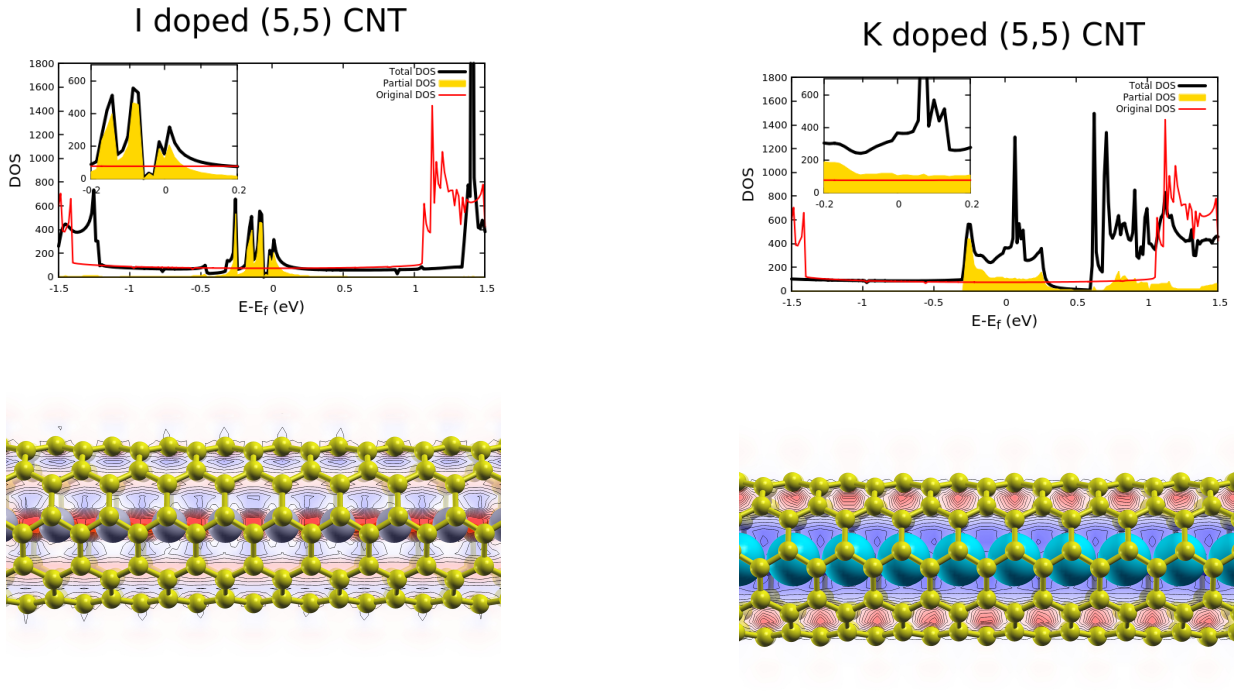

Figure 3.3: Charge transfer data (top row), density of states plots (middle row), and charge density difference plots (bottom row) for an iodine doped CNT(5,5) (left side) and a potassium doped CNT(5,5)) (right side). The shaded regions of the density of states plots show the partial density of states for the dopant atoms.

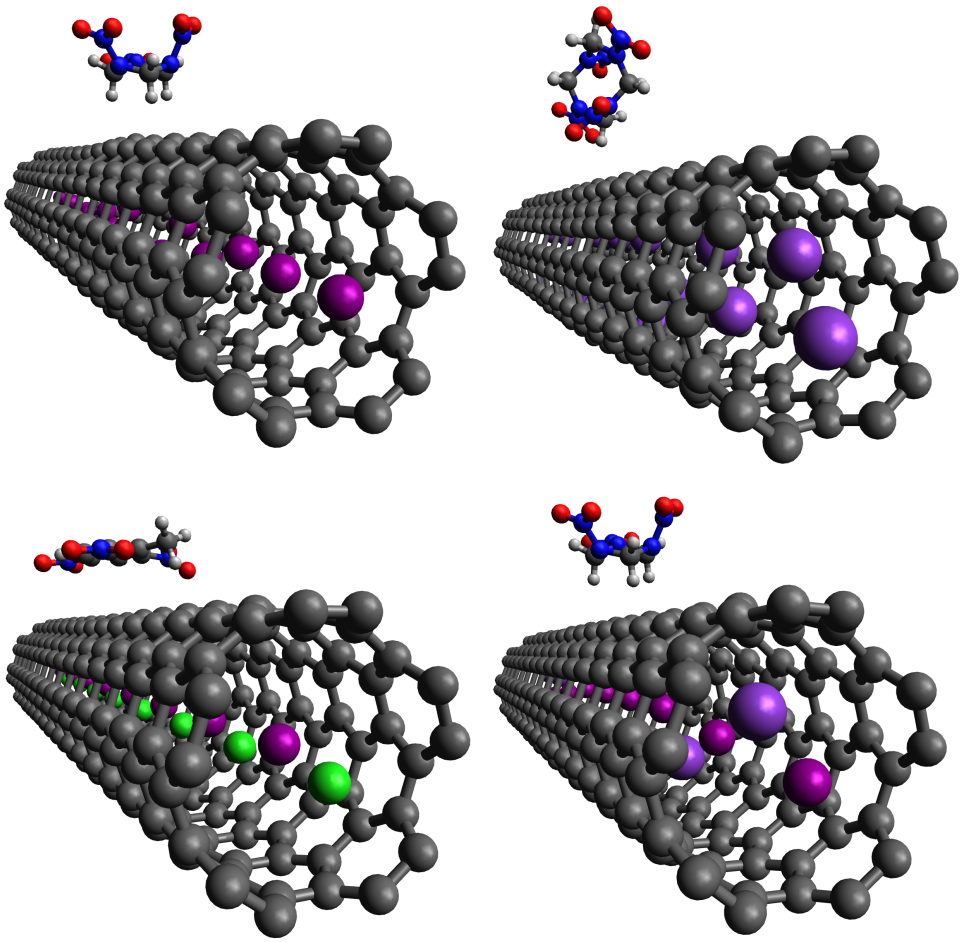

Figure 3.4: Chemiresistive sensing of explosive molecules with internally doped CNT(5,5): RDX sensing with iodine doping (top left), HMX sensing with potassium doping (top right), TNT sensing with iodine monochloride doping (bottom left), and RDX sensing with potassium iodide doping (bottom right).

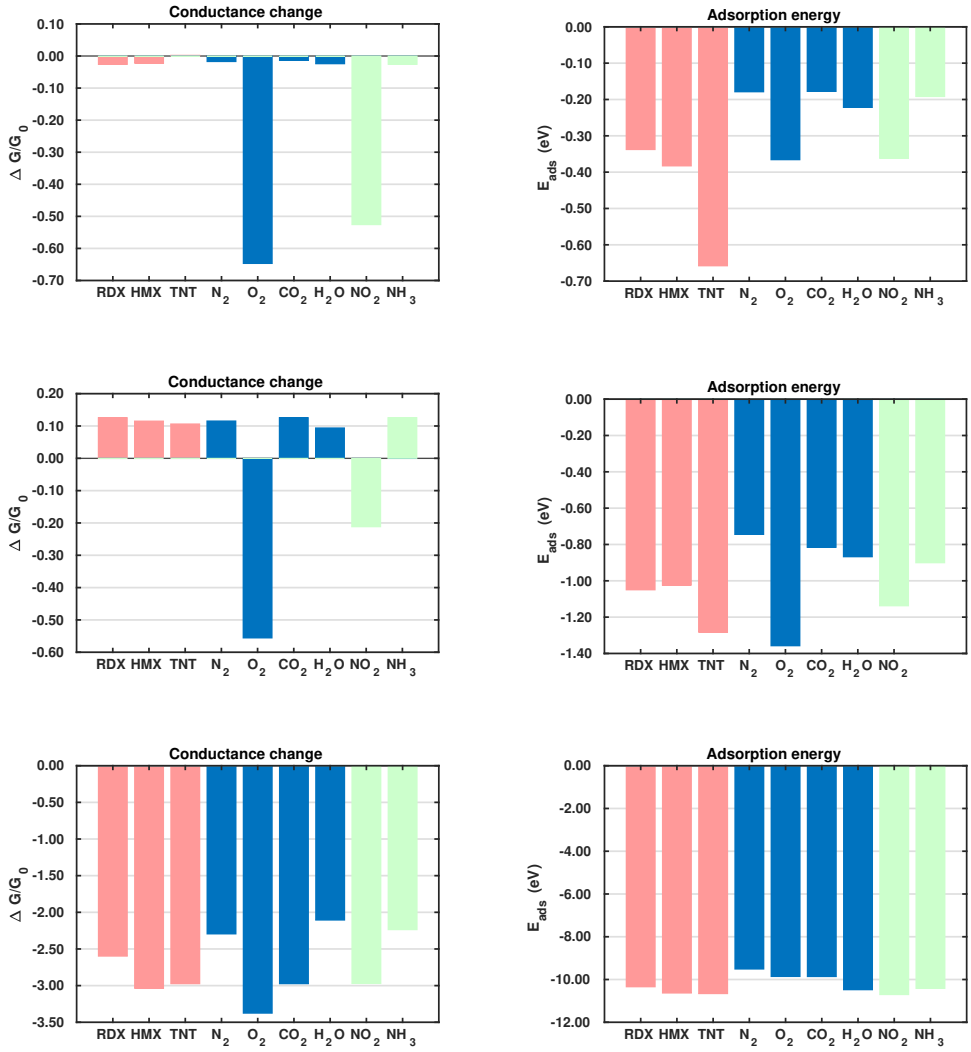

Figure 3.5: Conductance changes (left) and adsorption energy (right) due to analyte adsorption by halogen doped CNT(5,5): chlorine doping (top row), bromine doping (middle row), and iodine doping (bottom row).

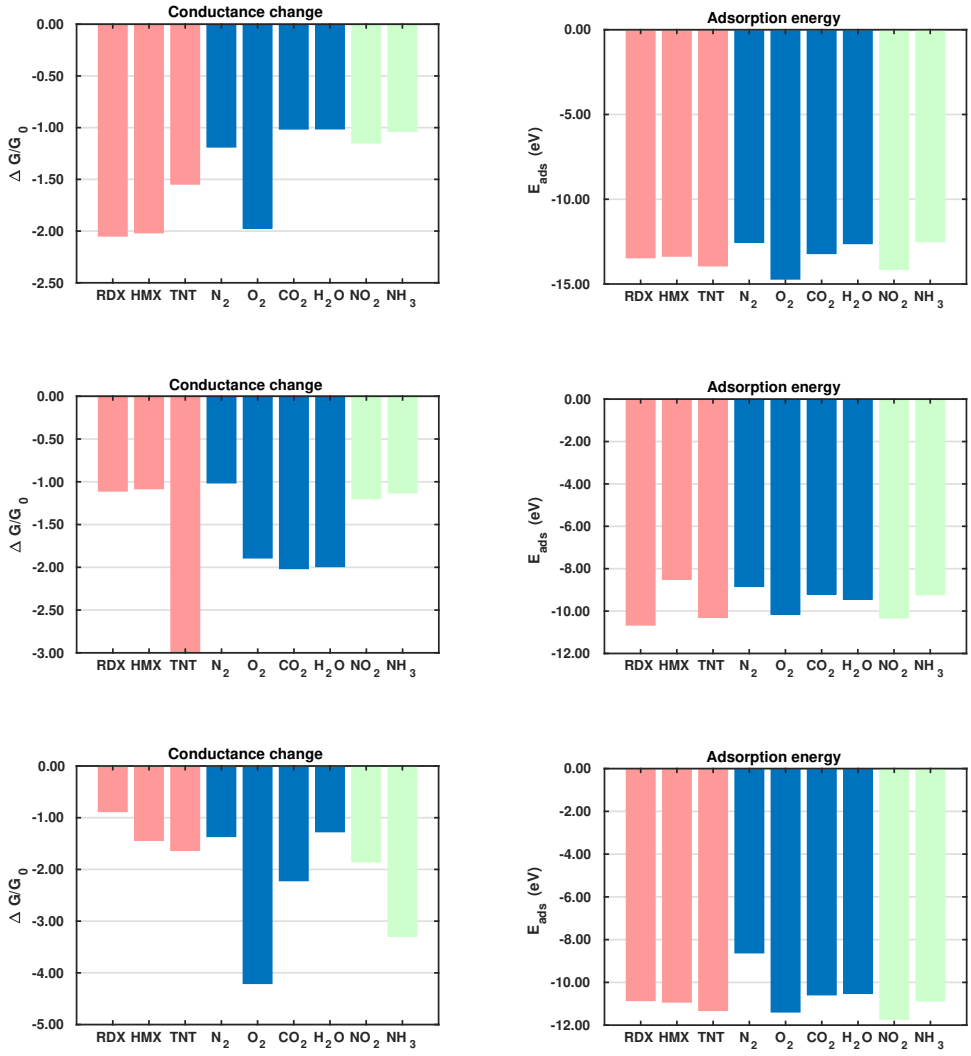

Figure 3.6: Conductance changes (left) and adsorption energy (right) due to analyte adsorption by alkali metal doped CNT(5,5): lithium doping (top row), sodium doping (middle row), and potassium doping (bottom row).

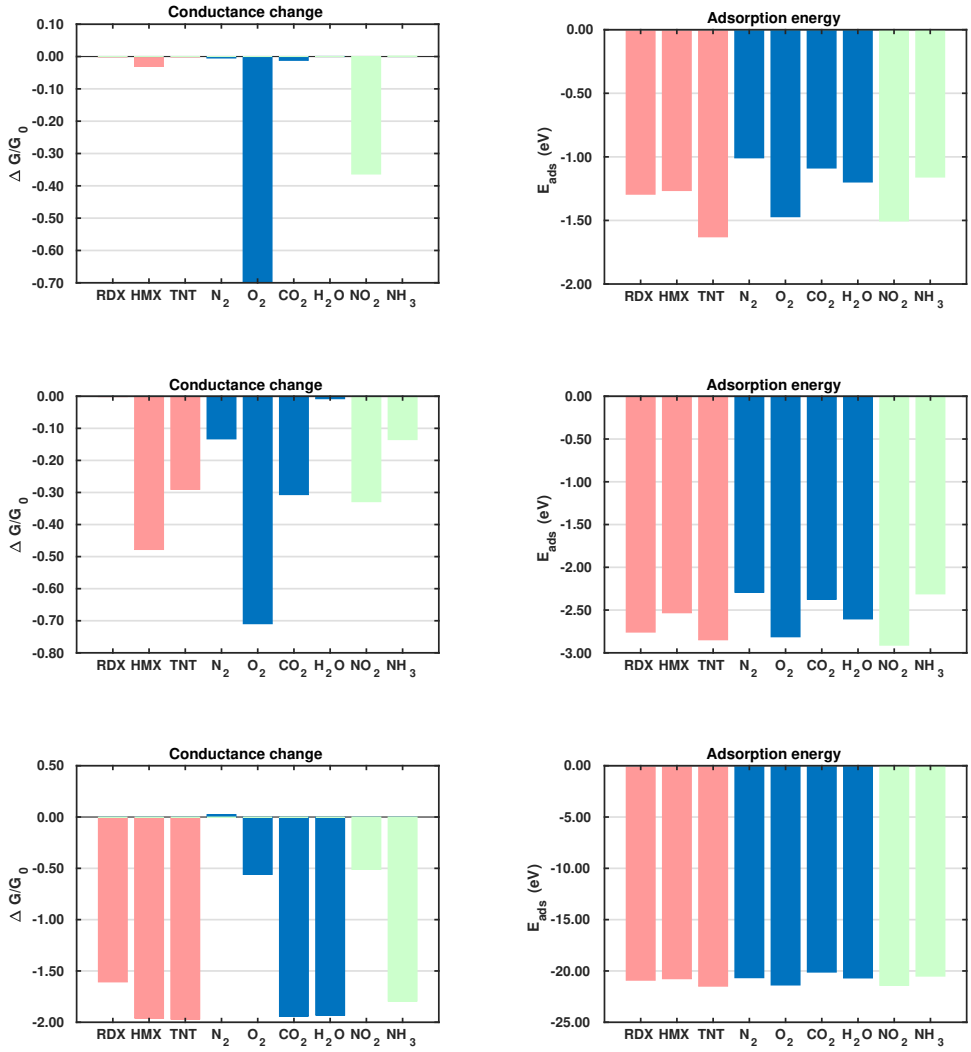

Figure 3.7: Conductance changes (left) and adsorption energy (right) due to analyte adsorption by interhalogen and alkali metal halide doped CNT(5,5): iodine monochloride doping (top row), iodine monobromide doping (middle row), and potassium iodide doping (bottom row).

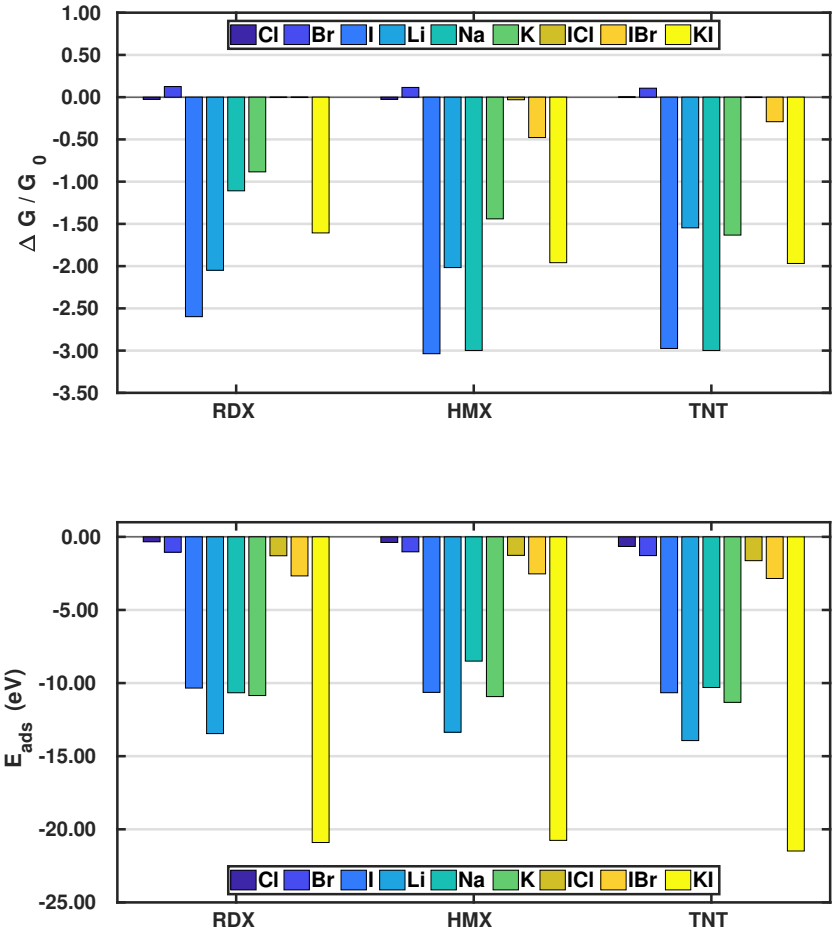

Figure 3.8: Conductance changes (upper chart) and adsorption energy (lower chart) for explosive molecule adsorption by nine different doped CNT(5,5): parameterization by explosive type.

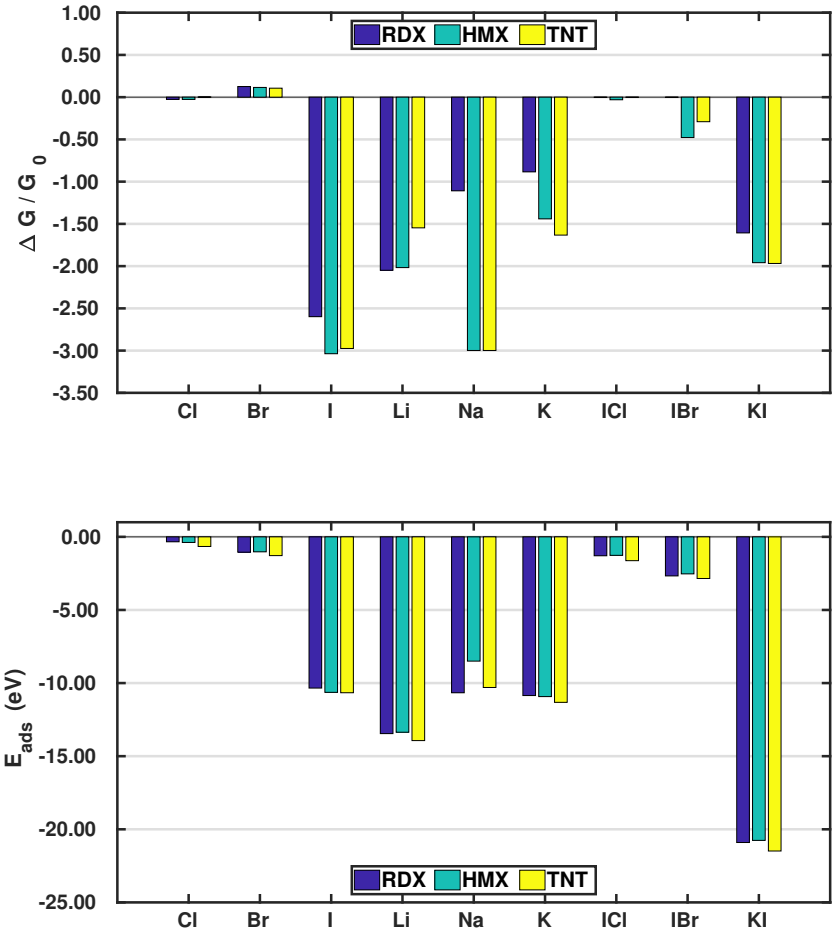

Figure 3.9: Conductance changes (upper chart) and adsorption energy (lower chart) for explosive molecule adsorption by nine different doped CNT(5,5): parameterization by dopant type.

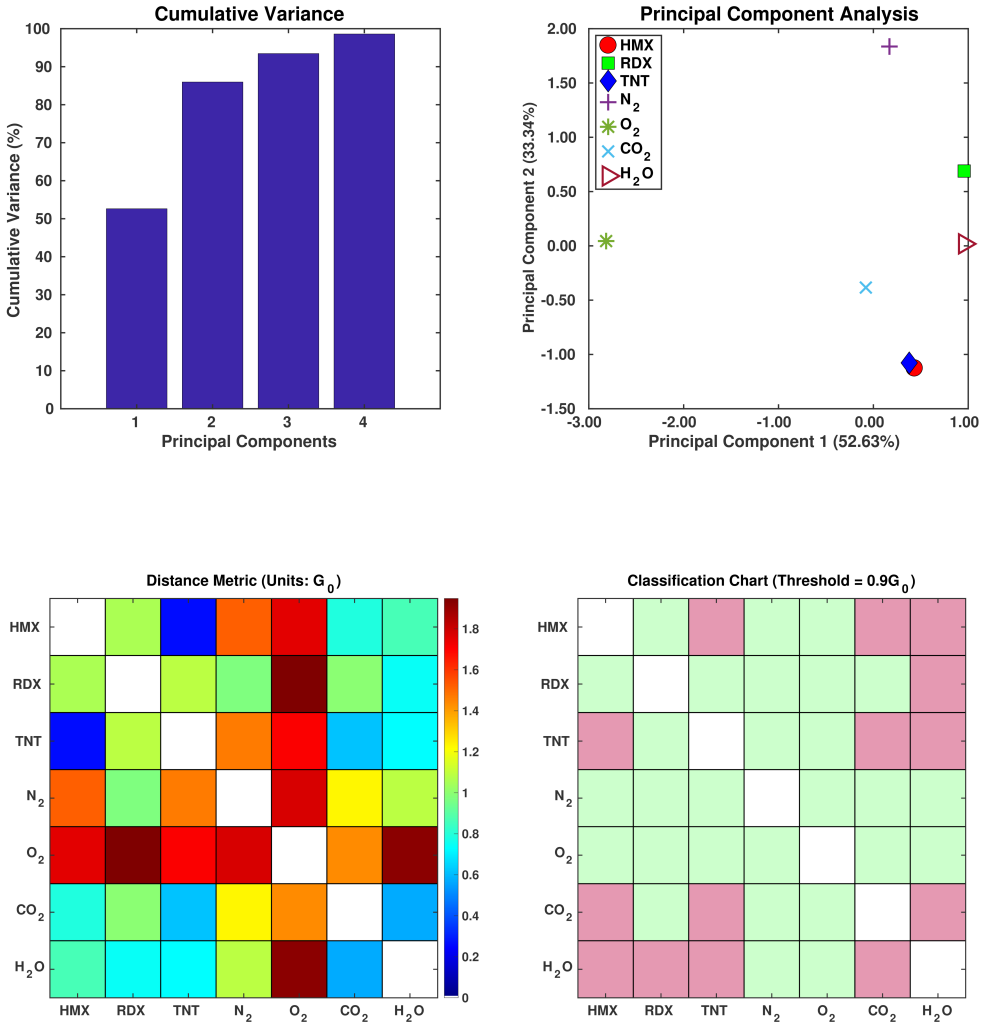

Figure 3.10: Principal Component Analysis of explosive sensing using a nine element array of internally doped CNT(5,5) sensors: cumulative variance plot (top left), illustration of analyte separation in a two principal component subspace (top right), distance metrics (lower left), and classification chart (lower right).

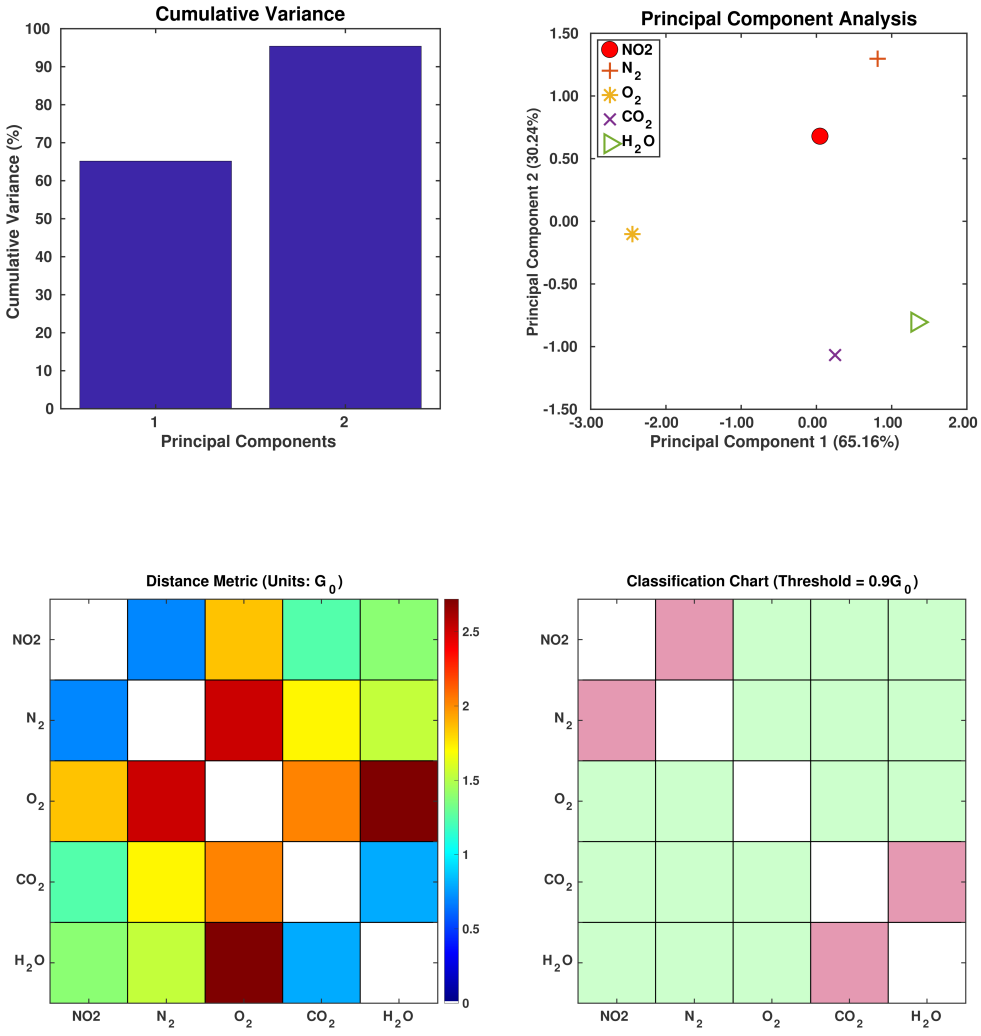

Figure 3.11: Principal Component Analysis of nitrogen dioxide sensing using a nine element array of internally doped CNT(5,5) sensors: cumulative variance plot (top left), illustration of analyte separation in a two principal component subspace (top right), distance metrics (lower left), and classification chart (lower right).

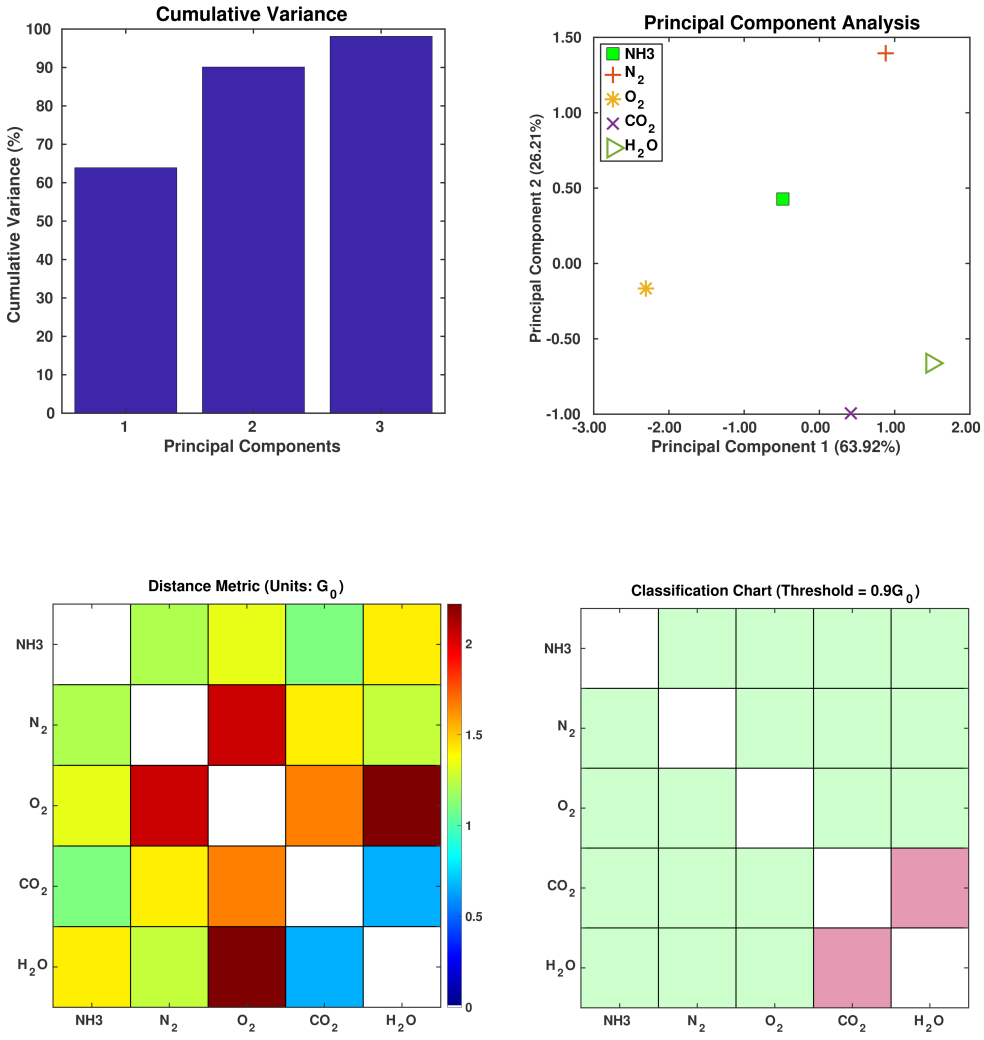

Figure 3.12: Principal Component Analysis of ammonia sensing using a nine element array of internally doped CNT(5,5) sensors: cumulative variance plot (top left), illustration of analyte separation in a two principal component subspace (top right), distance metrics (lower left), and classification chart (lower right).

Table 3.1: Conductance changes due to analyte adsorption for nine different doped CNT(5,5) sensors.

	Computed conductance change ($\Delta G/G_0$)								
Dopant:	**Cl**	**Br**	**I**	**Li**	**Na**	**K**	**ICl**	**IBr**	**KI**
HMX	-0.0262	0.1153	-3.0370	-2.0174	-2.9984	-1.4406	-0.0307	-0.4779	-1.9593
RDX	-0.0262	0.1258	-2.5984	-2.0490	-1.1086	-0.8842	-0.0014	-0.0013	-1.6069
TNT	0.0023	0.1064	-2.9748	-1.5469	-2.9985	-1.6328	-0.0014	-0.2904	-1.9686
N_2	-0.0175	0.1156	-2.2955	-1.1883	-1.0141	-1.3653	-0.0046	-0.1330	0.0239
O_2	-0.6471	-0.5558	-3.3768	-1.9728	-1.8917	-4.2074	-0.6986	-0.7093	-0.5595
CO_2	-0.0140	0.1259	-2.9746	-1.0142	-2.0163	-2.2195	-0.0119	-0.3067	-1.9404
H_2O	-0.0243	0.0941	-2.1064	-1.0129	-1.9927	-1.2733	0.0002	-0.0077	-1.9303
NO_2	-0.5260	-0.2119	-2.9718	-1.1486	-1.1993	-1.8556	-0.3635	-0.3287	-0.5112
NH_3	-0.0262	0.1259	-2.2374	-1.0378	-1.1325	-3.2920	0.0014	-0.1352	-0.7936

Chapter 4

Explosive Molecule Sensing at Lattice Defect Sites in Metallic Carbon Nanotubes

4.1 Introduction

Trace detection of explosive materials [70] presents a wide range of challenges. [73] In the gas phase, high sensitivity is often needed to address low vapor pressures [74], while good selectivity [75] is required to distinguish target analytes from background gases and other explosive molecules. There is considerable demand for mobile, low power sensing systems to replace mass spectrometers [76] or other traditional explosive detection devices which can be bulky, complex, and expensive. Hence recent research on hazardous gas sensing has placed considerable emphasis on the development of nanosensors [77, 78], including one and two dimensional nanocarbons [79, 80, 81].

Published experimental studies have tested carbon nanotube (CNT) based devices in gas sensing applications,[82, 83, 84, 85, 86, 87] and reported considerable success in detecting a wide range of molecules, from hydrogen [86] to complex nerve agents [87]. All of the papers just cited employed 'as produced' carbon nanotubes (CNTs). By contrast, studies employing 'pristine' nanotubes have generally measured weak interactions with analyte gases [80,

88, 89], suggesting that CNT defects play an important role in determining sensor performance. [90] Similarly, recent work [91] evaluated the effects of defects on the chemiresistive sensing properties of Field Effect Transistors (FETs) made from semiconducting CNTs. Plasma irradiation was used to intentionally add defects to the CNTs, and the presence of defects (primarily vacancies) was confirmed through Raman spectroscopy. The chemiresistive response to NO_2 of the CNT-FETs with added defects was much greater than those with the baseline level of defects, again showing that defects improve chemiresistive response.

A large body of CNT research has investigated lattice defects, which here refers to both structural flaws and substitutional deviations from a perfect network of sp^2 bonded carbon atoms. During the growth of CNTs substitutional 'doping' may occur when one or more of the carbon atoms are replaced by atoms of other elements. Nitrogen[92, 93] and boron [94, 95] are the most commonly studied substitutional dopants. Since CNTs doped by both these elements have shown good energy storage performance in batteries, controlled processes have been developed to apply such dopants on demand. The dopant elements produce local changes in the CNT structure [96] which enhance the surface reactivity of the nanotube [97] and may therefore also improve gas sensing performance. In published experiments, boron and nitrogen doped double-wall and multi-wall CNTs have shown an improved chemiresistive sensitivity for NH_3 and NO_2 detection [49, 97, 98]. Structural lattice defects (e.g. vacancies, divacancies, and and Stone-Wales defects) are also likely to occur

during CNT production [99, 100, 101] and are known to change the electronic properties of the nanotubes [102, 103]. Their sensitivity and selectivity effects on chemiresistive gas sensing have been investigated [90, 50] and been found to improve CNT performance in NH_3, NO_2 and H_2 detection.

It is important to note, given the extensive literature on CNT defects, that much published computational work infers improvements in sensing performance from property changes generated by the introduction of defects. Zhang et al. [104] studied the interaction of CNTs, substitutionally doped by palladium (Pd), with the decomposition products of SF_6. Based on calculations for adsorption energy, changes in the density of states (DOS) and HOMO-LUMO energy gaps, they concluded that the nature of the interaction of such CNTs with SO_2, H_2S, SOF_2, SO_2F_2, and CF_4 will be very species dependent. Similarly Kuganathan et al. [105] computed the adsorption energy, charge transfer, magnetic moment, charge density, and DOS for SO_2 and H_2 interaction with CNTs substitutionally doped by ruthenium (Ru). Based on large adsorption energy values, they inferred that Ru-doped CNTs may be good candidates for SO_2 and H_2 sensing. Demir et al. [106] studied a variety of properties (adsorption energy, HOMO-LUMO structures, charge density, DOS) for carbon monoxide interaction with CNTs substitutionally doped by platinum (Pt). Based on charge density difference plots and HOMO-LUMO energy gap data, they concluded that Pt doped CNTs could be used to detect carbon monoxide. With respect to structural defects, Andzelm et al. [107] studied adsorption energy, HOMO-LUMO structures, DOS, and Fourier-

transform infrared spectroscopy (FTIR) spectra for CNTs with Stone-Wales, vacancy, and interstitial defects, concluding that such nanotubes would perform well as ammonia sensors.

This research extends previous computational research on gas sensing using carbon nanotubes with defects, with the following focus:

- the target molecules are one nitroaromatic (TNT) and two nitramine (RDX and HMX) explosives; the response to four background gases (N_2, CO_2, H_2O, and O_2) is also computed, to determine the relative sensitivity of the CNTs to explosives and the selectivity of the modeled sensors in identifying various analytes;

- the modeled CNTs incorporate one of five different defects, two substitutional dopants (boron and nitrogen) and three structural defect types (vacancy, divacancy, and Stone-Wales);

- the five sensor types are evaluated for their performance as a sensor array, using Principal Component Analysis (PCA) to estimate the array's effectiveness in explosive molecule sensing.

Unlike previous work, since the introduction of defects renders the modeled metallic CNT sensing performance highly nonlinear, ab initio current transmission calculations are performed over a range of bias voltages (0.2 - 0.9 volts), at an increment of 0.1 volts. This provides an eight-fold increase in the sensor array degrees of freedom considered in the PCA, and is aimed at

improving the selectivity of the modeled sensing device, a central concern in chemiresistive sensing.

Initial computations for each combination of analyte and sensor type include: (1) adsorption energy, (2) zero-bias conductance, and (3) charge density difference distribution. Next, changes in the CNT current as a function of the applied bias voltage are computed and used to evaluate the chemiresistive sensing properties of the CNT-based array. Principal Component Analysis of the current data indicates that the defect based sensor array will show good sensitivity and selectivity, for all three explosives and for all four background gases included in the analysis, in particular distinguishing all three explosives from each other and from all four background gases.

4.2 Computational methods

The substitutional dopants and structural defects modeled in this chapter were applied to a metallic, single walled carbon nanotube of chirality (5,5), with a unit cell length of 2.46Å. Starting geometries for the background gases and explosives molecules are taken from published work [108, 109, 110]. The starting analyte molecule orientations assumed in this chapter were obtained from a preliminary analysis which identified the minimum energy orientations for analyte adsorption on a pristine CNT(5,5). A typical atom count for the models is 330. In the transport direction, the scattering zone was bounded by electrodes composed of pristine (5,5) nanotubes, modeling a conductor of infinite length.

Published work indicates that electronic transport through pristine CNTs occurs without spin polarization for hundreds of nanometers [111]. A computational study [112] on CNTs with Stone-Wales defects showed that the presence of a Stone-Wales defect does not induce spin polarization as long as the defect density is lower than one defect per nine unit cells. Our computations consider one defect per sixteen unit cells of CNT, much lower than the cited threshold. Computational studies [113, 91] also indicate that isolated vacancies do not cause spin polarization, since they undergo a 'reconstruction' of the type described later in the chapter. Hence the sensing models described in this chapter do not consider the effects of spin polarization. Finally note that recently published work [37] investigating surface adsorption processes for the same exchange correlation function, nanotube type, background mesh, and convergence criteria applied here found that van der Waals interaction effects were negligible.

4.3 Results and discussion

This section describes the ab initio modeling results for the response of the five CNT sensors to the seven analytes (three explosives and four background gases) considered in this chapter. The ab initio modeling results for the sensor current response are then used, in a Principal Component Analysis, to evaluate the performance of the sensor array for its sensitivity and selectivity in the detection of explosive molecules.

Fig. 4.1 depicts four of the total of 35 modeled sensor-analyte com-

binations, showing equilibrium configurations for HMX, RDX, TNT, and O_2 adsorbed on nitrogen-doped, boron-doped, divacancy flawed, and Stone-Wales defect flawed nanotubes respectively. Note that color distinguishes the dopant atoms and the CNT sidewall flaws, at which the analytes are adsorbed. To clarify the nature of the vacancy, divacancy, and Stone-Wales defects, Fig. 4.2 provides schematic descriptions of all three defects on a lattice segment with the same connectivities as the full lattice which makes up the sidewall. Figs. 4.3 and 4.4 plot adsorption energy (equation 1.6) and the change in zero bias voltage conductance (due to adsorption, equation 1.5) for all five sensors and all seven analytes considered in this chapter. Modeling results for a pristine CNT sensor and for two widely studied hazardous gas analytes (NO_2 and NH_3) are also included in these two figures, for reference in discussions of previous work. Note that Figs. 4.3 and 4.4 break out the O_2 and NO_2 adsorption results in separate plots, since the chemiresistive sensitivity to those analytes is, in comparison to the other species, rather high.

4.3.1 Pristine CNT response

In the pristine CNT sensor case, all of the analyte molecules reduce the CNT conductance, however the change is significant only for O_2 and NO_2 (see Fig. 4.3). The relatively high computed sensitivities to O_2 and NO_2 are consistent with experiment [114, 43] and reflect the strong electron-withdrawing properties of O_2 and NO_2. With respect to the explosives, TNT produces a slightly larger change in conductance than the nitramines, and all three explo-

sives show higher adsorption energies than the background gases. Consistent with the modeling results, experiments on pristine CNTs have generally shown low sensitivity and low selectivity [80, 115]; pristine CNTs have however been been shown to detect O_2 [82, 116, 117] and NH_3 [118]; the conductance change results presented here are sign consistent with the cited experiments. Experimental work sensing ammonia [119] has shown a relatively small drop in conductance, also consistent with the modeling results.

4.3.2 Doped CNT response

As nearest neighbors with carbon in the periodic table, nitrogen and boron are known to sometimes replace carbon atoms in CNTs; this effect has been studied in battery applications [120, 121, 122]. Consistent with experiment, [97] the equilibrium analyses conducted here show that both nitrogen and boron can replace carbon without distorting the CNT lattice. Figs. 4.5 and 4.6 provide charge density difference plots which depict equilibrium configurations for all three modeled explosives, and for an oxygen molecule, adsorbed on both nitrogen and boron substitutional dopant sites.

In the case of nitrogen, both in situ doping [92, 93] and post treatment methods [123, 124] have been used to produce substitutionally doped CNTs, which have been evaluated in NH_3, NO_2 and H_2O detection experiments [49]. As indicated in Fig. 4.3, O_2 sensing shows the largest change in conductance and NO_2 shows the largest adsorption energy. The computed change in conductance for NO_2 sensing is sign consistent with experimental

studies on single-wall [49, 84] and and double-wall [98] CNTs. With regard to the explosives, TNT shows the largest adsorption energy while RDX shows a change in conductance which differs in sign from those of the other explosives. Note that such distinctions can be very important in determining the selectivity properties of sensor arrays. In the case of boron, substitutional doping has been accomplished using laser ablation [94], arc discharge [95], chemical vapor deposition [125], and post-manufacturing reactions [126]. As indicated in Fig. 4.3, the modeling results indicate that O_2 and NO_2 show the largest sensitivity. With regard to the explosives, TNT shows the largest adsorption energy as well as a change in conductance which differs in sign from those of the nitramines.

Comparing the sensing results for the two substitutional doping cases, the conductance change results frequently differ in sign, perhaps since nitrogen n-dopes carbon while boron p-dopes carbon. The response to oxygen is consistently a large negative change in conductance. These results would generally support array selectivity, in the case of oxygen by isolating this analyte in the sensor response space.

4.3.3 Defective CNT response

The removal of atoms from a CNT can produce vacancy defects of several types, which can significantly change the electrical, chemical, and mechanical properties of CNTs. [127, 128, 129] Of specific interest here are the changes in electrical conductance due to the adsorption of analytes at these

sites. Figs. 4.7- 4.9 provide charge density difference plots which depict equilibrium configurations for all three modeled explosives, and for an oxygen molecule, adsorbed on monovacancy, divacancy, and Stone-Wales defect sites.

If only one carbon atom is missing from the sidewall, the defect is called a monovacancy or simply a vacancy defect. The mechanical effects of such defects on CNTs have been widely studied [127, 130, 128]. Recombination of the two-atom coordinated carbons at the defect forms a pentagonal structure (a Jahn-Teller distortion [91]), which has been observed in experiments and previous computational studies [131, 99]. Here the conductance modeling results (Fig. 4.4) indicate that all three of the explosives and H_2O show a large response to the vacancy defect, and that TNT and NO_2 show the largest adsorption energies. The closest reported experimental work has been on semiconducting CNTs, which showed a reduction in the conductance of defective CNTs upon exposure to ammonia [44, 50]. The present computational work, which considers metallic nanotubes, also shows a reduced conductance.

If two neighboring carbon atoms are removed from the sidewall, a divacancy defect is produced. Recombination of the neighboring carbon atoms creates two pentagonal rings and one 8-membered ring. Divacancy defects are common at room temperature in CNTs and affect their electrical and mechanical properties [128, 132]. The modeling results for sensing at these defects are shown in Fig. 4.4. Note that O_2 and NO_2 show negative changes in conductance, while the other analytes show positive changes in conductance. The explosives show relatively large conductance changes, as compared to most of

the analytes, however as in the case of substitutional doping oxygen sensitivity is high. Comparing the vacancy and divacancy defects, there are significant differences in the computed response. The magnitudes of the adsorption energies and the magnitudes of the conductance changes are much higher in the monovacancy case than in the divacancy case, apparently since monovacancy defects result in a carbon atom bonded to only two neighbors, instead of three. This creates a highly reactive site [91] which attracts any analyte.

The third defect modeled here is a Stone-Wales defect, which takes a pentagon-heptagon shape. Two π-bonded C atoms rotate by 90° along the mid point of their common bond, converting four adjacent 6-atom rings to two 5-atom rings and two 7-atom rings. [129, 133, 134] The modeling results shown in Fig. 4.4 indicate that the response is strongest to O_2, NO_2 and TNT. Among the explosives, TNT shows a change in conductance which is opposite in sign to those for the nitramines, and TNT also shows a larger adsorption energy. The present modeling work on NH_3 and NO_2 shows adsorption energies which are consistent with a previous computational study of Stone-Wales defects in graphene [135]. Note that the overall analyte response to the Stone-Wales defect is qualitatively similar to that for a pristine CNT. In both cases all of the carbon atoms in the sidewall remain bonded to three other carbon atoms.

4.3.4 Current-voltage characteristics

The preceding discussion has emphasized the somewhat disparate zero-bias conductance characteristics of five chemiresistive sensors defined by intro-

ducing lattice defects, of either the substitutional or vacancy type, to a pristine metallic CNT. Since such defects would be expected to produce a nonlinear current response under bias voltage loads, I-V characteristic curves for each sensor-analyte combination were computed, covering the bias voltage range 0.2-0.9 volts. Assuming a bias voltage interval of 0.1 volts, this creates a (non-degenerate) eight-fold larger discrete description of a sensor array response which can be employed in a 'pattern matching' algorithm (such as Principal Component Analysis) to add sensitivity to a chemiresistive sensing device. Fig. 4.10 plots the current-voltage characteristics of all five sensors, where the plotted response is the current increment defined by equation (3). As expected from the zero-bias conductance results, the current changes for oxygen adsorption are relatively high, hence they are presented separately on a sixth plot which includes results for all five sensor types. Although I-V curves for the nitrogen dioxide and ammonia analytes were not computed, they could be generated in order to perform a hazardous gas analysis similar to one presented in this chapter for explosives.

As in the case of the zero-bias conductance calculations, the current response results show disparate trends. In the case of the nitrogen-doped sensor, the RDX and TNT curves show opposite signs while the current curve for HMX is near zero. Comparing the nitrogen-doped and boron-doped sensors, the current responses for RDX and TNT differ in sign. In the case of the vacancy and divacancy defect sensors, the response trends are non-monotonic. In the case of the Stone-Wales defect, the current response for TNT differs

sharply from that of all the other analytes, including oxygen. Overall the results support the suggested selectivity analysis approach.

4.3.5 Principal Component Analysis

An evaluation of the sensor array performance was made by performing a principal component analysis (PCA) of the data plotted in Fig. 4.10. Note that the dimensions of the principal components, distance metrics, and classification threshold used in this chapter are microamps.

Fig. 4.11 (top left) shows the cumulative variance plot for the CNT sensor data set; only two principal components are needed to account for 95% of the variance in the sensor output data set. Fig. 4.11 (top right) shows the separation of the seven analytes (three explosives and four background gases) in the reduced order principal component space. Note in the Distance Metrics (Fig. 4.11, lower left) the clear separation of oxygen from all the remaining analytes, the close proximity of the N_2 and CO_2 coordinates in principal component space, and the distances separating the three explosive molecules from all of the other analytes. As indicated in Fig. 4.11 (lower right), where green squares denote distinguishable analyte pairs, if a classification threshold of 0.5μA is chosen for this data set the sensor array shows excellent selectivity. All the explosives can be distinguished from all of the background gases, and from each other. The only indistinguishable analytes are N_2 and CO_2. A review of published data on measured sensor currents in hazardous gas detection experiments [136, 137, 82] suggests that the classification threshold chosen here

is reasonable, perhaps conservative, and that selective detection of explosive molecules using defect modulated metallic CNTs is feasible.

4.4 Summary

Trace detection of explosives using carbon nanotube based sensors has attracted much research attention, since it might produce a light weight, low power, low cost solution to a hazardous materials detection problem of very wide military, government, and commercial interest. Chemiresistive sensing solutions often provide simplicity and robustness, but lack selectivity. Building on previous experimental and computational work on the study of defects in carbon nanotubes, and their effects on chemiresistive sensing performance, the present chapter suggests that sensor arrays which capitalize on the nonlinear response of substitutionally doped and structurally flawed metallic CNTs may offer opportunities for sensitive and selective detection of explosive molecules. Although this chapter considers only basic sensing mechanisms, it does motivate further research exploring the sensing scheme developed here and extension of the approach to address other hazardous gas sensing applications.

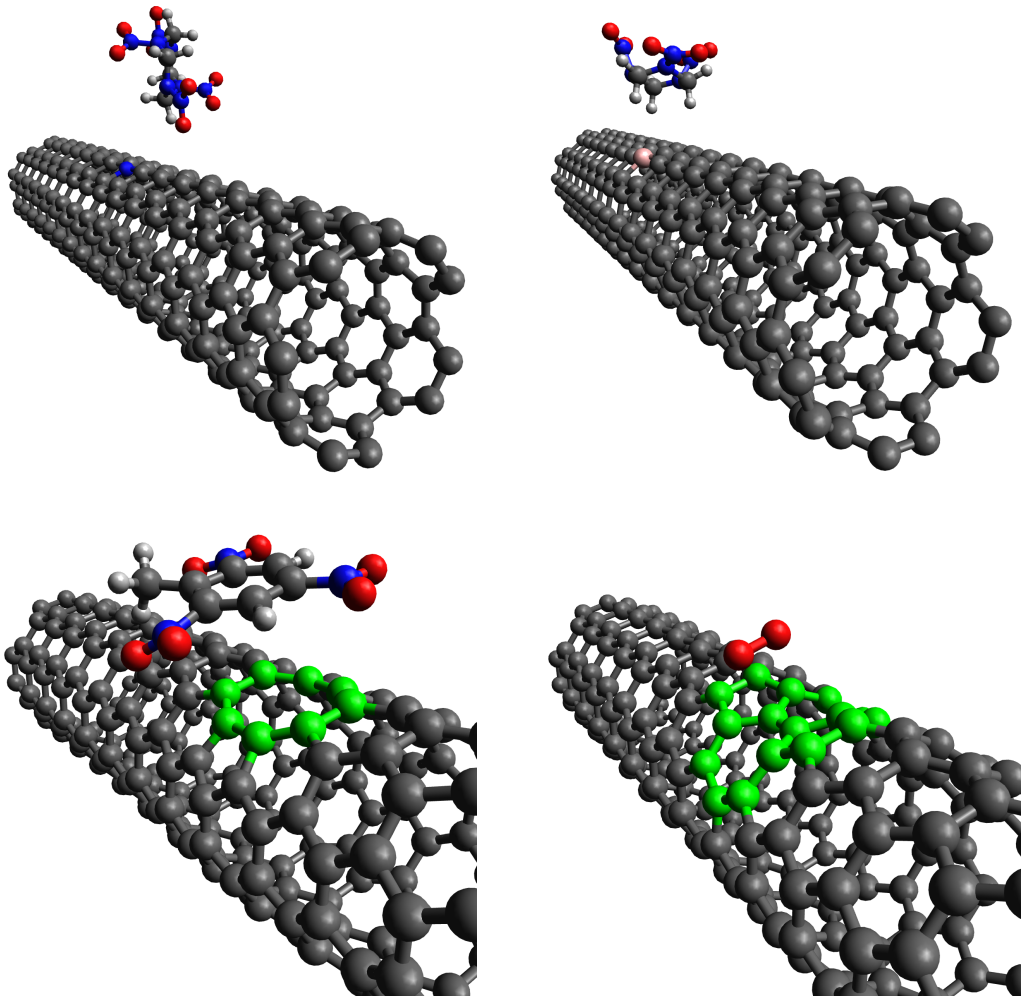

Figure 4.1: Computational models: HMX adsorption on CNT(5,5) with substitutional doping by nitrogen (top left), RDX adsorption on CNT(5,5) with substitutional doping by boron (top right), TNT adsorption on CNT(5,5) with a divacancy defect (bottom left), and O_2 adsorption on CNT(5,5) with Stone-Wales defect (bottom right). In the lower row of figures, the carbon atoms associated with the defects are highlighted in green.

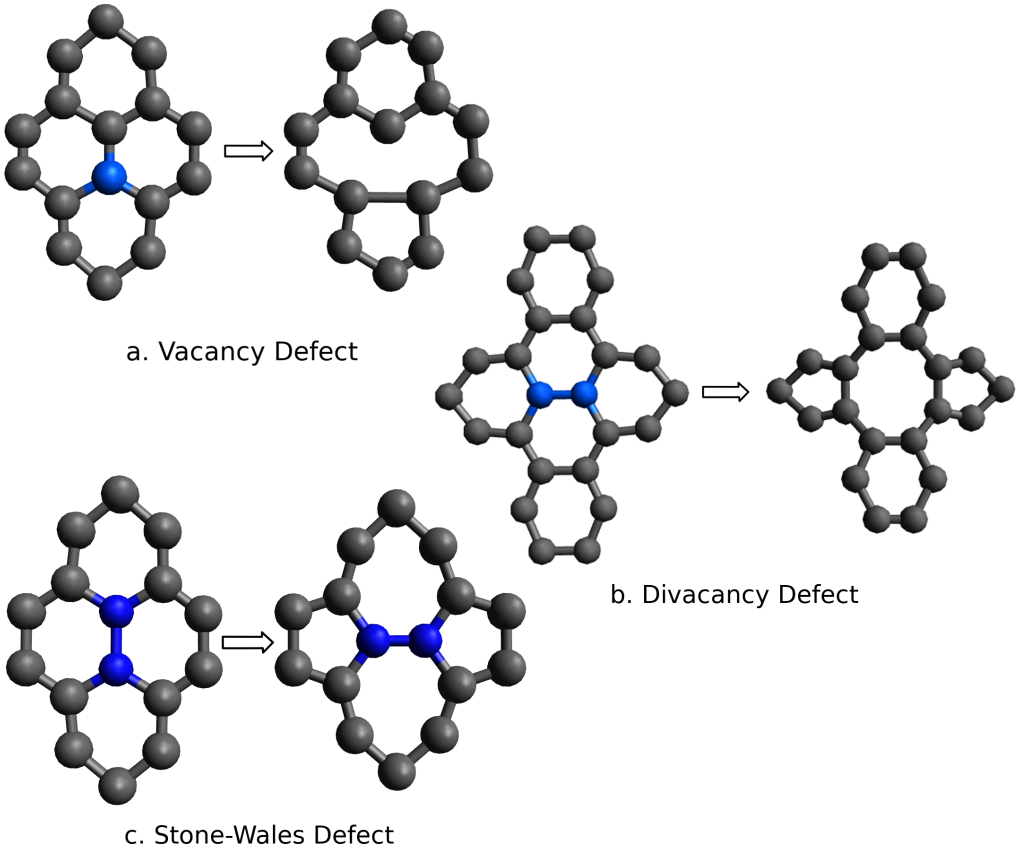

Figure 4.2: Schematics descriptions of three defects in a metallic CNT; the atoms highlighted in blue are either missing (vacancy and divacancy defects) or realigned (Stone-Wales defect).

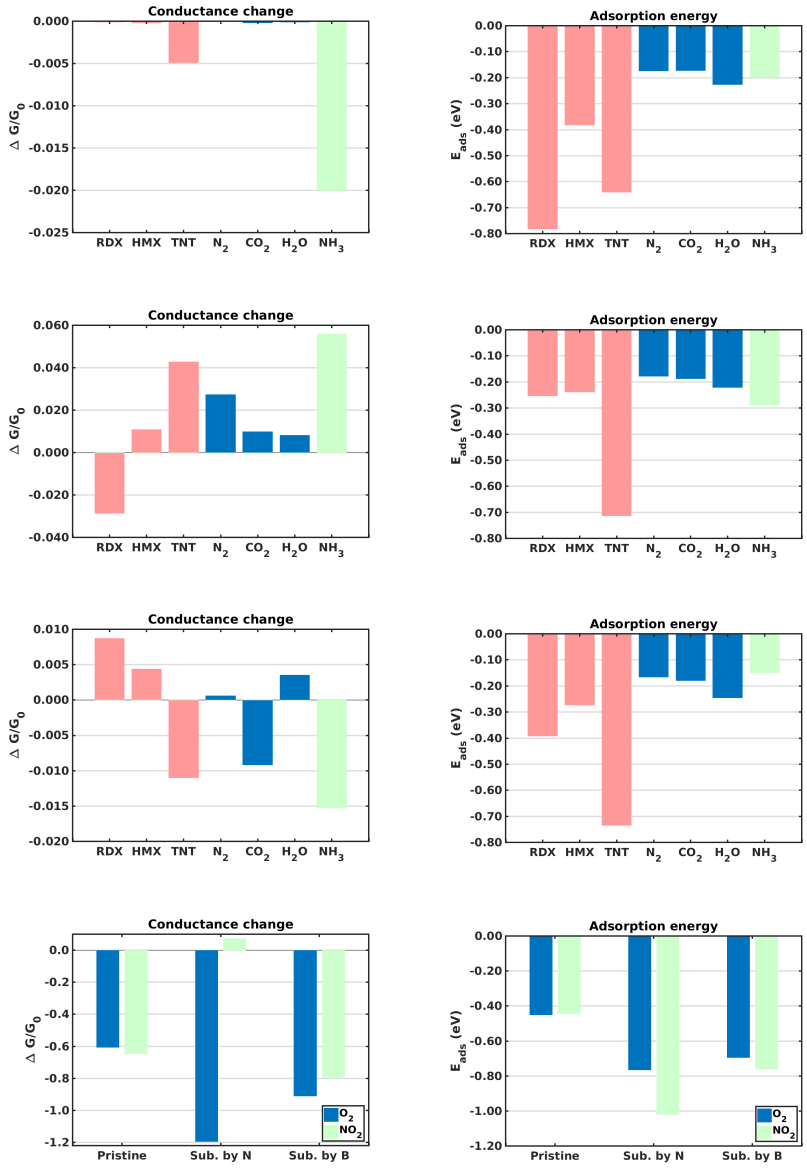

Figure 4.3: Computational results for the change in conductance due to analyte adsorption and adsorption energy, for a pristine CNT(5,5) (top row), a CNT (5,5) with substitutional doping by nitrogen (second row), and a CNT (5,5) with substitutional doping by boron (third row). The lower row shows similar computational results for O_2 and NO_2, parameterized by sensor type.

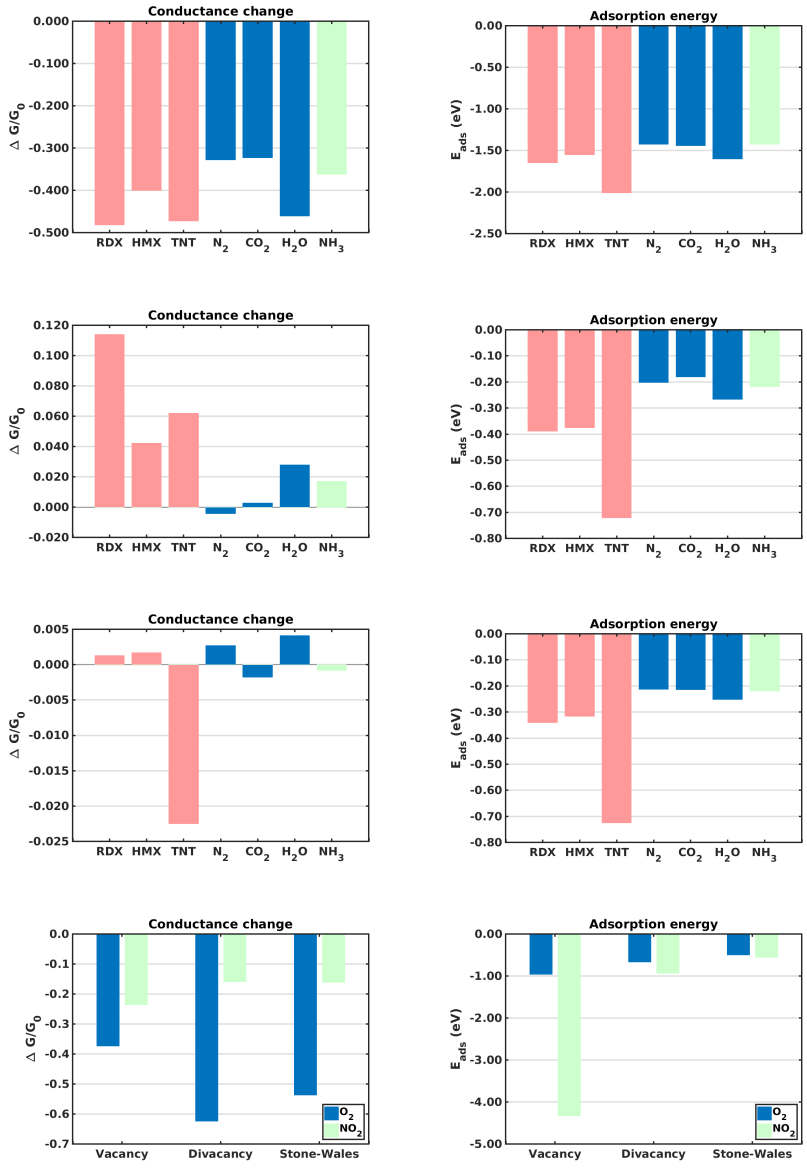

Figure 4.4: Computational results for the change in conductance due to analyte adsorption and adsorption energy, for a CNT(5,5) with a vacancy defect (top row), a CNT (5,5) with a divacancy defect (second row), and a CNT (5,5) with a Stone-Wales defect (third row). The lower row shows similar computational results for O_2 and NO_2, parameterized by sensor type.

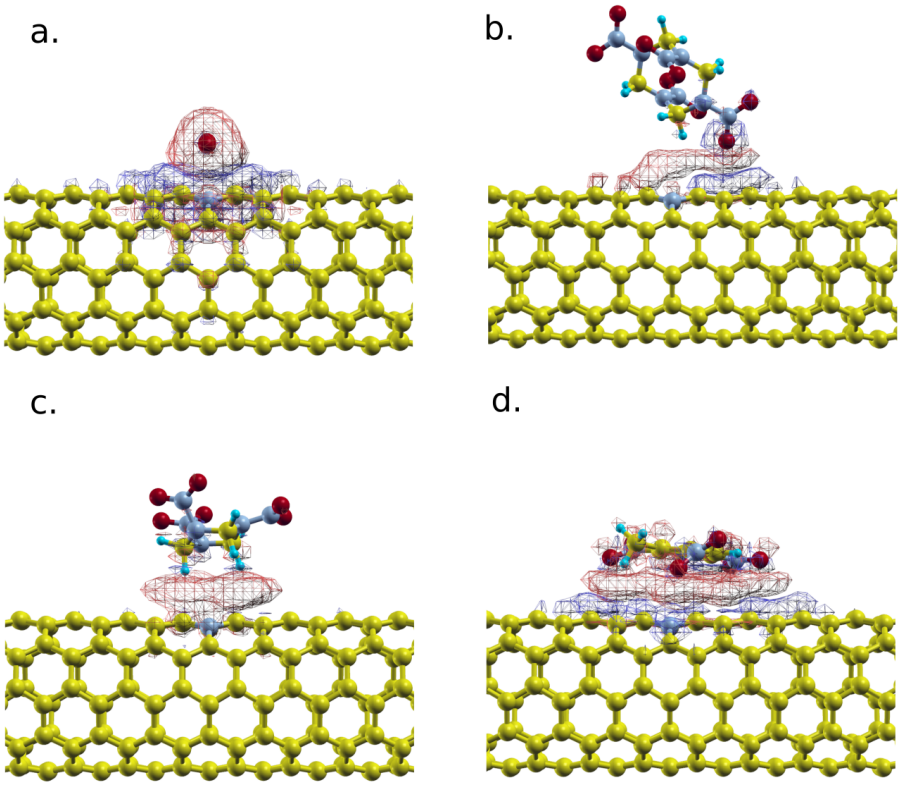

Figure 4.5: Charge density difference plots for sensing by a nitrogen-doped CNT(5,5): (a) O_2 sensing, (b) HMX sensing, (c) RDX sensing, and (d) TNT sensing

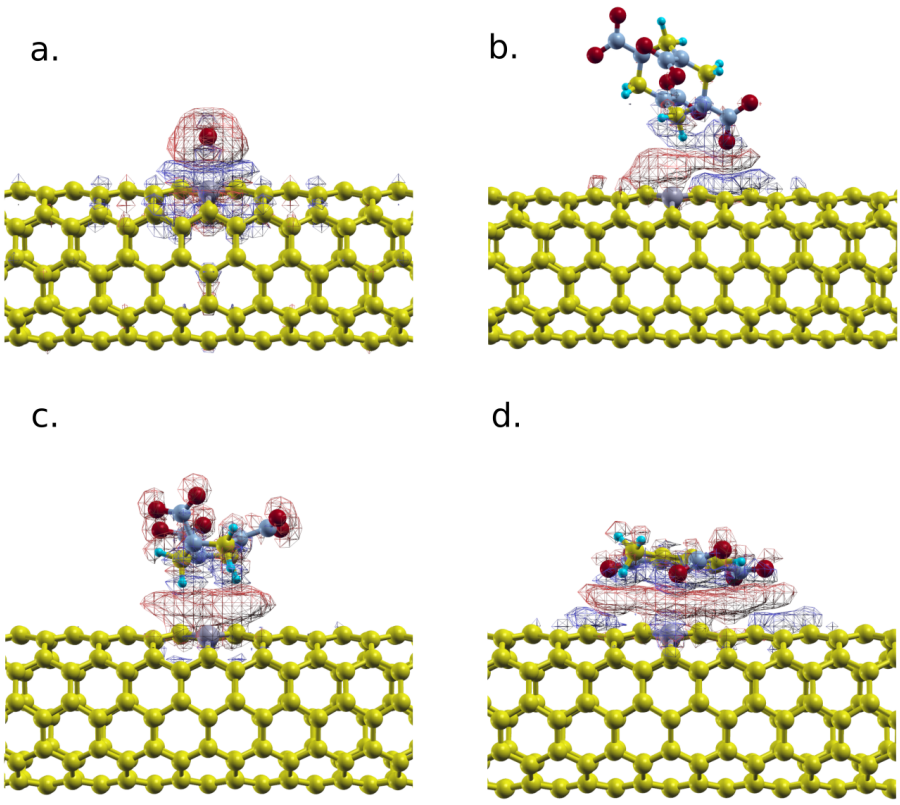

Figure 4.6: Charge density difference plots for sensing by a boron-doped CNT(5,5): (a) O_2 sensing, (b) HMX sensing, (c) RDX sensing, and (d) TNT sensing

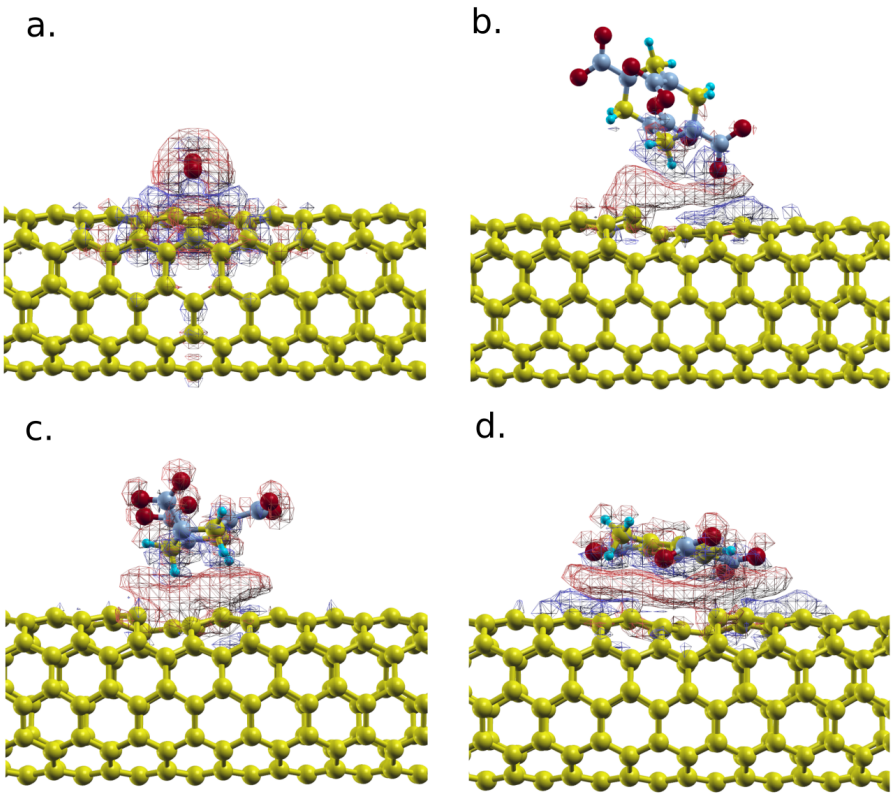

Figure 4.7: Charge density difference plots for sensing by a CNT(5,5) with a vacancy defect: (a) O_2 sensing, (b) HMX sensing, (c) RDX sensing, and (d) TNT sensing

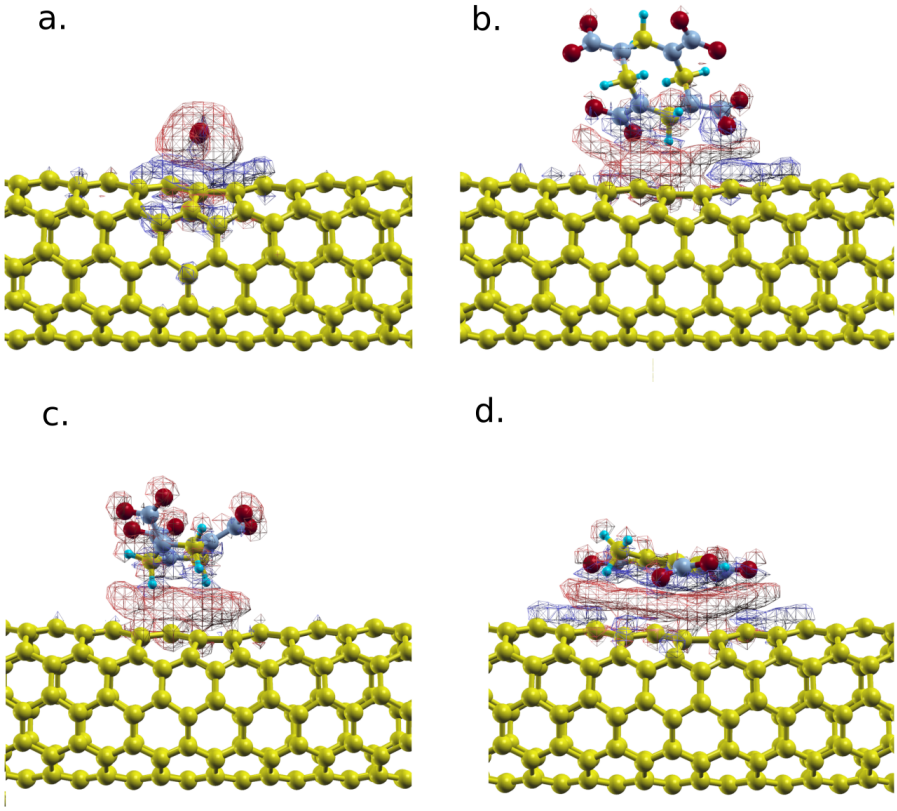

Figure 4.8: Charge density difference plots for sensing by a CNT(5,5) with a divacancy defect: (a) O_2 sensing, (b) HMX sensing, (c) RDX sensing, and (d) TNT sensing

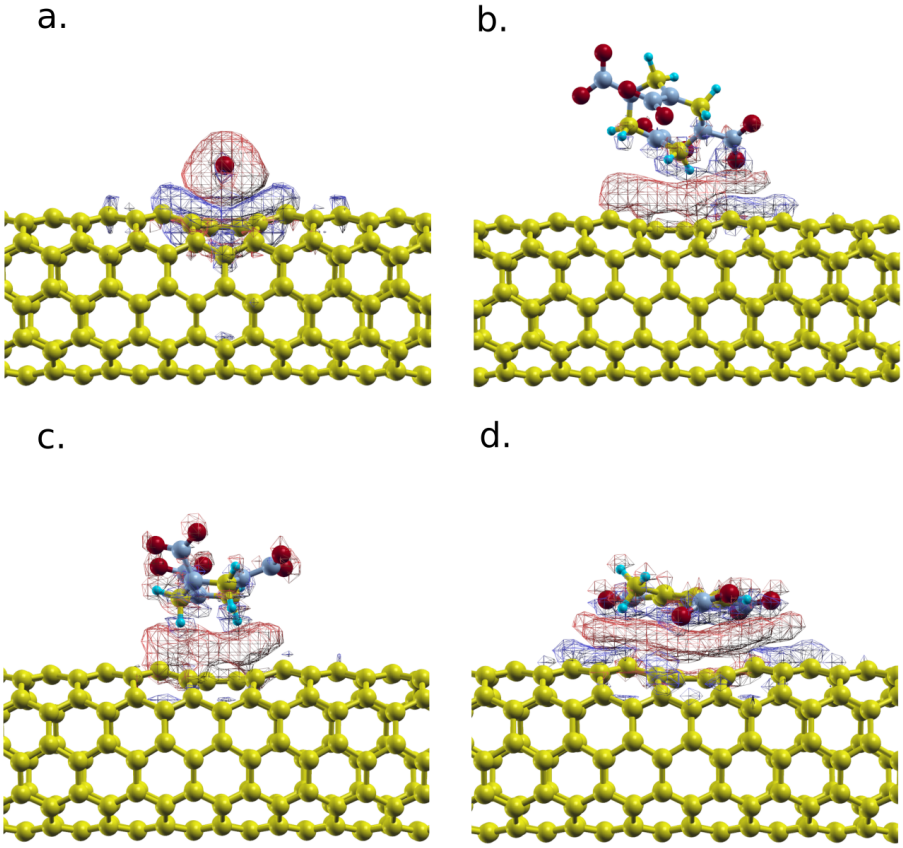

Figure 4.9: Charge density difference plots for sensing by a CNT(5,5) with a Stone-Wales defect: (a) O_2 sensing, (b) HMX sensing, (c) RDX sensing, and (d) TNT sensing

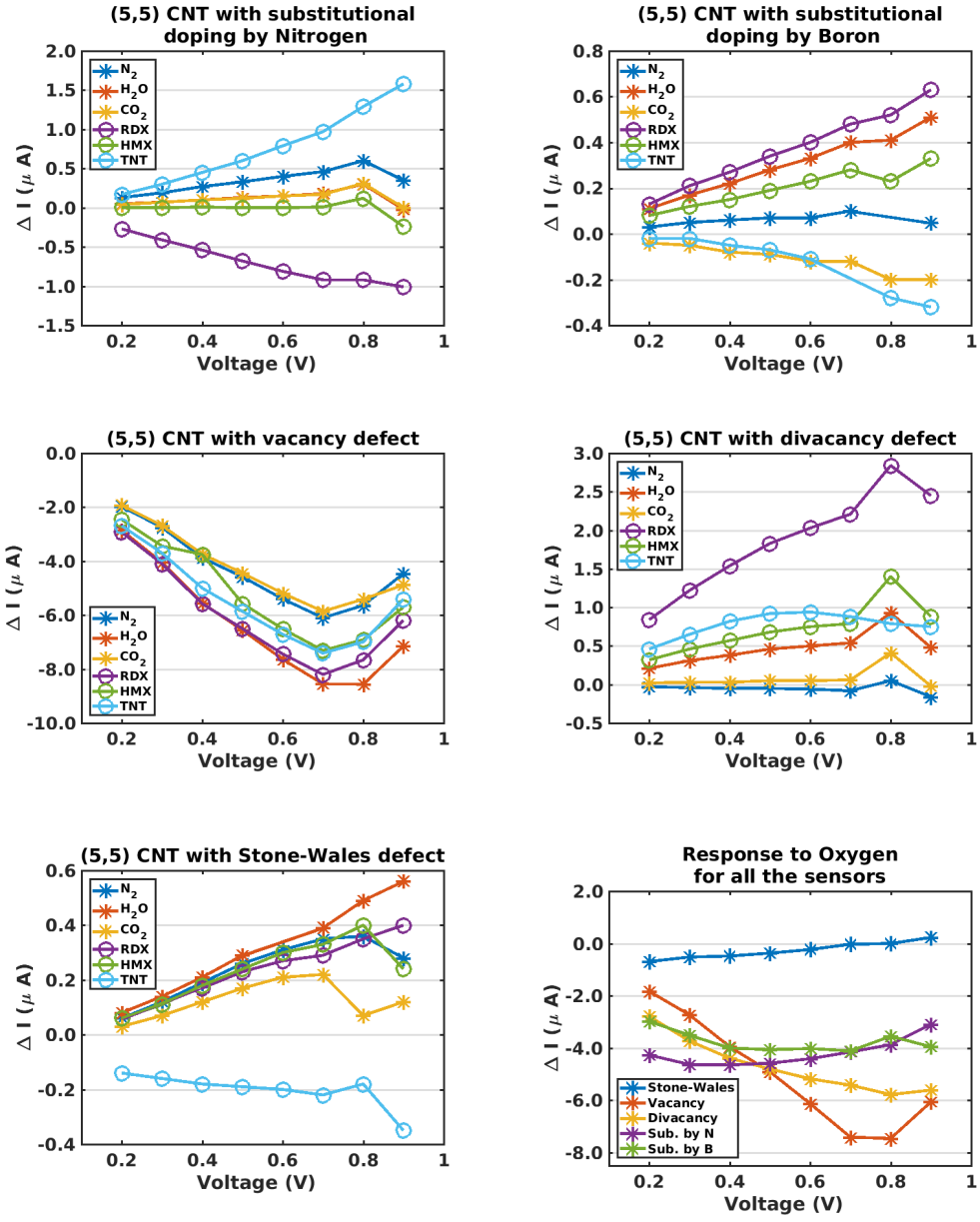

Figure 4.10: Current increment versus voltage characteristic curves for CNT(5,5) sensors with substitutional doping or structural flaws, due to adsorption of an explosive or background gas molecule. The bottom right plot isolates the computational results for oxygen, for all five sensor types.

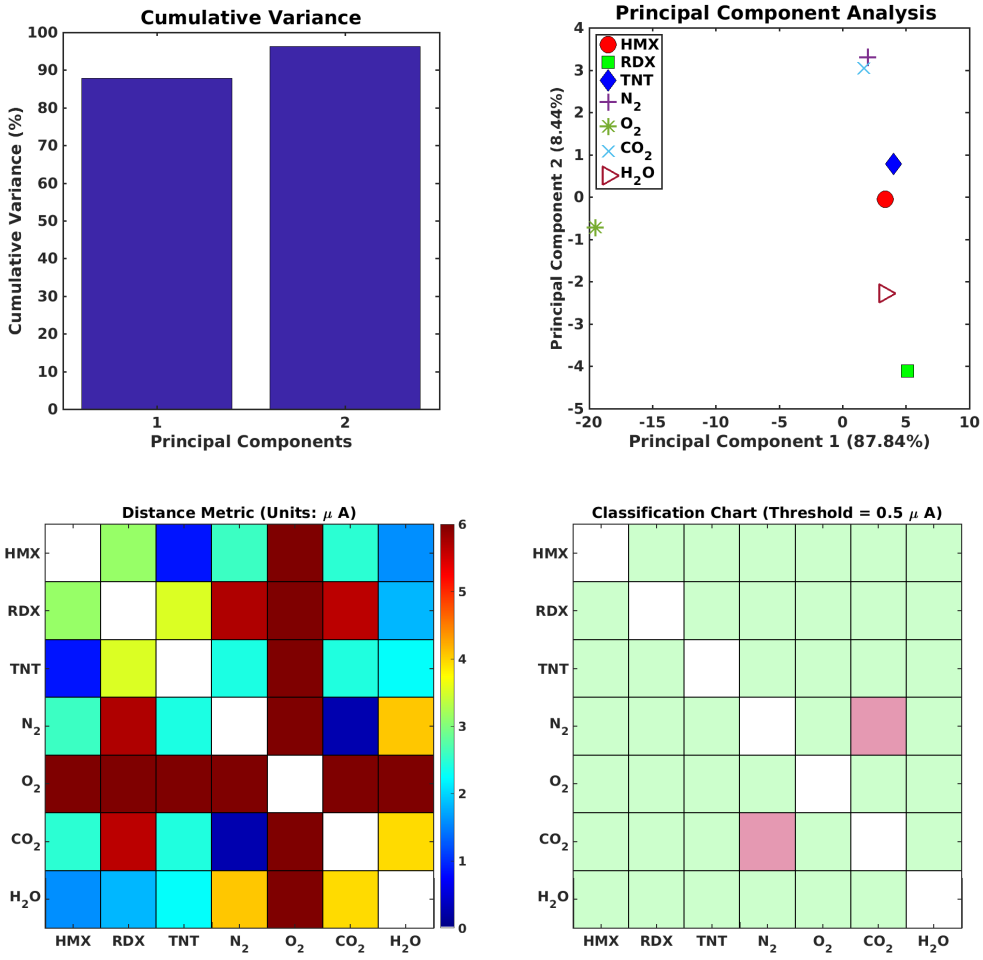

Figure 4.11: Principal Component Analysis results for sensing of an explosive or background gas molecule, using an array of five CNT(5,5) sensors with substitutional doping or structural flaws, over a bias voltage range of 0.2-0.9 volts: Cumulative Variance plot (top left), reduced order principal component space plot (top right), Distance Metric plot (lower left), and Classification Chart (lower right). In the Classification Chart, green squares denote distinguishable analyte pairs for a classification threshold of 0.5 μA .

Chapter 5

Functionalized Metallic Carbon Nanotube Arrays for Gas Phase Explosives Detection

5.1 Introduction

Hazardous gas detection [138, 139] is an important focus of chemical sensing research, and includes species which can be toxic at very small concentrations (NO_2, NH_3), common gases which can present dangers outside specific concentrations ranges (CO_2, O_2), and other analytes (DNA, explosives) of interest for non-biohazardous reasons. The last cited analyte class has motivated research on single molecule detection systems. [140] Sensing of explosives is a particularly challenging task: most explosives have low room temperature vapor pressures, [77, 74] demanding high sensitivity, and many explosives share similar functional groups, demanding high selectivity.

Much recent research on gas detection has investigated chemiresistive sensing [141, 142]. Solid state, [143] metal-oxide [80] or conducting polymer [79] based devices are widely used in detecting hazardous gases such as CO [144], and carbon nanotube (CNT) chemiresistive sensors have been developed for the detection of common gases like CO_2, NO_2 and NH_3 [145, 146, 147]. As compared to traditional gas identification and concentration measurement sys-

tems (mass spectrometer, gas chromatograph, residual gas analyzer, Fourier transform infrared spectrometer) [79], chemiresistive sensors typically reduce bulk, weight, cost, and power requirements. However they often lack selectivity.

Carbon nanotubes have attracted considerable attention as sensor materials, [148] because of a number of favorable properties, including low mass density, large aspect ratios, large specific surface areas, good mechanical properties, and tunable electrical properties [23]. These properties are well suited for the design of robust and portable chemiresistive sensors. Single walled carbon nanotubes (SWCNTs), which consist entirely of surface atoms, have an especially high surface area to volume ratio [79] and can show a high sensitivity to adsorbates. Other potential advantages to CNTs, over traditional materials, include room temperature operation and a high potential for miniaturization of large sensor arrays [80].

Functionalization of CNTs is frequently used to improve their sensitivity and selectivity; [79, 149, 150] it may be covalent or non-covalent. One non-covalent functionalization involves the wrapping of conducting polymers around the CNT. Some experiments on CNT sensors with non-covalent polymer functionalizations have exhibited impressive chemiresistive sensing properties for a wide range of gases [151, 152, 153], including certain explosives [3, 2]. Covalent functionalization links small organic molecules or metal particles to the CNT surface, and is generally performed with oxygen or nitrogen containing groups such as OH, COOH, NH_2, etc. [80]. As compared to noncovalent

polymer functionalization, the literature on covalent functionalization of CNTs for gas sensing is very limited. In some published experiments, CNTs with OH functionalization showed improved chemiresistive response to various organic vapors [154] and pollutant gases [16, 155]. In other published experiments, COOH functionalized sensors showed good chemiresistive response to ammonia [48, 16, 156], ethanol [157], methane, [158] and carbon monoxide [156, 158]. Similarly a computational study by Zhang et al. [155], which inferred chemiresistive sensing performance by evaluating adsorption energies, HOMO-LUMO structures, densities of state, and charge transfer, suggested good sensing performance for OH functionalized SWCNTs adsorping SO_2, CF_4, SO_2F_2, and SOF_2.

This chapter suggests the development of a sensor array, composed of covalently functionalized metallic SWCNTs, for the selective detection of gas phase explosives. Ab initio models are used to estimate the chemiresistive response of each sensor to three widely used explosives and common background gases. Principal Component Analysis (PCA) is then used to estimate the ability of a sensor array composed of five CNTs (with four with distinct covalent functionalizations) to selectively detect both nitroaromatic and nitramine explosives. The results indicate that the sensor array can distinguish common background gases from both classes of explosives, selectively identity nitroaromatics and nitramines, and distinguish very similar nitramine explosives from each other.

5.2 Computational methods

The scattering zone model consisted of a metallic CNT with chirality (5,5), plus functionalization and analyte. The total length of the nanotube models was 16 unit cells, for a unit cell length of 2.46Å, which corresponds to an atom count of 320. In the transport direction, the scattering zone was bounded by electrodes consisting of identical CNTs, in order to represent a conductor of infinite length. Starting geometries for the analyte molecules are taken from published work [108, 109, 110]. Starting orientations for the analyte molecules are based on minimum energy orientations obtained by modeling analyte adsorption on a pristine CNT(5,5).

5.3 Results and discussion

Computational evaluation of the proposed sensor array, described in this section, proceeds as follows:

- five sensor types are considered; they are a pristine metallic (5,5) carbon nanotube and CNTs of the same type functionalized with hydroxyl (OH), carboxylic acid (COOH), oxygen (COC), or amine (NH_2) groups;
- adsorption energy and zero bias conductance are computed for all combinations of the five sensor types and the following seven analytes: one nitroaromatic explosive (TNT) and two nitramines (HMX and RDX), plus four background gases (N_2, O_2, CO_2, and H_2O); two additional analytes (NO_2 and NH_3) are also included in the zero bias analysis due

to the wide interest in these hazardous gases suggested by the sensing literature;

- for all combinations of the five sensor types and six analytes (RDX, HMX, TNT, N_2, CO_2, and H_2O), the current-voltage characteristics of the sensor-analyte pairs are computed, over a bias voltage range 0.2-0.6 volts; due to the nonlinear response of the functionalized CNTs, this current data is not degenerate and therefore greatly expands the sensor output data base available for selectivity analysis;

- the performance of the five sensors as an array is analyzed using a Principal Component Analysis, to determine the ability of the array to distinguish between the various analytes.

Fig. 5.1 shows equilibrium configurations for TNT, RDX, and HMX molecules adsorbed on the four functionalized CNTs investigated in this chapter.

The first set of ab initio computational results presented here are for adsorption energy (equation 1.6) and change in conductance (equation 1.5, expressed in quantum conductance units G_o), at zero bias voltage, due to analyte adsorption. Fig. 5.2 shows the results for a baseline (pristine) CNT. In this case the conductance change data shows a low sensitivity for most analytes, and the computed data is sign consistent with reported experimental results for O_2 [116], H_2O [117], NH_3 [119], and TNT [78]. Fig. 5.3 shows the zero bias configuration results for the functionalized CNTs. Note that functionalization is often discussed as a means to increase the sensitivity and selectivity

of SWCNT sensors [43, 48]. In general, functionalization increases slightly the carbon-carbon bond lengths in the CNT wall at the point of attachment of the functional group, from 1.42Å for the pristine CNTs to approximately 1.50Å for the functionalized CNTs. This corresponds to a change in the hybridization from sp^2 to sp^3 for those carbon atoms [159]. The carbon-carbon bond lengths for carbon atoms not attached to the functional group are not significantly changed, indicating that the rehybridization is local to the functionalization. This result is similar to that observed in previous studies [160]. With regards to zero bias transmission, the functionalized nanotubes showed lower conductance than the pristine nanotube. This result is consistent with previous experimental and computational studies, which showed that covalent functionalization has an adverse impact on the electrical transport properties of metallic CNTs [161, 160, 162].

5.3.1 Hydroxyl functionalization

Functionalization of SWCNTs with OH [90] can be accomplished using ozone or acid treatments; OH functionalized CNTs are commercially available. In published experimental work OH functionalized CNTs have been used in sensing organic vapors [154] and pollutant gases, including CH_4, SO_2, NH_3 and CO [16]. As indicated in Fig. 5.3, the change in conductance due to explosive molecule sensing is opposite in sign to that produced by all of the background gases except water. The conductance change induced by RDX adsorption is very similar to that for water. Note that O_2 and NO_2 show

large negative changes in conductance, while HMX and TNT show significant positive changes. In published experiments, the response of OH functionalized carbon nanotubes to ammonia adsorption [16] is a decrease in conductance, which is sign consistent with the modeling results shown here.

5.3.2 Carboxylic acid functionalization

Functionalization of SWCNTs with COOH is also accomplished by acid or ozone treatments [90], and COOH functionalized SWCNTs are also commercially available. They have been applied to detect organic vapors [90], DMMP [163], NH_3, CH_4, H_2, SO_2, CO, and Cl_2 [48]. The change in conductance shown here for HMX sensing differs in sign from those for the other explosives. RDX and O_2 show conductance changes similar in sign and magnitude, while NH_3 shows a significantly larger magnitude response which also differs in sign. Published experiments show that CNTs functionalized with carboxylic acid [48, 16, 156] react to ammonia with a decrease in conductance, which is sign consistent with the present modeling results.

5.3.3 Oxygen functionalization

Functionalization of SWCNTs with oxygen can be accomplished by treatment with ozone followed by a photoconversion process [164]. This forms a COC bond between two neighboring carbon atoms on the CNT sidewall. In this case the computed conductance change response to explosives is opposite in sign to that for all of the background gases except water; RDX and TNT

show a similar response while that for HMX is much lower. Note that NO_2 induces a negligible conductance change in a COC functionalized CNT(5,5).

5.3.4 Amine functionalization

Functionalization of SWCNTs with NH_2 can be accomplished using a plasma activation process [165]; amine functionalized CNTs are commercially available. Here O_2 and NO_2 adsorption show conductance changes that are opposite in sign to those for the other analyte molecules. Note that RDX and H_2O show a similar conductance response, as do TNT and CO_2.

Overall, the differences in the conductance change responses suggest that, when used in a sensing array, these functionalized CNTs may offer good selectivity. To estimate the array performance, a Principal Component Analysis (PCA) was performed using the zero bias conductance data for pristine and functionalized CNT(5,5) sensors plotted in Figs. 5.2 and 5.3. A PCA of the conductance change data, performed with commercial software, indicates that (in this case) the first two principal components account for over 97% of the variance in the data. Fig. 5.4 (left side) shows the representation of the sensor data in a two dimensional principal component space, while Fig. 5.4 (right side) plots the 'separation distances' between the analytes in the two dimensional principal coordinate space.From the two plots in Fig. 5.4, it is clear that oxygen is quite isolated in principal component space and the sensing array response would easily distinguish oxygen from the other analytes.

The second series of ab initio computational results discussed in this

section describes the current-voltage characteristics of the five modeled sensors included in this study, for the six analytes TNT, RDX, HMX, H_2O, CO_2, and N_2, under bias voltages varying over the range 0.2-0.6 volts. The purpose of the next series of calculations is to evaluate the ability of the proposed sensor array to discriminate between the three explosives and to distinguish explosives from common background gases. Hence nitrogen dioxide and ammonia are not considered in this analysis, and oxygen is excluded from this analysis by virtue of its distinctive sensor array response. As previously noted, extending the ab initio analysis work performed in this chapter to the nonzero bias case provides a factor of five (for bias voltage intervals of 0.1 volts) increase in the sensor output data base, and is motivated by interest in improving the selectivity properties of the sensor array.

Current voltage characteristics (equation 3) for each of the five sensors were computed as a function of bias voltage and plotted in Fig. 5.5 (for the pristine CNT) and Fig. 5.6 for the functionalized CNTs. Like the zero bias case results, the I-V characteristics show some distinct trends. In the case of the pristine CNT(5,5) sensor (Fig. 5.5), the response to TNT differs dramatically from those of the other analytes. In the case of the hydroxyl functionalized CNT(5,5) sensor, the nitramines show the highest current response. In the case of the carboxylic acid functionalized CNT(5,5), RDX shows the largest magnitude response and the response to HMX, a similar explosive, is different in sign. The responses from the oxygen functionalized CNT(5,5) sensor are roughly an order of magnitude lower than those from the other functionalized

sensors. In the case of the amine functionalized CNT(5,5), RDX and water show a much larger magnitude response than the other analytes. As in the case of the zero bias voltage results, the variations in the current response curves suggest that the sensor array can provide selectivity.

To evaluate the performance of the sensor array, a Principal Component Analysis was performed on the current response data shown in Figs. 5.5 and 5.6. Note that the dimensions of the principal components and the distance metrics are microamps.

The cumulative variance plot indicates that only two principal components are needed to account for at least 95% of the variance in the data. Hence the two dimensional principal component space plot in Fig. 5.7 shows that all of the analytes are well separated, as quantified by the distance metric plot. For a classification threshold of 0.5μA, all of the analytes considered here are distinguishable and are shown as green (as opposed to red) squares in the Classification Chart. Since the selected classification threshold appears reasonable, based on published experimental data on chemiresistive, SWCNT gas sensors [136, 137, 82], the results suggest that functionalized metallic carbon nanotubes show excellent potential for the selective sensing of explosive molecules.

5.4 Summary

Chemiresistive sensors based on functionalized carbon nanotubes show excellent potential for application in the sensing of explosive molecules. The

analysis presented in this chapter suggests that functionalizations previously investigated for hazardous gas sensing applications may be suitable for the selective sensing of explosives, distinguishing between explosives and background gases, between nitroaromatic and nitramine explosives, and between similar nitramine explosives. The work presented here, like many experimental studies, considers only one aspect of practical sensor design, namely the basic sensing mechanism of interest, so that much additional research is needed.

Experimental work on hazardous materials is difficult, due to both safety concerns and the severe restrictions typically placed on the handling of controlled substances. Hence computational work, as a complement to experiment, is of particular importance in the sensing applications discussed in this chapter.

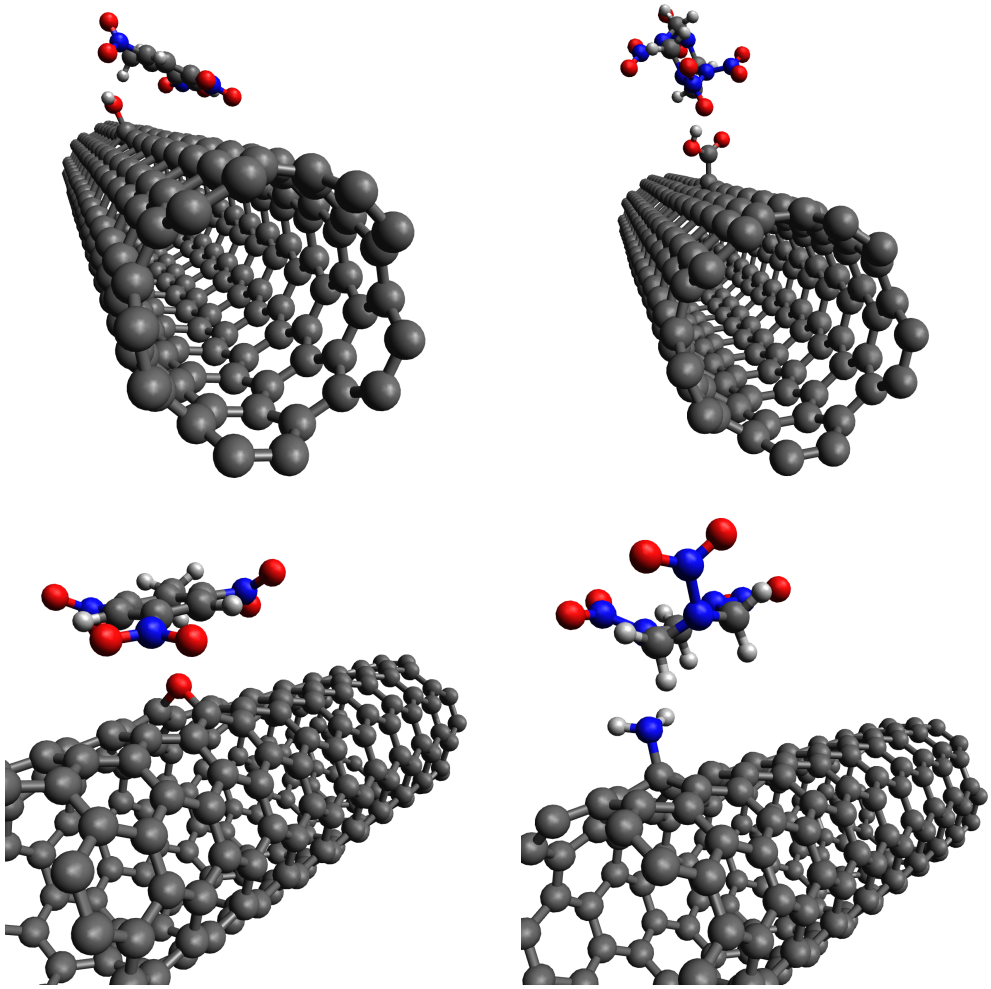

Figure 5.1: Computational models for TNT adsorption on OH functionalized CNT(5,5) (top left), HMX adsorption on COOH functionalized CNT(5,5) (top right), TNT adsorption on COC functionalized CNT(5,5) (bottom left), and RDX adsorption on NH_2 functionalized CNT(5,5) (bottom right).

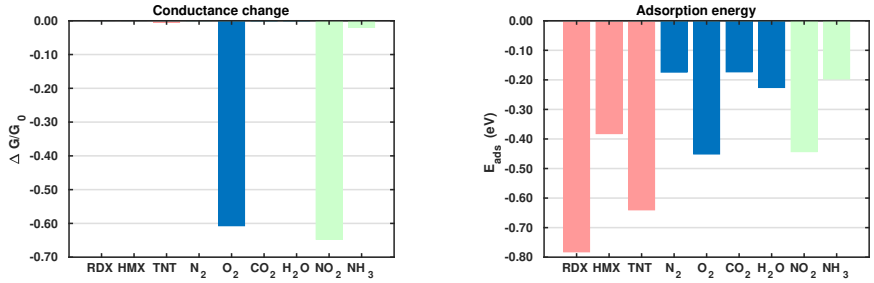

Figure 5.2: Computational results for the change in conductance (left) and adsorption energy (right) due to analyte adsorption on a pristine CNT(5,5)(top row).

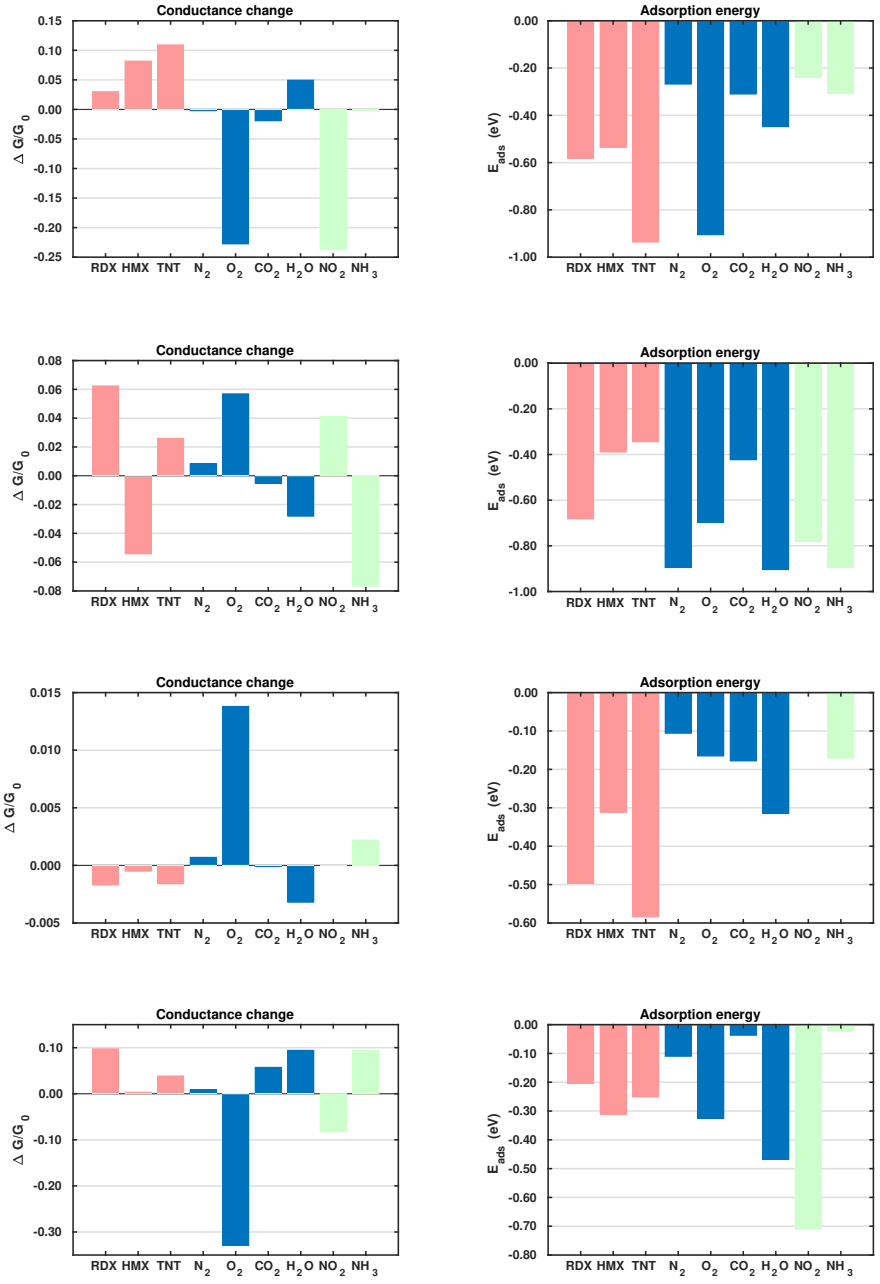

Figure 5.3: Computational results for the change in conductance (left column) and adsorption energy (right column) due to analyte adsorption on: OH functionalized CNT(5,5) (top row), COOH functionalized CNT(5,5) (second row) COC functionalized CNT(5,5) (third row), and NH_2 functionalized CNT(5,5) (bottom row).

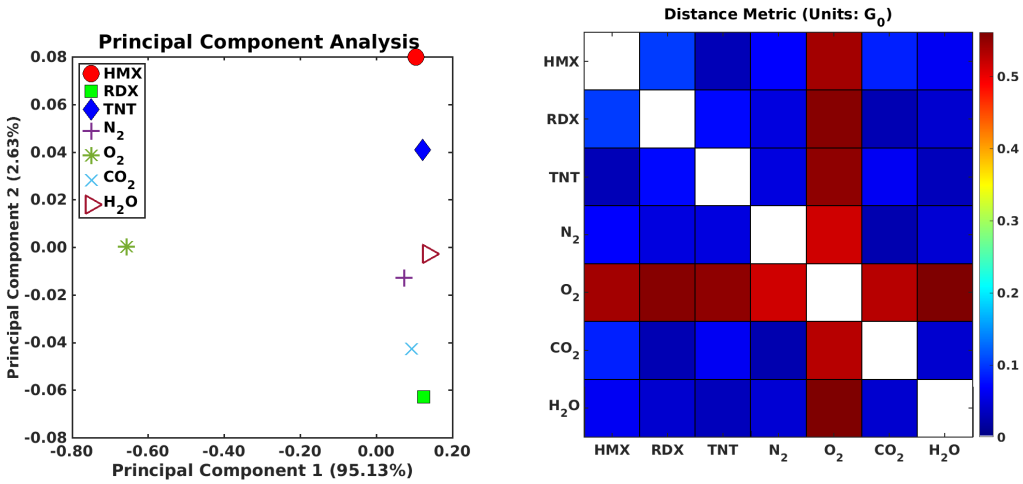

Figure 5.4: Principal Component Analysis of the zero bias voltage change in conductance due to analyte adsorption for an array of functionalized CNT(5,5) sensors: analyte locations in a two-dimensional principal component space (left), and distance metric plot (right).

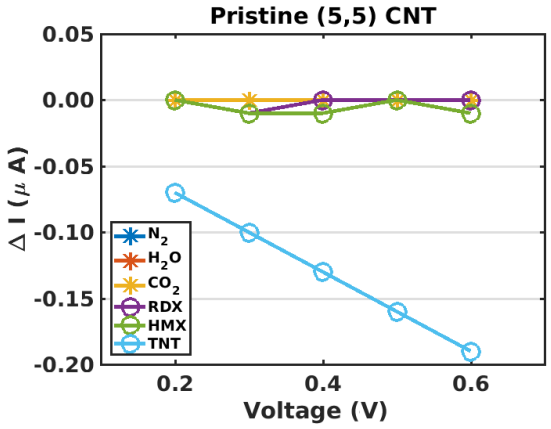

Figure 5.5: Change in current versus applied bias voltage for analyte adsorption on a pristine CNT(5,5)

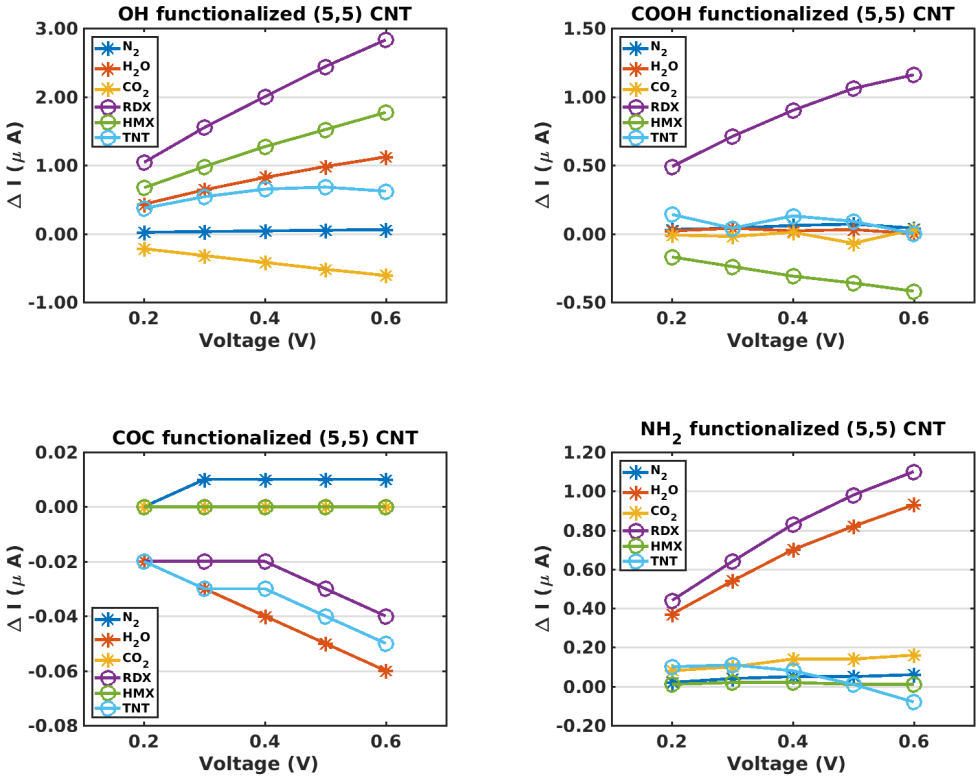

Figure 5.6: Change in current versus applied bias voltage for analyte adsorption on a functionalized CNT(5,5): OH functionalization (top left), COOH functionalization (top right), COC functionalization (bottom left), and NH_2 functionalization (bottom right).

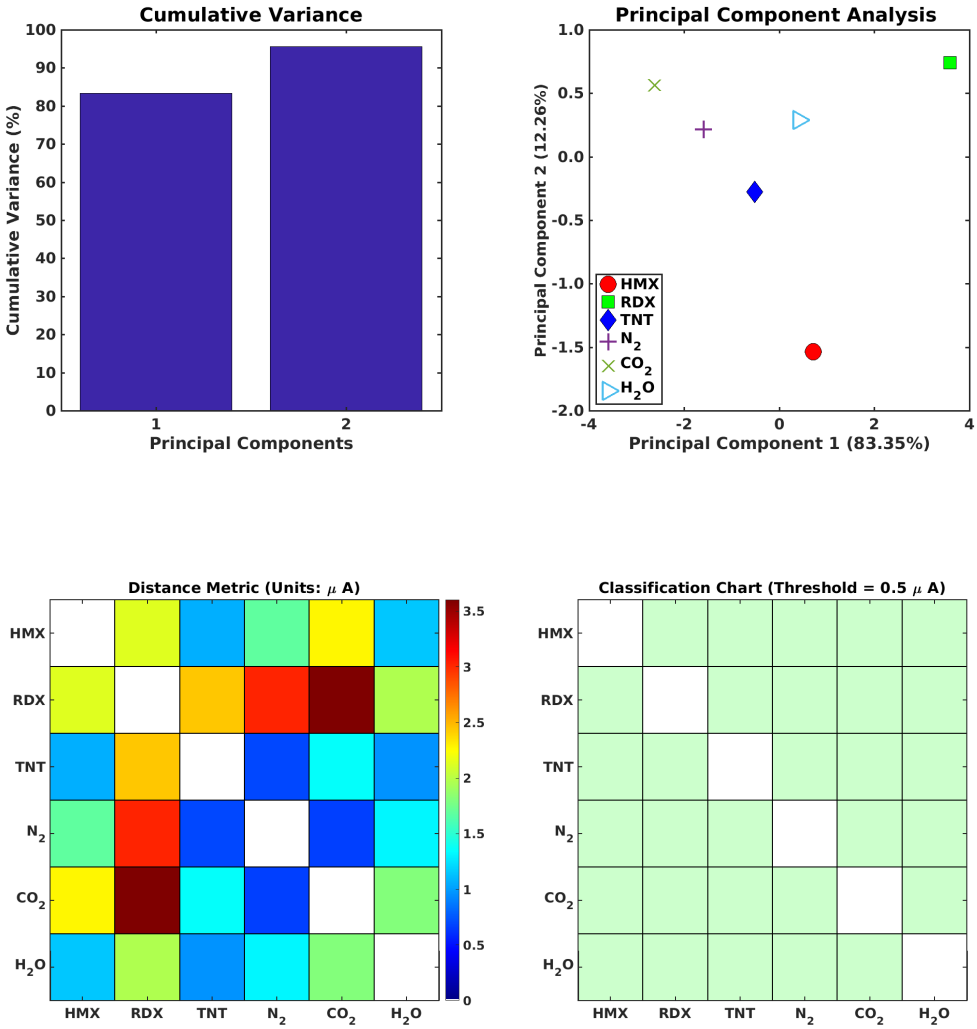

Figure 5.7: Principal Component Analysis of the change in current due to analyte adsorption for an array of functionalized CNT(5,5) sensors: Cumulative Variance plot (top left), analyte locations in a two-dimensional principal component space (top right), Distance Metrics plot (lower left), and Classification Chart (lower right, green squares indicate the ability to distinguish between analytes at the indicated classification threshold).

Chapter 6

Functionalized Semiconducting Carbon Nanotubes Arrays for Gas Phase Explosives Detection

6.1 Introduction

Single molecule detection systems are a focus of research in sensing applications which require 'ultra-sensitive' measurement [166] of transient kinetics or analyte concentrations. Examples include the directed assembly of nanostructures [140], disease detection [167], and biological process characterization [168]. As in many other sensing applications [169], carbon nanotube (CNT) based devices [166, 168] are of considerable research interest, one reason being that they may reduce the size, cost, and power requirements of current single molecule detection systems [167]. Trace detection of explosives [70] is another application where the mere presence, not necessarily the concentration, of an analyte is of concern, in this case for safety and security reasons. The very low vapor pressures [77, 74] of most explosives already places a strong emphasis on sensitivity; recognizing that many explosives share similar functional groups, the design of explosive sensors for selectivity can also be difficult.

Since carbon nanotubes have a high surface area per unit mass, they

are attractive candidates for light weight, low power gas sensors. [42] The performance of CNT based gas sensors has been studied in many experiments [170, 171, 139, 145, 146], which typically investigate chemiresistive sensing [147, 138]. Depending on their chirality, single walled carbon nanotubes (SWCNTs) can be metallic or semiconducting. Metallic CNTs can theoretically carry current densities that are much higher than copper or aluminum wiring. [172] Semiconducting nanotubes show a band gap of about 0.5 - 1.0 eV that varies inversely with the CNT diameter [137, 173]. However upon analyte adsorption some semiconducting CNTs have been shown to transition from semiconducting to metallic, a transition which is attributed to charge transfer between the CNT and the analyte and changes in the bandgap or density of states of the CNT [174, 82, 175]. Such transitions encourage the consideration of semiconducting CNTs in chemiresistive sensing applications [136].

Since pristine CNTs show limited sensitivity, the CNT surface is often modified for sensing applications. These modifications may take the form of lattice defects [90, 91] or surface functionalizations [79, 149, 150], which may be covalent or non-covalent. Carbon nanotubes with covalent surface functionalizations have shown improved sensing properties in some published experiments [154, 16, 156, 157] and some computational work [155]. The covalent functionalizations considered in this chapter are those most commonly applied to carbon nanotubes. OH functionalization can develop during CNT production [90] or be induced by post-production treatments [154]. In published experiments, gas sensors using OH functionalized SWCNTs have shown

sensitivity to organic vapors [154] and pollutant gases, including CH_4, SO_2, NH_3, and CO [16]. COOH functionalization can be produced by treating CNTs with ozone or acid [90]. In published experiments, CNTs with COOH functionalization have shown sensitivity to DMMP [163], CH_4, SO_2, CO, and Cl_2 [48]. COC functionalization has been induced [176] by ozone treatment, followed by a photoconversion process. NH_2 functionalization can be produced by dielectric barrier discharge and plasma activation processes [177].

Motivated by the cited experimental results on gas sensing with covalently modified CNTs, and the well known advantages of employing sensor arrays to improve selectivity, [17] this chapter investigates the performance of covalently functionalized semiconducting CNT arrays for trace detection of explosive gas molecules. Due to the high cost of producing pure metallic or semiconducting CNTs, most experiments have employed mixed collections of metallic and semiconducting nanotubes. Here the study of semiconducting CNTs is motivated by the expected presence of nonlinearities in the current-bias voltage response of array components to surface adsorption of an analyte. Such nonlinearities will in general improve the selectivity of the sensor array, at best producing an 'k-fold' increase in the effective size of the sensor array, where 'k' is the number of distinct bias voltages included in the sensor output data base. The semiconducting CNT considered here has chirality (7,0), and the four modeled covalent functionalizations are due to hydroxyl, carboxylic acid, oxygen, and amine groups. The analytes considered here are three explosives (HMX, RDX, TNT) and three background gases (N_2, CO_2,

H_2O). Oxygen is not modeled since the "extreme sensitivity" [82] of carbon nanotubes to oxygen will in general render it distinguishable from any other analyte in standard 'pattern matching' analysis of sensor array data [71, 17]. Two hazardous gases (NO_2 and NH_3) are also analyzed, based on the wide interest in these gases suggested by the sensing literature. Note that the list of analytes includes one nitroaromatic and two nitramine explosives, and that the two nitramines have a very similar molecular structure.

In the work which follows, ab initio methods are used to compute the response of the CNT(7,0) to functionalization followed by analyte adsorption, over a range of bias voltages. Principal Component Analysis [71, 17] is then applied to estimate the ability of the sensor array to distinguish the modeled analytes. The modeling results indicate that at a reasonable current detection threshold, the sensor array can distinguish (with one exception), all three explosives from all three background gases, both hazardous gases from all three background gases, and all three explosives from each other. This includes distinguishing between the two similar nitramines.

6.2 Computational methods

All of the calculations in this chapter model a semiconducting CNT with chirality (7,0), augmented by the functionalizations and analytes discussed in the next section. The length of the CNT in the scattering zone was 16 unit cells, with a unit cell length of 4.26Å. The total atom count for each model was 448 atoms, plus those for the functional group and the analyte. In

the transport directions, the electrodes were constructed of (7,0) carbon nanotubes, in order to model a conductor of infinite length. Starting geometries for the analytes were taken from published work [108, 109, 110], and starting orientations for the analytes were obtained by identifying the minimum energy configurations for analyte adsorption on a pristine metallic CNT(5,5).

6.3 Results and discussion

Computational analysis of the functionalized semiconducting CNT sensor array proceeds as follows:

- the five array components are semiconducting CNTs with chirality (7,0), including one pristine nanotube and four functionalized nanotubes, where the functionalizations are hydroxyl (OH), carboxylic acid (COOH), oxygen (COC), and amine (NH_2) groups;
- a band structure is computed for each of the five sensors;
- the adsorption energy is computed for all combinations of the five sensors and eight analytes (TNT, HMX, RDX, nitrogen, carbon dioxide, water, nitrogen dioxide, and ammonia);
- a current-bias voltage curve is computed for all combinations of the five sensors and eight analytes, for bias voltages over the range 0.3-0.9 volts, at intervals of 0.1 volts;

- a Principal Component Analysis (PCA) is performed on the the sensor output data, defined as the current increments of equation (1.6), in order to evaluate the performance of the sensor array in the selective identification of hazardous gases or explosive molecules.

More specifically, the last item includes three principal component analyses, one evaluating the ability of the sensor array to distinguish between six analytes (three explosives and three background gases), and two additional principal component analyses evaluating the ability of the sensor array to distinguish between four analytes (a hazardous gas, either nitrogen dioxide or ammonia, and three background gases).

Figs. 6.1, 6.2, and 6.3 show the adsorption of explosive molecules on all five of the modeled CNT sensors, and the adsorption energy for all forty sensor-analyte combinations. In the pristine CNT case: (a) TNT and NO_2 show the largest adsorption energy, and (b) the computed adsorption energy of 0.72 eV for NO_2 is similar to the adsorption energy of 0.9 eV reported by Kong et al. [136] for a semiconducting CNT(10,0). The adsorption energy results for the four functionalized nanotubes show in general high adsorption energies for nitrogen dioxide, adsorption energies for water which are higher than those of the other background gases, and adsorption energies for the explosives which are more functionalization dependent than those for the background gases.

Figs. 6.4 and 6.5 show band structures for all five sensor configurations. The pristine CNT(7,0) is semiconducting, with a computed band gap of

approximately 0.9 eV, consistent with previous theoretical and computational work [178, 179]. This band structure is changed by the introduction of covalent functional groups. Band structures for OH, COOH, and NH_2 functionalization show modified band gaps of 0.33, 0.44, and 0.37 eV respectively, and the introduction of a new band near the Fermi energy, consistent with previous computational studies [160, 162]. In the case of COC functionalization, the band gap is reduced to 0.59 eV, however a new band near the Fermi energy is not produced.

Figs. 6.4 and 6.6 show the computed current-voltage characteristics for the five modeled sensors, for adsorption of the three explosives and the three background gases, as a function of the applied bias voltage over the range 0.3-0.9 volts. These curves are the sensor array output data that will be used in the PCA to identify the adsorbed analytes. In the pristine sensor case, the current-voltage characteristics in Fig. 6.4 show similar shapes for the three explosives. The changes in the current are positive for all of the analytes, consistent with experiments which have shown that: (a) the conductance of a CNT sensor increases in the presence of N_2 gas [180], (b) the conductance of a CNT mat increases when distilled water is injected [181], (c) the conductance of a semiconducting CNT network increases due to water adsorption [117], and (d) the conductance of a semiconducting CNT increases when NO_2 is adsorbed [136, 119]. Several features of the current response curves suggest that the array response will show selectivity. In the hydroxyl functionalization case, the current change for HMX differs in sign from the current changes due to

RDX and TNT. In the carboxylic acid functionalization case, the nitroaromatic explosive (TNT) shows a positive change in current while the nitramines (HMX and RDX) show a negative change in current. In the oxygen functionalization case, all of the analytes show current change curves with a similar shape, but they differ in magnitude. In the amine functionalization case, most of the current response curves are non-monotonic. As noted in the introduction, the sensor array responses to nitrogen dioxide and ammonia adsorption were also computed, to evaluate the array performance in sensing those hazardous gases. Fig. 6.7 shows the current response data for those two analytes. The NO_2 data shows a strong dependence on sensor type, and the magnitude of the current change is much higher than that for the other analytes. The NH_3 data shows a smaller output current range but a strong dependence on bias voltage. Overall, the computed sensor outputs suggest a selective array response to the analytes.

To evaluate the performance of the functionalized, semiconducting CNT array as an explosive or hazardous gas sensor, Principal Component Analysis [12, 13, 14, 15, 1] was performed on three different data sets extracted from Figs. 6.4, 6.6, and 6.7. The first data set considers the three explosives and the three background gases, the second data set considers NO_2 and the three background gases, and the third data set considers NH_3 and the three background gases.

The sensor output data, principal components, and distance metrics in this chapter are expressed in units of microamps. Based on published ex-

perimental data [136, 137, 82] on gas sensing using carbon nanotubes, the classification threshold used here to estimate whether or not two analytes will be distinguishable is 0.5 μA.

Fig. 6.8 shows the PCA results for explosives sensing. The cumulative variance plot (top left) indicates that three principal components are required to account for at least 95% of the variance in the data. The analyte separations in a two principal coordinate space are illustrated in the top right figure. The distance metric (bottom left) shows the separation distances for the analytes in a three dimensional principal component space. For a classification threshold of 0.5 μA, the classification chart (bottom right) indicates that all of the analyte pairs, with the exception of RDX and water, can be distinguished from each other.

Fig. 6.9 shows the PCA results for nitrogen dioxide sensing. The cumulative variance plot (top left) indicates that two principal components can account for more than 95% of the variance in the data. The analyte separations in a two dimensional principal coordinate space are illustrated in the top right figure. The distance metric (bottom left) shows the separation distances for the analytes in a two dimensional principal component space. For a classification threshold of 0.5 μA, the classification chart (bottom right) indicates that all of the analyte pairs can be distinguished from each other.

Fig. 6.10 shows the PCA results for ammonia sensing. The cumulative variance plot (top left) indicates that three principal components are required to account for at least 95% of the variance in the data. The analyte separations

in a two dimensional principal coordinate space are illustrated in the top right figure. The distance metric (bottom left) shows the separation distances for the analytes in a three dimensional principal component space. For a classification threshold of 0.5 μA, the classification chart (bottom right) indicates that all of the analyte pairs can be distinguished from each other.

Overall the analysis results suggest that functionalized semiconducting CNT arrays may be effectively applied to distinguish explosive or hazardous gas molecules from common background gases.

6.4 Summary

Experimental research on the trace detection of explosives is complicated by safety concerns and the severe restrictions typically placed on the handling of explosive materials. Computational research, as a complement to experiment, therefore offers important opportunities to accelerate the development of new explosive sensing concepts. The ab initio conductance and sensor array performance modeling presented in this chapter suggest that functionalized semiconducting carbon nanotubes show excellent potential for application in the development of light weight, low power explosives sensors. Although molecular scale discrimination among a range of analytes is only one aspect of the general sensor design problem, it is of particular importance in explosives sensing and other applications where ultra-sensitive detection methods are needed.

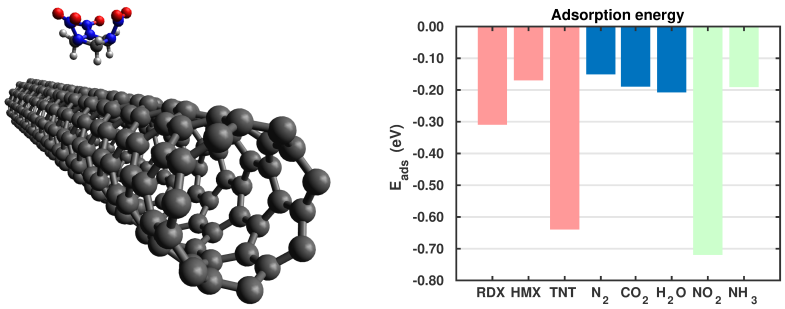

Figure 6.1: Adsorption of an RDX molecule (left) and adsorption energy as a function of the analyte (right) for a pristine (7,0) CNT.

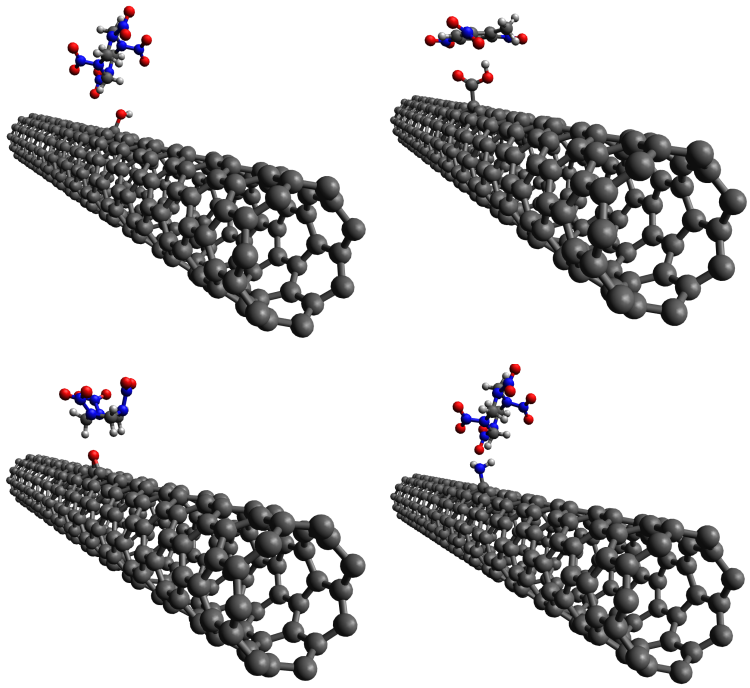

Figure 6.2: Computational models of: HMX adsorption on an OH functionalized CNT (top left), TNT adsorption on a COOH functionalized CNT (top right), RDX adsorption on a COC functionalized CNT (bottom left), and HMX adsorption on an NH_2 functionalized CNT (bottom right).

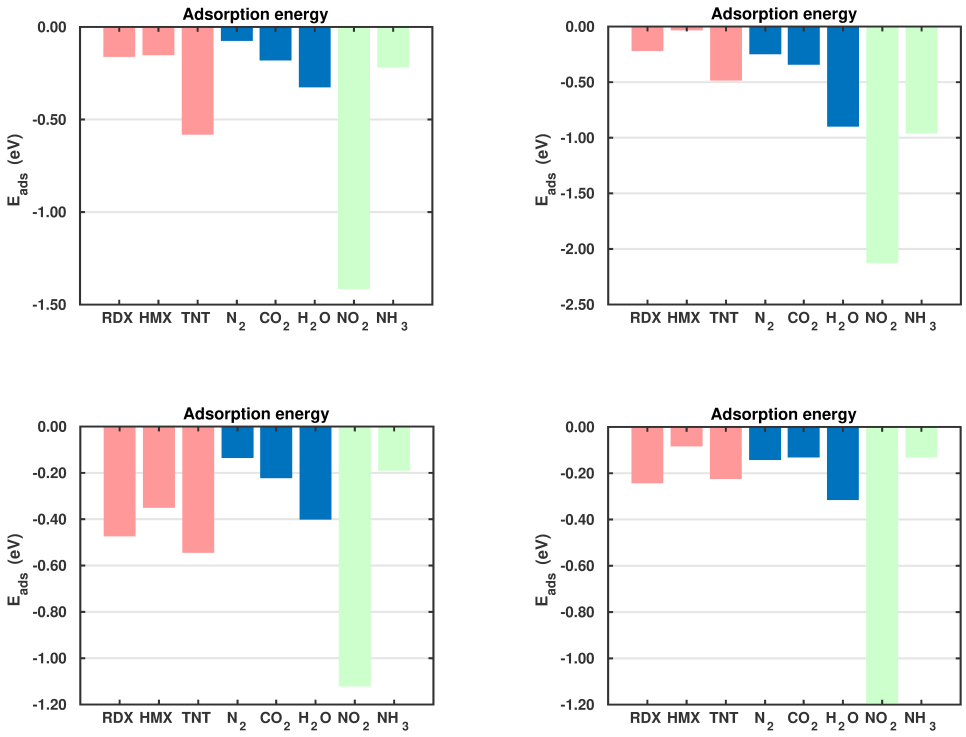

Figure 6.3: Adsorption energy as a function of the analyte for: an OH functionalized CNT (top left), a COOH functionalized CNT (top right), a COC functionalized CNT (bottom left), and an NH_2 functionalized CNT (bottom right).

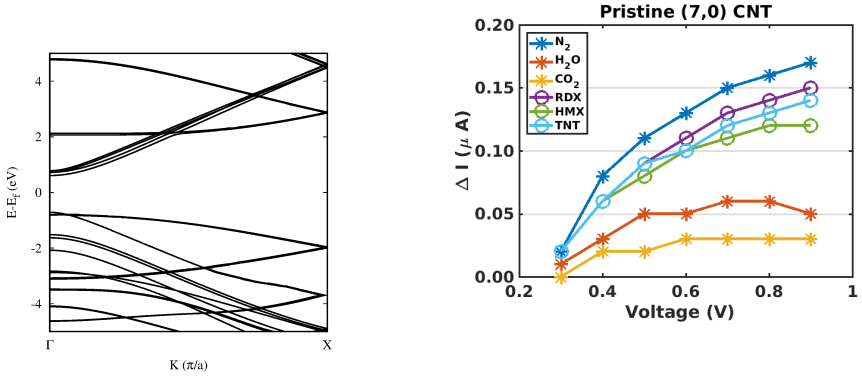

Figure 6.4: Band structure (left) and incremental current-bias voltage characteristics (right) for a pristine (7,0) CNT.

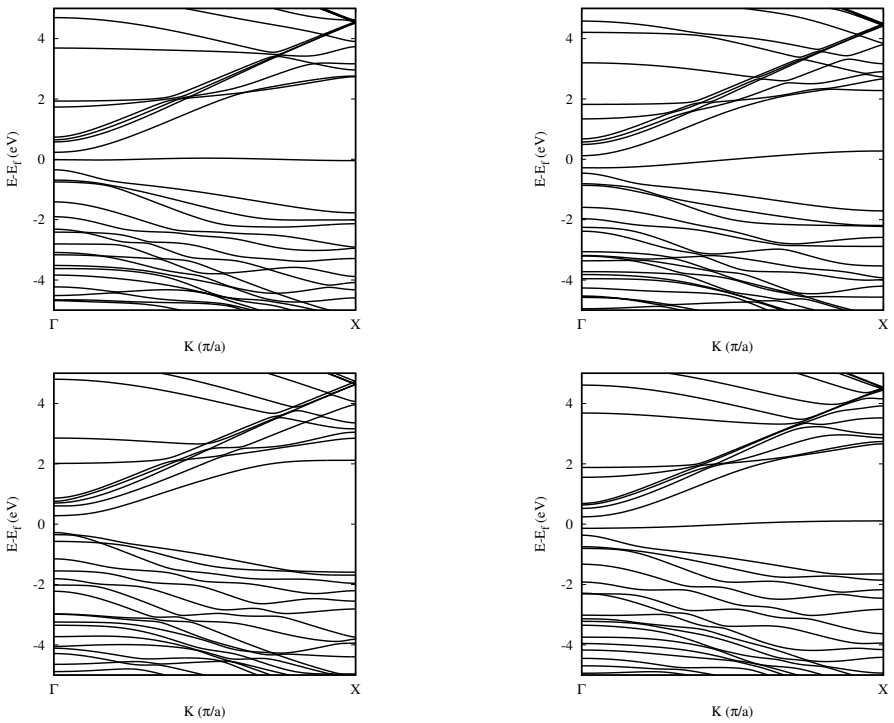

Figure 6.5: Band structures for functionalized (7,0) CNTs: OH functionalization (top left), COOH functionalization (top right), COC functionalization (bottom left), and NH_2 functionalization (bottom right).

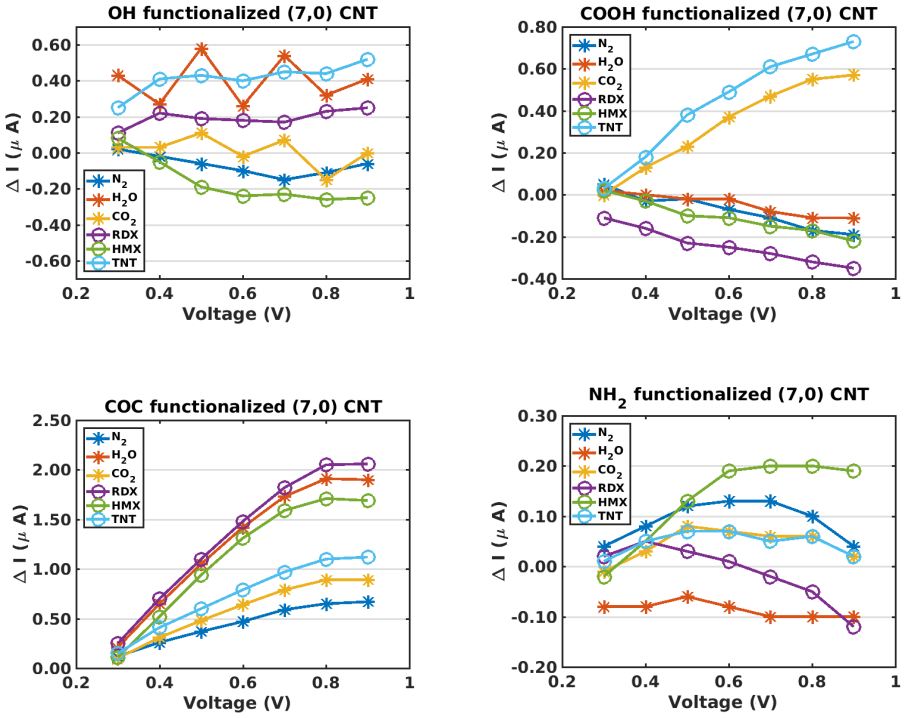

Figure 6.6: Incremental current-bias voltage characteristics for functionalized (7,0) CNTs: OH functionalization (top left), COOH functionalization (top right), COC functionalization (bottom left), and NH_2 functionalization (bottom right)

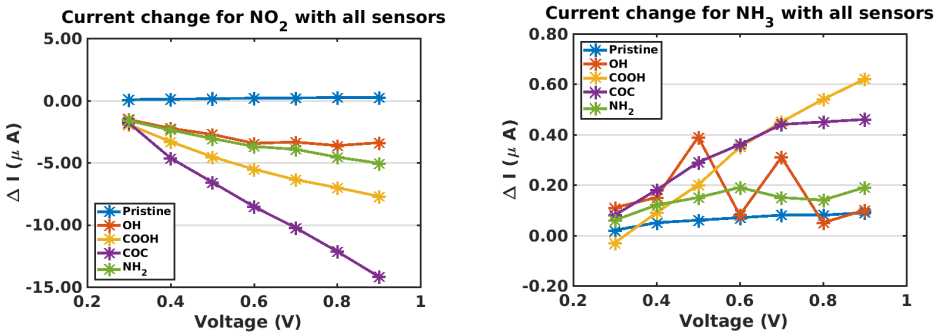

Figure 6.7: Incremental current-bias voltage characteristics for NO_2 adsorption (left) and NH_3 adsorption (right) on pristine and functionalized (7,0) CNTs.

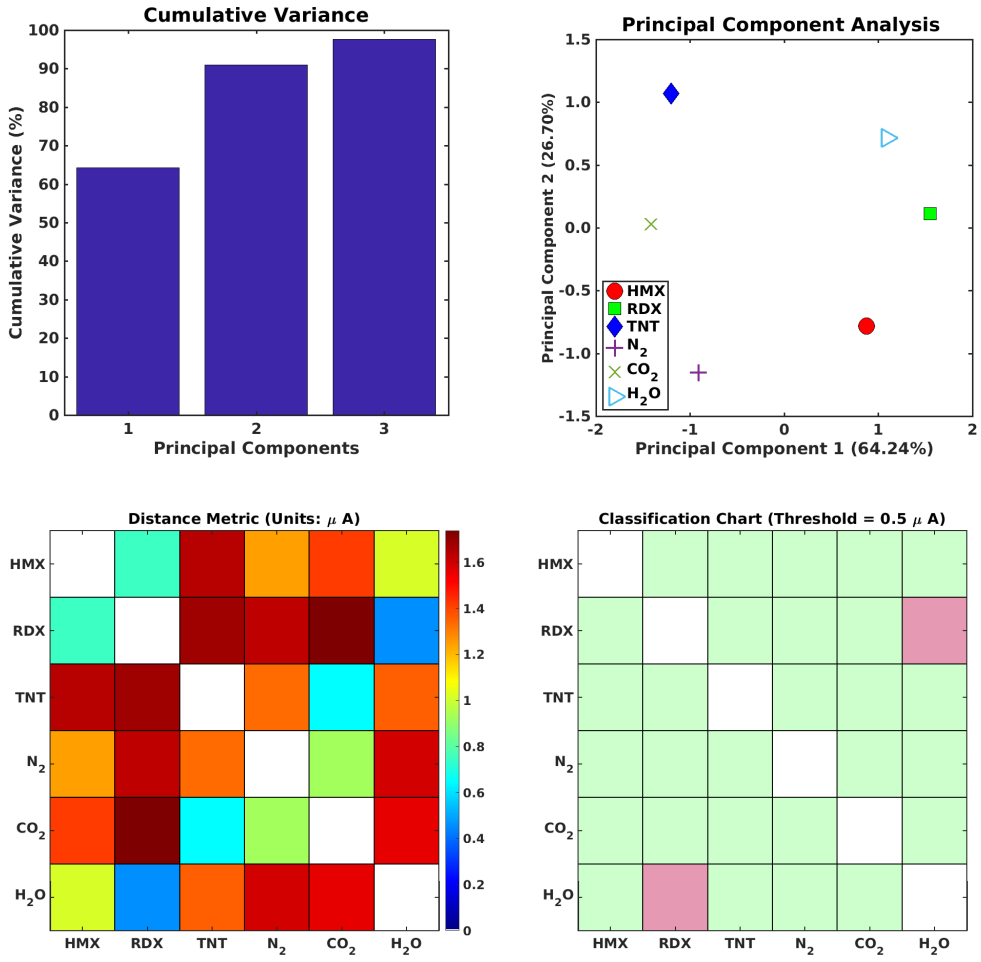

Figure 6.8: Principal Component Analysis for explosive sensing using an array of functionalized CNT(7,0) sensors: cumulative variance plot (top left), analyte locations in a two-dimensional principal component space (top right), distance metrics plot (lower left), and classification chart (lower right). Note that green (red) squares indicate the ability (inability) to distinguish between analyte pairs at the specified classification threshold.

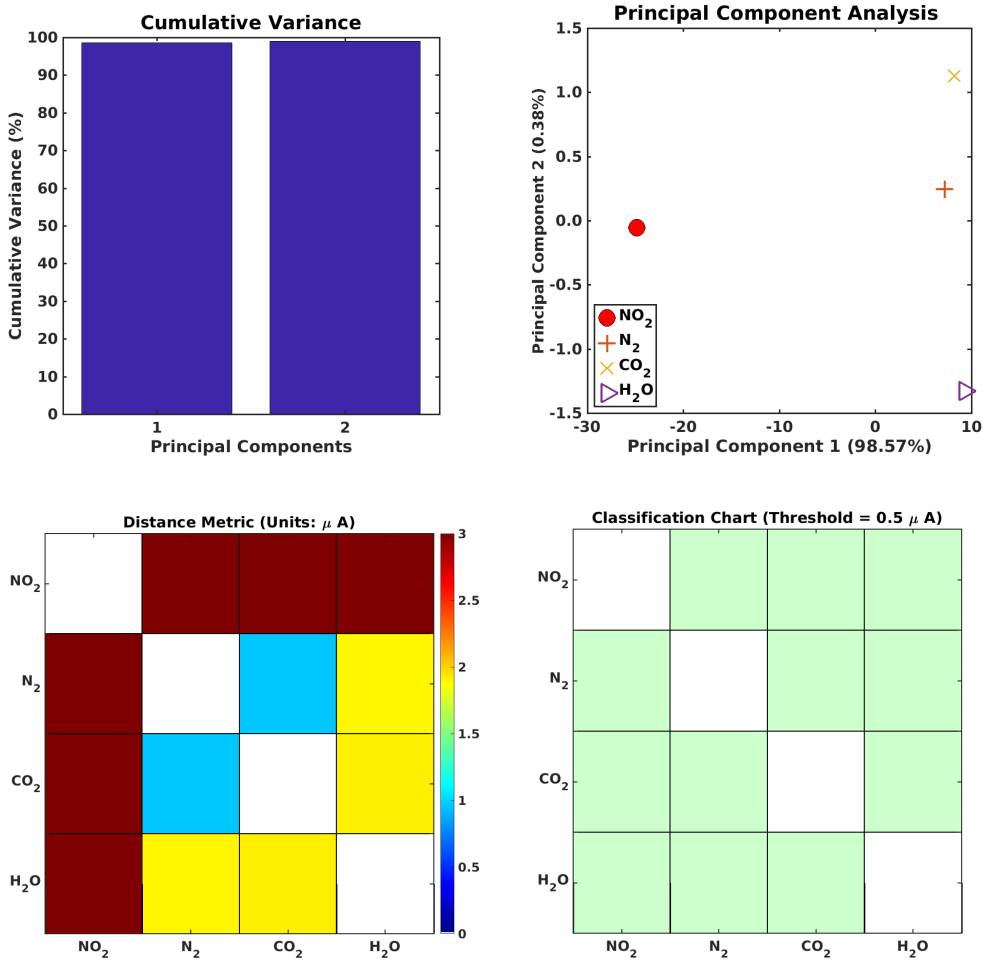

Figure 6.9: Principal Component Analysis for nitrogen dioxide sensing using an array of functionalized CNT(7,0) sensors: cumulative variance plot (top left), analyte locations in a two-dimensional principal component space (top right), distance metrics plot (lower left), and classification chart (lower right). Note that green (red) squares indicate the ability (inability) to distinguish between analyte pairs at the specified classification threshold.

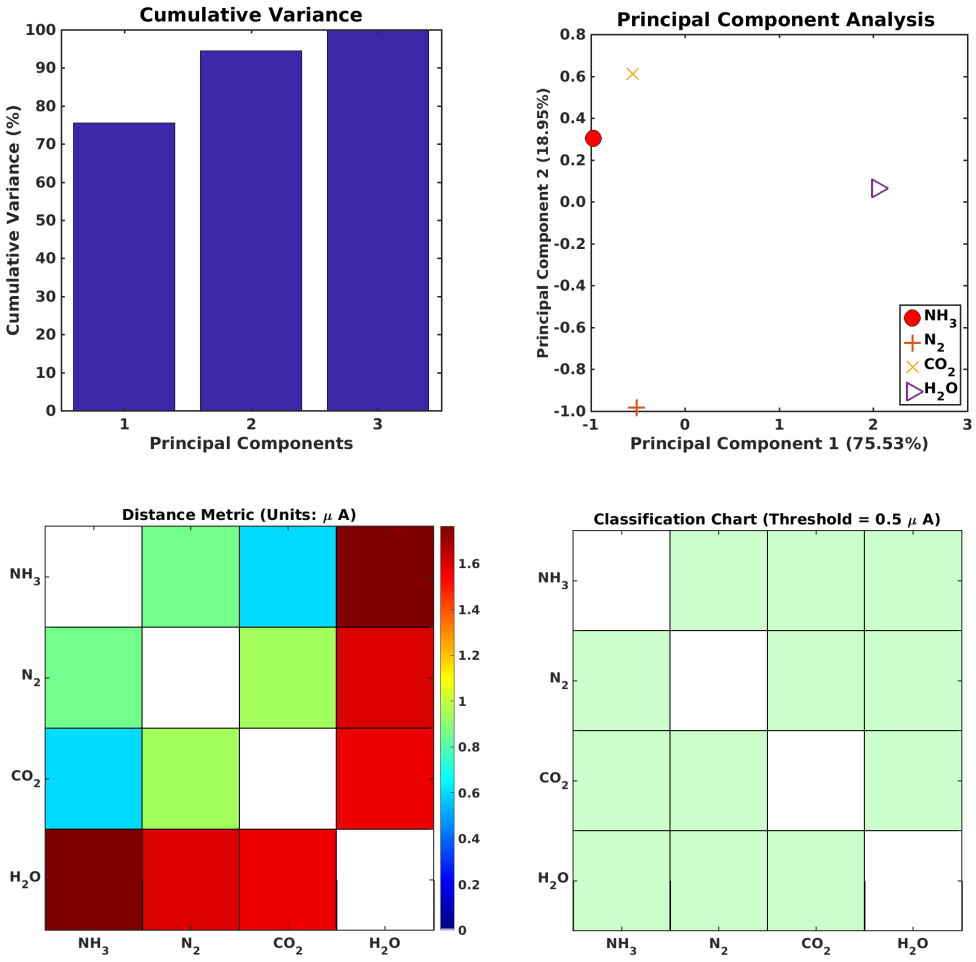

Figure 6.10: Principal Component Analysis for ammonia sensing using an array of functionalized CNT(7,0) sensors: cumulative variance plot (top left), analyte locations in a two-dimensional principal component space (top right), distance metrics plot (lower left), and classification chart (lower right). Note that green (red) squares indicate the ability (inability) to distinguish between analyte pairs at the specified classification threshold.

Chapter 7

Spin Polarized Ab Initio Molecular Dynamics

7.1 Introduction

Electrons can travel inside CNTs without changing their spin orientation for hundreds of nanometers [111], however spin polarization has been observed for certain chiral CNTs with small armchair edges [182]. Spin dependent transport is also important for interfaces between CNTs and ferromagnetic materials, such as CNTs connected to metal electrodes [111] or CNTs doped with transition metals [183]. In CNT based sensor applications, spin-polarization is relevant when CNTs are decorated with clusters of metals such as Nickel. Note that Ni-decorated CNTs are used as carbon monoxide sensors [184]. In addition, spin polarization is important in modeling other carbon based sensors, such as graphene nanoribbons.

This chapter develops a new ab initio molecular dynamics (AIMD) model of spin polarized systems, including electric and magnetic filed loading. Such models may be employed to simulate the finite temperature response of carbon nanotube based sensors. Although this dissertation includes only a theoretical formulation, it is expected that future work will include numerical implementation.

The model of spin-polarized sensor dynamics developed here employs a novel nonholonomic Hamiltonian modeling methodology. The formulation couples a quantum model of the electronic structure to a molecular model of the nuclear dynamics, and quantifies the modeled nanoscale system's interaction with the external thermal and electromagnetic environment. The model developed in this chapter can complement experimental research in this field, supporting research linking material and defect physics to measured experimental performance.

7.2 Motivation

A very general motivation for the modeling research described here is provided by the field of quantum sensors. Quantum sensors offer important opportunities in the development of sensitive, high resolution detection and measurement systems [185]. Potential applications include thermal, optical, magnetic, inertial, and other sensing devices [186]. Although atomic sensors employing vapor cells or optical and magnetic confinement have demonstrated exceptional performance [187], solid state devices [188] are of great interest, and may facilitate fundamental improvements in miniaturized, low cost, low power sensors. Solid state devices based on nitrogen-vacancy (NV) defects in diamond [189, 190] have been the focus of much experimental and theoretical research, for potential application in both quantum sensing [191] and quantum computing [192] systems. Nitrogen-vacancy defect based sensors in diamond have demonstrated excellent sensitivity in nanoscale measurements

of both magnetic [193] and electric [194] fields; however experiments have also demonstrated a significant temperature [195] and strain field [196] response. The sensitivity of NV magnetometers is remarkable, however experimental work aimed at improving their performance has demonstrated that fundamental advances in sensor technology will require a concerted effort to understand complex energy domain coupling effects on quantum sensing physics. Computational model development can contribute to that effort.

7.3 Previous work

Computational research is increasingly seen as a valuable adjunct to experiment, assisting in the development of new materials and processes, using models applied at both the molecular and electronic scales. Reacting molecular dynamics models offer a computationally efficient approach to the materials design problem, but generally rely on empirical force fields. Ab initio molecular dynamics models, by contrast, offer the possibility of investigating the physics of interest at a fundamental level. Although uncoupled simulations conducted at the electronic and molecular scales have proven to be of considerable value in scientific research and engineering design, the transient multiphyics of central interest in many sensing applications will require a multiscale, multiphysics modeling approach.

Although a variety of ab initio [197], molecular dynamics [198], and ab initio molecular dynamics [199, 200] methods are currently available for application to materials and process design problems, fundamental improvements

in current numerical methods are needed to support research on improved sensors. The generic form of the numerical formulation developed in this research means that the method can be applied in future research to a variety of materials design applications.

7.4 Numerical model

The discussion which follows outlines the development of a new ab initio molecular dynamics formulation, coupled to macroscale thermal and magnetic loads, using the proposed nonholonomic Hamiltonian methodology. The modeled system is a collection of n nuclei and n_e electrons in an NVT ensemble. The Hamiltonian for the system (H) is the sum of the kinetic (T_n) and potential (V_n) energies for the nuclei (which take a molecular dynamics form) and a total energy (E_e) for the electrons (which takes a quantum mechanics form)

$$H = T_n + V_n + E_e \tag{7.1}$$

The nuclear kinetic co-energy, nuclear momenta ($\mathbf{p}^{(i)}$), and nuclear potential energy are

$$T_n^* = \frac{1}{2} \sum_{i=1}^{n} M^{(i)} \dot{\mathbf{q}}^{(i)2} \,, \qquad \mathbf{p}^{(i)} = \frac{\partial T_n^*}{\partial \dot{\mathbf{q}}^{(i)}} \,, \qquad V_n = V_n(\mathbf{q}) \tag{7.2}$$

where $M^{(i)}$ is a nuclear mass and $\mathbf{q}^{(i)}$ is a nuclear center of mass position. The nuclear potential energy models electrostatic repulsion of the nuclei. The quantum mechanics expression for the electronic energy includes electron repulsion, electron-nuclear attraction, electron kinetic energy, and an imposed

magnetic field, and is computed from the electronic wave function using the expectation value expression (in Dirac bracket notation)

$$E_e = \frac{<\mathbf{\Psi}|\mathbf{H}_e|\mathbf{\Psi}>}{<\mathbf{\Psi}|\mathbf{\Psi}>}, \quad \mathbf{H}_e = e\phi(\mathbf{x})\,\mathbf{I} + \sum_{j=1}^{n_s} \frac{1}{2m^{(j)}} \left[\boldsymbol{\sigma} \cdot \left(i\hbar\nabla^{(j)} + e\mathbf{A}(\mathbf{x})\right)\right]^2 \tag{7.3}$$

$$\boldsymbol{\sigma} \equiv (\sigma_1, \sigma_2, \sigma_3), \quad \mathbf{I} = \begin{pmatrix} 1 & 0 \\ 0 & 1 \end{pmatrix} \tag{7.4}$$

$$\sigma_1 = \begin{pmatrix} 0 & 1 \\ 1 & 0 \end{pmatrix}, \quad \sigma_2 = \begin{pmatrix} 0 & -i \\ i & 0 \end{pmatrix}, \quad \sigma_3 = \begin{pmatrix} 1 & 0 \\ 0 & -1 \end{pmatrix} \tag{7.5}$$

and for any vector (first order tensor) $\mathbf{v}$

$$\boldsymbol{\sigma} \cdot \mathbf{v} \equiv \sigma_1 v_1 + \sigma_2 v_2 + \sigma_3 v_3 \tag{7.6}$$

where $\mathbf{H}_e$ is the electronic Hamiltonian operator matrix, ϕ is the electric scalar potential, $\mathbf{I}$ is an identity matrix, $\boldsymbol{\sigma}$ is a vector of Pauli matrices, $\hbar$ is the reduced Planck constant, m is an electron mass, e is an electron charge, $\mathbf{A}(\mathbf{x})$ is a magnetic vector potential, and $\mathbf{\Psi} = [\Psi^+ \Psi^-]^T$ is a vector (spin up and spin down) of electronic wave functions. Interpolating the electronic wave function with basis functions ϕ_j

$$\Psi^+ = \sum_{j=1}^{n_s} a^{(j)}\,\phi_j(\mathbf{q}, \mathbf{x}), \qquad \Psi^- = \sum_{j=1}^{n_s} b^{(j)}\,\phi_j(\mathbf{q}, \mathbf{x}) \tag{7.7}$$

defines the discrete stored energy function $E_e = E_e(\mathbf{q}, \mathbf{a}, \bar{\mathbf{a}}, \mathbf{b}, \bar{\mathbf{b}})$, where $\mathbf{a}$ and $\mathbf{b}$ are vectors of time dependent basis set weighting coefficients and ' $^-$ ' denotes the complex conjugate. In order to complete the formulation, evolution equations for the time dependent basis coefficients are now introduced. These may be obtained from the Pauli equation

$$i\hbar \frac{\partial \mathbf{\Psi}}{\partial t} = \mathbf{H}_e \mathbf{\Psi}, \qquad \mathbf{H}_e = \begin{pmatrix} H_e^{aa} & H_e^{ab} \\ H_e^{ba} & H_e^{bb} \end{pmatrix} \tag{7.8}$$

Multiplying the Pauli equation by the complex conjugate basis function $\overline{\phi}_k$ and integrating over the modeled volume provides the discrete evolution equations

$$\mathbf{C}^a \, \dot{\mathbf{a}} = -\mathbf{D}^a \dot{\mathbf{q}} + \mathbf{Q}^{aa} \mathbf{a} + \mathbf{Q}^{ab} \mathbf{b}, \quad \mathbf{C}^b \, \dot{\mathbf{b}} = -\mathbf{D}^b \dot{\mathbf{q}} + \mathbf{Q}^{ba} \mathbf{a} + \mathbf{Q}^{bb} \mathbf{b} \tag{7.9}$$

$$\overline{\mathbf{C}}^a \, \dot{\bar{\mathbf{a}}} = -\overline{\mathbf{D}}^a \dot{\mathbf{q}} + \overline{\mathbf{Q}}^{aa} \, \bar{\mathbf{a}} + \overline{\mathbf{Q}}^{ab} \, \bar{\mathbf{b}}, \quad \overline{\mathbf{C}}^b \, \dot{\bar{\mathbf{b}}} = -\overline{\mathbf{D}}^b \dot{\mathbf{q}} + \overline{\mathbf{Q}}^{ba} \, \bar{\mathbf{a}} + \overline{\mathbf{Q}}^{bb} \, \bar{\mathbf{b}} \tag{7.10}$$

where the matrix coefficients are

$$C_{kj}^a = i\hbar \int \overline{\phi}_k \phi_j \, d\mathbf{x}, \quad D_{kj}^a = i\hbar \sum_{l=1}^{n_s} a^{(l)} \int \overline{\phi}_k \frac{\partial \phi_l}{\partial q^{(j)}} \, d\mathbf{x} \tag{7.11}$$

$$Q_{kj}^{aa} = \int \overline{\phi}_k H_e^{aa} \phi_j \, d\mathbf{x}, \quad Q_{kj}^{ab} = \int \overline{\phi}_k H_e^{ab} \phi_j \, d\mathbf{x} \tag{7.12}$$

$$C^b_{kj} = i\hbar \int \overline{\phi}_k \phi_j \, d\mathbf{x}, \quad D^b_{kj} = i\hbar \sum_{l=1}^{n_s} b^{(l)} \int \overline{\phi}_k \frac{\partial \phi_l}{\partial q^{(j)}} \, d\mathbf{x} \tag{7.13}$$

$$Q^{ba}_{kj} = \int \overline{\phi}_k H^{ba}_e \phi_j \, d\mathbf{x}, \quad Q^{bb}_{kj} = \int \overline{\phi}_k H^{bb}_e \phi_j \, d\mathbf{x} \tag{7.14}$$

In previous work, the momentum balance relations for the nuclei have been related to the wave equations by adopting a constant energy assumption for the system, or invoking Hellman-Feynman theorems [201]. Such assumptions may be unacceptable in cases where thermal and electromagnetic interaction with the environment is of central interest. Instead, in the discussion which follows the classical and quantum system dynamics are coupled using a nonholonomic modeling approach.

The canonical Hamilton's equations for the mixed classical-quantum system are

$$\dot{\mathbf{p}} = -\frac{\partial H}{\partial \mathbf{q}} + \mathbf{f}^q, \qquad \dot{\mathbf{q}} = \mathbf{M}^{-1}\mathbf{p}, \tag{7.15}$$

$$\mathbf{0} = -\frac{\partial H}{\partial \mathbf{a}} + \mathbf{f}^a, \quad \mathbf{0} = -\frac{\partial H}{\partial \overline{\mathbf{a}}} + \mathbf{f}^{\overline{a}}, \quad \mathbf{0} = -\frac{\partial H}{\partial \mathbf{b}} + \mathbf{f}^b, \quad \mathbf{0} = -\frac{\partial H}{\partial \overline{\mathbf{b}}} + \mathbf{f}^{\overline{b}} \tag{7.16}$$

where the inertia matrix $\mathbf{M}$ is diagonal, and $\mathbf{f}^q$, $\mathbf{f}^a$, $\mathbf{f}^b$,$\mathbf{f}^{\overline{a}}$, $\mathbf{f}^{\overline{b}}$ are generalized forces due to the nonholonomic constraints and the power input to the system. The last four Hamilton's equations, which are degenerate momentum equations (degenerate since there are no generalized momenta associated with

the generalized coordinates $\mathbf{a}$, $\overline{\mathbf{a}}$, $\mathbf{b}$, and $\overline{\mathbf{b}}$, have been overlooked in previous nanoscale simulation work (with the exception of recent work [202]). However they are of central importance, since they allow the Lagrange multipliers associated with the nonholonomic constraints to be determined in closed form.

The power input (P) to the system is due to external mechanical forces $\mathbf{F}^{(j)}(t)$, the imposed magnetic field $\mathbf{B}$, and the imposed electric field $\mathbf{E}$, and takes the form

$$P = \sum_{j=1}^{n} \left(\mathbf{F}^{(j)}(t) + \mathbf{F}_L^{(j)} + eZ^{(j)}\, \mathbf{E} \right) \cdot \mathbf{v}^{(j)}, \qquad \mathbf{F}_L^{(j)} = eZ^{(j)}\, \mathbf{v}^{(j)} \times \mathbf{B} \tag{7.17}$$

which has the general form

$$P = \mathbf{F}^{extT} \dot{\mathbf{q}} \tag{7.18}$$

The nonholonomic constraints are the discrete Pauli equations and a rate relation which quantifies thermal interaction with the environment

$$\theta \dot{S} = R\left(\theta - \theta_e\right), \qquad \theta = \sum_{j=1}^{n} \frac{1}{2nk_B}\, M_j\, \mathbf{q}^{(j)2} \tag{7.19}$$

where $\dot{S}$ is a net entropy flow from the nanoscale ensemble to the environment, θ_e is a controlled environmental temperature (and may vary with time), R is an overall heat transfer coefficient, θ is the ensemble temperature, and k_B is Boltzmann's constant. Introducing vectors of Lagrange multipliers $\boldsymbol{\lambda}^a$, $\boldsymbol{\lambda}^b$, $\boldsymbol{\lambda}^{\overline{a}}$, $\boldsymbol{\lambda}^{\overline{b}}$ for the discrete Pauli equations, the quantum constraints and the thermal dissipation expression require

$$\mathbf{f}^a = \mathbf{C}^{aT}\boldsymbol{\lambda}^a, \quad \mathbf{f}^b = \mathbf{C}^{bT}\boldsymbol{\lambda}^b, \quad \mathbf{f}^{\overline{a}} = \overline{\mathbf{C}}^{aT}\boldsymbol{\lambda}^{\overline{a}}, \quad \mathbf{f}^{\overline{b}} = \overline{\mathbf{C}}^{bT}\boldsymbol{\lambda}^{\overline{b}} \tag{7.20}$$

$$\mathbf{f}^q = \mathbf{D}^{aT}\boldsymbol{\lambda}^a + \mathbf{D}^{bT}\boldsymbol{\lambda}^b + \overline{\mathbf{D}}^{aT}\boldsymbol{\lambda}^{\overline{a}} + \overline{\mathbf{D}}^{bT}\boldsymbol{\lambda}^{\overline{b}} + \mathbf{F}^{ext} - \frac{R}{2nk_B}\left(1 - \frac{\theta_e}{\theta}\right)\mathbf{p} \tag{7.21}$$

Since equations 16 and 18 require

$$\boldsymbol{\lambda}^a = \mathbf{C}^{a-T}\frac{\partial H}{\partial \mathbf{a}}, \quad \boldsymbol{\lambda}^b = \mathbf{C}^{b-T}\frac{\partial H}{\partial \mathbf{b}}, \quad \boldsymbol{\lambda}^{\overline{a}} = \overline{\mathbf{C}}^{a-T}\frac{\partial H}{\partial \overline{\mathbf{a}}}, \quad \boldsymbol{\lambda}^{\overline{b}} = \overline{\mathbf{C}}^{b-T}\frac{\partial H}{\partial \overline{\mathbf{b}}} \tag{7.22}$$

it follows that the final Hamilton's equations for the NVT ensemble are

$$\begin{aligned}\dot{\mathbf{p}} = &-\frac{\partial H}{\partial \mathbf{q}} + \mathbf{D}^{aT}\mathbf{C}^{a-T}\frac{\partial H}{\partial \mathbf{a}} + \mathbf{D}^{bT}\mathbf{C}^{b-T}\frac{\partial H}{\partial \mathbf{b}} + \overline{\mathbf{D}}^{aT}\overline{\mathbf{C}}^{a-T}\frac{\partial H}{\partial \overline{\mathbf{a}}} + \\ &\overline{\mathbf{D}}^{bT}\overline{\mathbf{C}}^{b-T}\frac{\partial H}{\partial \overline{\mathbf{b}}} + \mathbf{F}^{ext} - \frac{R}{2nk_B}\left(1 - \frac{\theta_e}{\theta}\right)\mathbf{p}\end{aligned} \tag{7.23}$$

$$\dot{\mathbf{q}} = \mathbf{M}^{-1}\mathbf{p} \tag{7.24}$$

augmented by the discrete Pauli equations

$$\mathbf{C}^a\dot{\mathbf{a}} = -\mathbf{D}^a\mathbf{M}^{-1}\mathbf{p} + \mathbf{Q}^{aa}\mathbf{a} + \mathbf{Q}^{ab}\mathbf{b}, \quad \mathbf{C}^b\dot{\mathbf{b}} = -\mathbf{D}^b\mathbf{M}^{-1}\mathbf{p} + \mathbf{Q}^{ba}\mathbf{a} + \mathbf{Q}^{bb}\mathbf{b} \tag{7.25}$$

The formulation just derived is the first to exploit nonholonomic Hamiltonian methods in order to obtain an energy conserving multiscale multiphysics model of a mixed classical-quantum system incorporating a spinor wave function. It generalizes previous work [202, 203, 204, 205], for muliphysics systems

modeled at a variety of scales, and may be further extended to include relativistic effects (Dirac formulation). The method may be applied to model either an NVT or an NVE ($R = 0$) ensemble, and may be generalized to incorporate a variety of additional quantum, molecular, and macro scale physics.

The preceding general formulation may be specialized to the plane wave interpolation case. In that case, the interpolation functions are orthogonal and may be normalized so that

$$\mathbf{C}^a = \mathbf{C}^b = i\hbar\,\mathbf{I}, \quad \mathbf{D}^a = \mathbf{D}^b = \mathbf{0} \tag{7.26}$$

and the state equations are

$$\dot{\mathbf{p}} = -\frac{\partial H}{\partial \mathbf{q}} + \mathbf{F}^{ext} - \frac{R}{2nk_B}\left(1 - \frac{\theta_e}{\theta}\right)\mathbf{p} \tag{7.27}$$

$$\dot{\mathbf{q}} = \mathbf{M}^{-1}\mathbf{p} \tag{7.28}$$

$$i\hbar\,\dot{\mathbf{a}} = \mathbf{Q}^{aa}\mathbf{a} + \mathbf{Q}^{ab}\mathbf{b}, \quad i\hbar\,\dot{\mathbf{b}} = \mathbf{Q}^{ba}\mathbf{a} + \mathbf{Q}^{bb}\mathbf{b} \tag{7.29}$$

A bond graph representation of the plane wave case is shown in Figure 7.1, extending the research of Zhang [206]. The extensions include the addition of spin polarization and the modeling of interaction of the atomic nuclei with external electric and magnetic fields.

7.5 Summary

The research described in this chapter, formulating a new computational model of spin polarized sensing physics, can strongly complement experimental research in the study of mixed energy domain dynamics of quantum sensors.

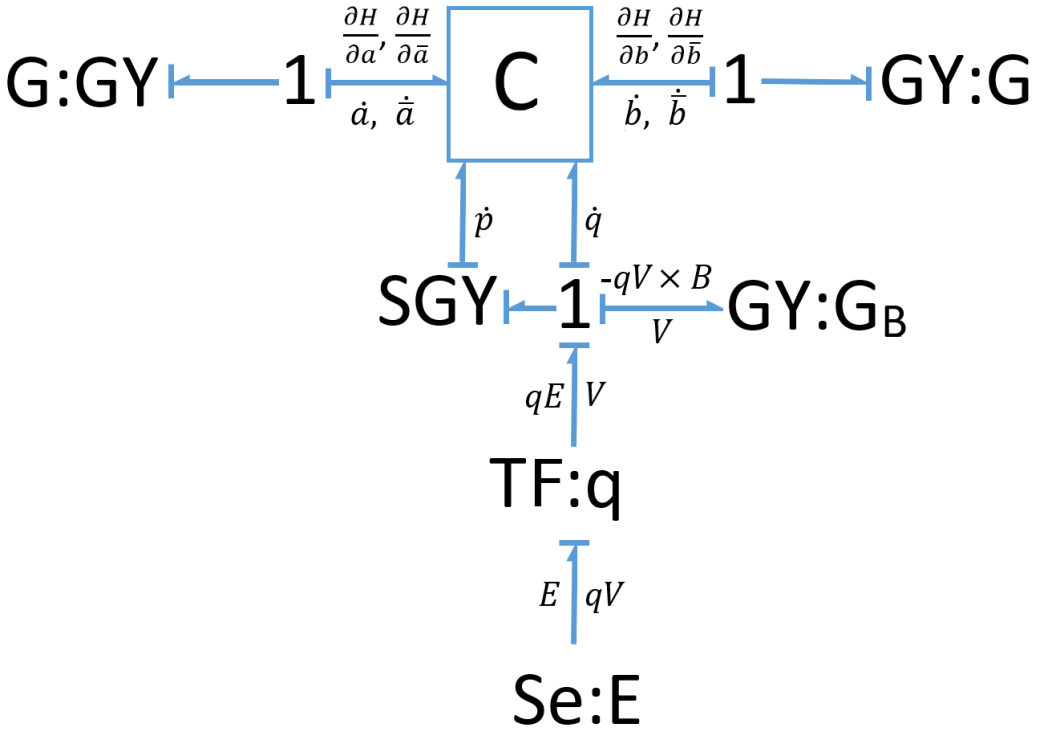

Figure 7.1: Bond graph of the new spin-polarized AIMD formulation

Chapter 8

Conclusion

Computational research plays a critical role in the development of explosives detection systems, due to both safety concerns and to severe restrictions on the distribution of controlled materials. This dissertation has applied both ab initio and statistical methods to investigate the performance of carbon nanotube based sensors in the trace detection of explosives. The results suggest that CNT based sensor arrays show excellent potential, offering opportunities for both sensitive and selective detection of explosive molecules.

The chemiresistive sensing performance of both metallic and semiconducting nanotubes was evaluated, in a variety of configurations, including internally doped, substitutionally doped, structurally flawed, and functionalized systems. All configurations were evaluated for their performance in a sensing array, for both sensitivity and selectivity in the detection of explosives. The computational results indicate that the proposed sensor arrays: (a) can distinguish common background gases from both nitroaromatic and nitramine explosives, (b) can distinguish between nitroaromatic and nitramine explosives, and (c) can distinguish similar nitramine explosives from each other. These results recommend the experimental study of improved explosive sensing de-

vices, devices based on the most productive CNT based sensor configurations investigated in this research.

Table 8.1 shows a comparison of the various sensor configurations analyzed in this dissertation. The comparison is based on the following five factors: (1) Ease of Manufacturing. Manufacturing processes have been established to produce CNTs with internal doping, lattice defects, and functionalizations; however, separating metallic and semiconducting CNTs is the critical issue. (2) Sensitivity. Sensitivity for the explosives, obtained from the computational research in this dissertation, is in the following sequence - CNTs with internal doping > CNTs with defects > CNTs with functionalization. (3) Selectivity. All four sensor arrays showed good selectivity towards the explosives, based on the Principal Component Analysis results in this dissertation. (4) Thermal Stability. Published experimental work indicates that internal doping is extremely stable [207]. Defects are also very stable and extremely high temperatures are required to change the defect density in CNTs [208]. Compared to internal doping and defects, functionalizations are relatively less stable [209]. (5) Chemical Stability. Internal doping places dopants inside the CNT so they do not react with the analytes outside the CNT. Published experimental work suggests that defects are also stable, although dangling bonds in certain defects (e.g. vacancy) can be terminated by reactive groups under suitable temperature and pressure conditions [210]. Compared to internal doping and defects, functionalizations are relatively less stable [211].

Comparing the various sensor configurations using these five criteria,

internal doping appears to be the most promising configuration, and the most practical configuration.

Next generation research on explosive sensor design must address three important issues: (a) modeling sensor performance at finite temperatures, (b) modeling sensor performance in mixed energy domain environments, in particular under applied electromagnetic fields, and (c) modeling sensor performance with spin polarization. A new ab initio molecular dynamics model has been formulated to address these issues. Development of the formulation is complete; future numerical implementation and validation work will allow this model to address the finite temperature, mixed energy domain dynamics problems important in the development of next generation explosives detection systems.

Major contributions. This dissertation makes three major contributions:

- It extended computational studies on CNT based wiring, by modeling CNTs doped with nine materials belonging to four material classes, in a unified framework. It showed the near-orthogonal performance characteristics of the various dopant types, for metallic and semiconducting CNTs, suggesting that fabricating high mass specific conductivity wiring from metallic/semiconducting CNT mixtures may be very difficult.

- It compared the chemiresistive sensing performance of four CNT based sensor array configurations for explosive molecules. It showed that sensor

arrays have great potential for the selective detection of explosives, and suggested that CNT sensor arrays with internal doping are the most practical design choice.

- It developed a new ab initio molecular dynamics formulation which generalizes Ehrenfest methods, extending a previous formulation [206] to incorporate spin polarization and electromagnetic field loading.

Table 8.1: Comparison of the Sensor Configurations.

Comparison of the Sensor Configurations					
Sensor Configuration	Ease of Manufacturing	Sensitivity (explosives)	Selectivity (explosives)	Thermal Stability	Chemical Stability
Internal Doping	✓	Excellent	Excellent	Excellent[1]	Excellent
Lattice Defects	✓	Very Good	Excellent	Very Good[2]	Very Good[4]
Functionalized CNT(M)	✓*	Good	Excellent	Good[3]	Fair[5]
Functionalized CNT(S)	✓*	Good	Very Good	Good[3]	Fair[5]

*Controlled processes are available to produce functionalized CNTs; however, cost-effective methods are required for separating metallic and semiconducting CNTs.
1 Based on experiments on CNTs filled with metal halides [207].
2 Based on annealing experiments on CNTs with defects [208].
3 Based on experimental data [209] for COOH functionalized CNTs.
4 Based on experimental observations on defect termination [210].
5 Based on experiments that use covalent functionalization of CNTs to attach them to polymers [211].

Appendix

Appendix 1

van der Waals Effects

The SIESTA modeling results presented in this dissertation are obtained using a generalized gradient approximation (GGA) with the Perdew-Burke-Ernzerhof (PBE) parameterization [4]. In order to evaluate the effect of adding van der Waals interactions, several test problems were solved using: (1) GGA-PBE, (2) the van der Waals (VDW) correlation functional with DRSLL (Dion-Rydberg, Schroeder-Langreth-Lundqvist) [212] parameterization, and (3) GGA-PBE plus molecular mechanics potentials describing species interactions [213, 214, 215]. The molecular mechanics potentials chosen for the tests were Grimme dispersion potentials[216] (the C_6 parameters and the van der Waals radii were taken from the work of Grimme [216]).

Table 1.1 compares computed results for the bond lengths of several dopant molecules, for all three methods, with published experimental data. The bond lengths computed using GGA-PBE and GGA-PBE+MM match to three significant figures, and show better agreement with the experimental data than does VDW-DRSLL. Consistent with previous work [217, 218, 219], the bond lengths computed by VDW are overestimated. Table 1.2 compares computed results for the equilibrium standoffs of three monatomic and three

diatomic dopants from the surface of a metallic carbon nanotube. As in the case of the bond length calculations, the GGA-PBE and GGA-PBE+MM results agree to three significant figures, while the differences with VDW-DRSLL range from -0.02 to +0.06 Å. Since the effects of adding van der Waals interactions appear to be small, and since the GGA-PBE formulation appears to show the best agreement with experiments, all of the results presented in the main text were computed using the GGA-PBE formulation.

Table 1.1: Comparison of computed dopant molecule bond lengths

Dopant	Model	Equilibrium Bond Length (Å)
ICl	GGA	2.37
	GGA+MM	2.37
	VDW	2.40
	Experiment	2.32[220], 2.35[29]
IBr	GGA	2.52
	GGA+MM	2.52
	VDW	2.55
	Experiment	2.47[221], 2.49[29]
LiBr	GGA	2.22
	GGA+MM	2.22
	VDW	2.24
	Experiment	2.17[222]

Table 1.2: Interaction of CNT and dopants

System	Model	Equilibrium Standoff (Å)
CNT(M)+Iodine	GGA	3.17
	GGA+MM	3.17
	VDW	3.17
CNT(M)+Bromine	GGA	2.86
	GGA+MM	2.86
	VDW	2.86
CNT(M)+Lithium	GGA	1.86
	GGA+MM	1.86
	VDW	1.94
CNT(M)+ICl	GGA	3.34
	GGA+MM	3.34
	VDW	3.32
CNT(M)+IBr	GGA	3.42
	GGA+MM	3.42
	VDW	3.41
CNT(M)+LiBr	GGA	3.38
	GGA+MM	3.38
	VDW	3.41

Bibliography

[1] J. Chen, K. Wang, and W. Zhou, "Vertically aligned ZnO nanorod arrays coated with SnO_2/noble metal nanoparticles for highly sensitive and selective gas detection," *IEEE Transactions on Nanotechnology*, vol. 10, no. 5, pp. 968–974, 2010.

[2] Y. Zhang, M. Xu, B. R. Bunes, N. Wu, D. E. Gross, J. S. Moore, and L. Zang, "Oligomer-coated carbon nanotube chemiresistive sensors for selective detection of nitroaromatic explosives," *ACS Applied Materials & Interfaces*, vol. 7, no. 14, pp. 7471–7475, 2015.

[3] L. Wei, D. Lu, J. Wang, H. Wei, J. Zhao, H. Geng, and Y. Zhang, "Highly sensitive detection of trinitrotoluene in water by chemiresistive sensor based on noncovalently amino functionalized single-walled carbon nanotube," *Sensors and Actuators B: Chemical*, vol. 190, pp. 529–534, 2014.

[4] J. M. Soler, E. Artacho, J. D. Gale, A. Garcia, J. Junquera, P. Ordejon, and D. Sanchez-Portal, "The SIESTA method for ab initio order-N materials simulation," *Journal of Physics: Condensed Matter*, vol. 14, no. 11, p. 2745, 2002.

[5] K. Stokbro, J. Taylor, M. Brandbyge, and P. Ordejon, "TranSIESTA:

a spice for molecular electronics," *Annals of the New York Academy of Sciences*, vol. 1006, no. 1, pp. 212–226, 2003.

[6] Y. Imry and R. Landauer, "Conductance viewed as transmission," *Reviews of Modern Physics*, vol. 71, no. 2, p. S306, 1999.

[7] J. Kong, E. Yenilmez, T. W. Tombler, W. Kim, H. Dai, R. B. Laughlin, L. Liu, C. Jayanthi, and S. Wu, "Quantum interference and ballistic transmission in nanotube electron waveguides," *Physical Review Letters*, vol. 87, no. 10, pp. 106–801, 2001.

[8] A. García, N. Papior, A. Akhtar, E. Artacho, V. Blum, E. Bosoni, P. Brandimarte, M. Brandbyge, J. I. Cerdá, F. Corsetti, *et al.*, "Siesta: Recent developments and applications," *The Journal of chemical physics*, vol. 152, no. 20, p. 204108, 2020.

[9] M. Kolmer, P. Brandimarte, J. Lis, R. Zuzak, S. Godlewski, H. Kawai, A. Garcia-Lekue, N. Lorente, T. Frederiksen, C. Joachim, *et al.*, "Electronic transport in planar atomic-scale structures measured by two-probe scanning tunneling spectroscopy," *Nature communications*, vol. 10, no. 1, pp. 1–10, 2019.

[10] G. T. Feliciano, A. J. da Silva, G. Reguera, and E. Artacho, "Molecular and electronic structure of the peptide subunit of geobacter sulfurreducens conductive pili from first principles," *The Journal of Physical Chemistry A*, vol. 116, no. 30, pp. 8023–8030, 2012.

[11] F. Vines, J. R. Gomes, and F. Illas, "Understanding the reactivity of metallic nanoparticles: beyond the extended surface model for catalysis," *Chemical Society Reviews*, vol. 43, no. 14, pp. 4922–4939, 2014.

[12] J. M. Schnorr, D. van der Zwaag, J. J. Walish, Y. Weizmann, and T. M. Swager, "Sensory arrays of covalently functionalized single-walled carbon nanotubes for explosive detection," *Advanced Functional Materials*, vol. 23, no. 42, pp. 5285–5291, 2013.

[13] M. Kermit and O. Tomic, "Independent component analysis applied on gas sensor array measurement data," *IEEE Sensors Journal*, vol. 3, no. 2, pp. 218–228, 2003.

[14] Z. Xiaobo, Z. Jiewen, W. Shouyi, and H. Xingyi, "Vinegar classification based on feature extraction and selection from tin oxide gas sensor array data," *Sensors*, vol. 3, no. 4, pp. 101–109, 2003.

[15] A. S. R. Murthy, D. Pathak, G. Sharma, K. Gnanasekar, V. Jayaraman, A. Umarji, and T. Gnanasekaran, "Application of principal component analysis to gas sensing characteristics of Cr0.8Fe0.2NbO4 thick film array," *Analytica Chimica Acta*, vol. 892, pp. 175–182, 2015.

[16] A. Hannon, Y. Lu, J. Li, and M. Meyyappan, "A sensor array for the detection and discrimination of methane and other environmental pollutant gases," *Sensors*, vol. 16, no. 8, p. 1163, 2016.

[17] Z. Li, J. R. Askim, and K. S. Suslick, "The optoelectronic nose: Colorimetric and fluorometric sensor arrays," *Chemical Reviews*, vol. 119, no. 1, pp. 231–292, 2019. PMID: 30207700.

[18] I. T. Jolliffe and J. Cadima, "Principal component analysis: a review and recent developments," *Philosophical Transactions of the Royal Society A: Mathematical, Physical and Engineering Sciences*, vol. 374, no. 2065, p. 20150202, 2016.

[19] J. E. Jackson, *A user's guide to principal components*, vol. 587. John Wiley & Sons, 2005.

[20] M. Meyyappan, *Carbon Nanotubes: Science and Applications*. CRC press, 2004.

[21] W. Lu, M. Zu, J.-H. Byun, B.-S. Kim, and T.-W. Chou, "State of the art of carbon nanotube fibers: opportunities and challenges," *Advanced Materials*, vol. 24, no. 14, pp. 1805–1833, 2012.

[22] A. Lekawa-Raus, J. Patmore, L. Kurzepa, J. Bulmer, and K. Koziol, "Electrical properties of carbon nanotube based fibers and their future use in electrical wiring," *Advanced Functional Materials*, vol. 24, no. 24, pp. 3661–3682, 2014.

[23] S. Zhang, N. Nguyen, B. Leonhardt, C. Jolowsky, A. Hao, J. G. Park, and R. Liang, "Carbon-Nanotube-Based Electrical Conductors: Fabri-

cation, Optimization, and Applications," *Advanced Electronic Materials*, pp. 800–811, 2019.

[24] R. Downes, S. Wang, D. Haldane, A. Moench, and R. Liang, "Strain-induced alignment mechanisms of carbon nanotube networks," *Advanced Engineering Materials*, vol. 17, no. 3, pp. 349–358, 2015.

[25] I. Puchades, C. C. Lawlor, C. M. Schauerman, A. R. Bucossi, J. E. Rossi, N. D. Cox, and B. J. Landi, "Mechanism of chemical doping in electronic-type-separated single wall carbon nanotubes towards high electrical conductivity," *Journal of Materials Chemistry C*, vol. 3, no. 39, pp. 10256–10266, 2015.

[26] Y. Zhao, J. Wei, R. Vajtai, P. M. Ajayan, and E. V. Barrera, "Iodine doped carbon nanotube cables exceeding specific electrical conductivity of metals," *Scientific Reports*, vol. 1, p. 83, 2011.

[27] R. Lee, H. Kim, J. Fischer, A. Thess, and R. E. Smalley, "Conductivity enhancement in single-walled carbon nanotube bundles doped with K and Br," *Nature*, vol. 388, no. 6639, p. 255, 1997.

[28] J. Alvarenga, P. R. Jarosz, C. M. Schauerman, B. T. Moses, B. J. Landi, C. D. Cress, and R. P. Raffaelle, "High conductivity carbon nanotube wires from radial densification and ionic doping," *Applied Physics Letters*, vol. 97, no. 18, p. 182106, 2010.

[29] D. Janas, K. Z. Milowska, P. D. Bristowe, and K. K. Koziol, "Improving the electrical properties of carbon nanotubes with interhalogen compounds," *Nanoscale*, vol. 9, no. 9, pp. 3212–3221, 2017.

[30] R. Jackson, B. Domercq, R. Jain, B. Kippelen, and S. Graham, "Stability of doped transparent carbon nanotube electrodes," *Advanced Functional Materials*, vol. 18, no. 17, pp. 2548–2554, 2008.

[31] X. Yang and J. Ni, "Metal-semiconductor and semiconductor-semiconductor transitions in carbon nanotubes induced by intercalating alkali atoms," *Physical Review B*, vol. 71, no. 16, p. 165438, 2005.

[32] S. Ghosh, S. S. Yamijala, S. K. Pati, and C. Rao, "The interaction of halogen molecules with SWNTs and graphene," *RSC Advances*, vol. 2, no. 3, pp. 1181–1188, 2012.

[33] E. Y. Li and N. Marzari, "Improving the electrical conductivity of carbon nanotube networks: A first-principles study," *ACS Nano*, vol. 5, no. 12, pp. 9726–9736, 2011.

[34] S. Ciraci, A. Buldum, and I. P. Batra, "Quantum effects in electrical and thermal transport through nanowires," *Journal of Physics: Condensed Matter*, vol. 13, no. 29, p. R537, 2001.

[35] Y. Li and E. Fahrenthold, "Ab Initio Study of Iodine-Doped Carbon Nanotube Conductors," *Journal of Engineering Materials and Technology*, vol. 140, no. 2, p. 021008, 2018.

[36] K. Y. Chin, "Molecular Doping of Carbon Nanotube Conductors," *Masters Thesis, University of Texas at Austin*, 2018.

[37] K. Y. Chin and E. P. Fahrenthold, "Mass specific performance of potassium tetrabromoaurate as a carbon nanotube dopant," *Computational Materials Science*, vol. 197, p. 110573, 2021.

[38] A. Fujiwara, K. Ishii, H. Suematsu, H. Kataura, Y. Maniwa, S. Suzuki, and Y. Achiba, "Gas adsorption in the inside and outside of single-walled carbon nanotubes," *Chemical Physics Letters*, vol. 336, no. 3-4, pp. 205–211, 2001.

[39] D. Mann, A. Javey, J. Kong, Q. Wang, and H. Dai, "Ballistic transport in metallic nanotubes with reliable Pd ohmic contacts," *Nano Letters*, vol. 3, no. 11, pp. 1541–1544, 2003.

[40] R. A. Matula, "Electrical resistivity of copper, gold, palladium, and silver," *Journal of Physical and Chemical Reference Data*, vol. 8, no. 4, pp. 1147–1298, 1979.

[41] D. Janas, A. P. Herman, S. Boncel, and K. K. Koziol, "Iodine monochloride as a powerful enhancer of electrical conductivity of carbon nanotube wires," *Carbon*, vol. 73, pp. 225–233, 2014.

[42] V. Schroeder, S. Savagatrup, M. He, S. Lin, and T. M. Swager, "Carbon nanotube chemical sensors," *Chemical Reviews*, vol. 119, no. 1, pp. 599–663, 2019.

[43] A. D. Rushi, K. P. Datta, P. S. Ghosh, A. Mulchandani, and M. D. Shirsat, "Functionalized carbon nanotubes for detection of volatile organic pollutant," in *Perspective of Carbon Nanotubes*, IntechOpen, 2019.

[44] N. D. Hoa, N. Van Quy, Y. Cho, and D. Kim, "An ammonia gas sensor based on non-catalytically synthesized carbon nanotubes on an anodic aluminum oxide template," *Sensors and Actuators B: Chemical*, vol. 127, no. 2, pp. 447–454, 2007.

[45] M. Muris, N. Dufau, M. Bienfait, N. Dupont-Pavlovsky, Y. Grillet, and J. Palmari, "Methane and krypton adsorption on single-walled carbon nanotubes," *Langmuir*, vol. 16, no. 17, pp. 7019–7022, 2000.

[46] P. Pannopard, P. Khongpracha, M. Probst, and J. Limtrakul, "Gas sensing properties of platinum derivatives of single-walled carbon nanotubes: A dft analysis," *Journal of Molecular Graphics and Modelling*, vol. 28, no. 1, pp. 62–69, 2009.

[47] X. Zhang, H. Cui, Y. Gui, and J. Tang, "Mechanism and application of carbon nanotube sensors in sf 6 decomposed production detection: a review," *Nanoscale Research Letters*, vol. 12, no. 1, pp. 1–12, 2017.

[48] A. Hannon, Y. Lu, H. Hong, J. Li, and M. Meyyappan, "Functionalized-Carbon Nanotube Sensor for Room Temperature Ammonia Detection," *Sensor Letters*, vol. 12, no. 10, pp. 1469–1476, 2014.

[49] Y. Battie, O. Ducloux, P. Thobois, T. Susi, E. I. Kauppinen, and A. Loiseau, "Selective differential ammonia gas sensor based on N-doped SWCNT films," *Physica Status Solidi (B)*, vol. 248, no. 11, pp. 2462–2466, 2011.

[50] J. Kim, S.-W. Choi, J.-H. Lee, Y. Chung, and Y. T. Byun, "Gas sensing properties of defect-induced single-walled carbon nanotubes," *Sensors and Actuators B: Chemical*, vol. 228, pp. 688–692, 2016.

[51] M. Green, "The opening and filling of single walled carbon nanotubes (swts)," *Chemical Communications*, no. 3, pp. 347–348, 1998.

[52] A. Govindaraj, B. Satishkumar, M. Nath, and C. N. R. Rao, "Metal nanowires and intercalated metal layers in single-walled carbon nanotube bundles," in *Advances In Chemistry: A Selection of CNR Rao's Publications (1994–2003)*, pp. 334–337, World Scientific, 2003.

[53] D. Wright, A. P. E. York, K. S. Coleman, M. L. H. Green, and J. L. Hutchison, "Capillarity and silver nanowire formation observed in single walled carbon nanotubes," *Chemical Communications*, no. 8, pp. 699–700, 1999.

[54] A. Kuznetsova, J. Yates Jr, J. Liu, and R. Smalley, "Physical adsorption of xenon in open single walled carbon nanotubes: Observation of a quasi-one-dimensional confined xe phase," *The Journal of Chemical Physics*, vol. 112, no. 21, pp. 9590–9598, 2000.

[55] M. Babaa, N. Dupont-Pavlovsky, E. McRae, and K. Masenelli-Varlot, "Physical adsorption of carbon tetrachloride on as-produced and on mechanically opened single walled carbon nanotubes," *Carbon*, vol. 42, no. 8-9, pp. 1549–1554, 2004.

[56] Z. Wang, Z. Shi, and Z. Gu, "Synthesis of single-walled carbon nanotube/metal nanoparticle hybrid materials from potassium-filled nanotubes," *Carbon*, vol. 48, no. 2, pp. 443–446, 2010.

[57] X. Fan, E. Dickey, P. Eklund, K. Williams, L. Grigorian, R. Buczko, S. Pantelides, and S. Pennycook, "Atomic arrangement of iodine atoms inside single-walled carbon nanotubes," *Physical Review Letters*, vol. 84, no. 20, p. 4621, 2000.

[58] J. Sloan, M. Novotny, S. Bailey, G. Brown, C. Xu, V. Williams, S. Friedrichs, E. Flahaut, R. Callender, A. York, *et al.*, "Two layer 4: 4 co-ordinated ki crystals grown within single walled carbon nanotubes," *Chemical Physics Letters*, vol. 329, no. 1-2, pp. 61–65, 2000.

[59] A. Leonhardt, M. Ritschel, R. Kozhuharova, A. Graff, T. Mühl, R. Huhle, I. Mönch, D. Elefant, and C. Schneider, "Synthesis and properties of filled carbon nanotubes," *Diamond and Related Materials*, vol. 12, no. 3-7, pp. 790–793, 2003.

[60] I. Stepanek, G. Maurin, P. Bernier, J. Gavillet, A. Loiseau, R. Edwards, and O. Jaschinski, "Nano-mechanical cutting and opening of single wall

carbon nanotubes," *Chemical Physics Letters*, vol. 331, no. 2-4, pp. 125–131, 2000.

[61] P. Ajayan, T. Ebbesen, T. Ichihashi, S. Iijima, K. Tanigaki, and H. Hiura, "Opening carbon nanotubes with oxygen and implications for filling," *Nature*, vol. 362, no. 6420, pp. 522–525, 1993.

[62] M. V. Kharlamova, "Electronic properties of pristine and modified single-walled carbon nanotubes," *Physics-Uspekhi*, vol. 56, no. 11, p. 1047, 2013.

[63] M. Chernysheva, A. Eliseev, A. Lukashin, Y. D. Tretyakov, S. Savilov, N. Kiselev, O. Zhigalina, A. Kumskov, A. Krestinin, and J. Hutchison, "Filling of single-walled carbon nanotubes by cui nanocrystals via capillary technique," *Physica E: Low-dimensional Systems and Nanostructures*, vol. 37, no. 1-2, pp. 62–65, 2007.

[64] E. L. Sceats, J. C. Green, and S. Reich, "Theoretical study of the molecular and electronic structure of one-dimensional crystals of potassium iodide and composites formed upon intercalation in single-walled carbon nanotubes," *Physical Review B*, vol. 73, no. 12, p. 125441, 2006.

[65] A. Eliseev, L. Yashina, N. Verbitskiy, M. Brzhezinskaya, M. Kharlamova, M. Chernysheva, A. Lukashin, N. Kiselev, A. Kumskov, and B. Freitag, "Interaction between single walled carbon nanotube and 1d crystal in cux@ swcnt (x= cl, br, i) nanostructures," *Carbon*, vol. 50, no. 11, pp. 4021–4039, 2012.

[66] E. Galpern, I. Stankevich, A. Chistykov, and L. Chernozatonskii, "Carbon nanotubes with metal inside: electron structure of tubelenes [li@ c24] n and [k@ c36] n," *Chemical Physics Letters*, vol. 214, no. 3-4, pp. 345–348, 1993.

[67] J. Zhou, X. Yan, G. Luo, R. Qin, H. Li, J. Lu, W. N. Mei, and Z. Gao, "Structural, electronic, and transport properties of gd/eu atomic chains encapsulated in single-walled carbon nanotubes," *The Journal of Physical Chemistry C*, vol. 114, no. 36, pp. 15347–15353, 2010.

[68] O. M. Korsun, O. N. Kalugin, A. S. Vasenko, and O. V. Prezhdo, "Electronic properties of carbon nanotubes intercalated with li+ and mg2+: effects of ion charge and ion solvation," *The Journal of Physical Chemistry C*, vol. 120, no. 46, pp. 26514–26521, 2016.

[69] A. E. Goldt, O. T. Zaremba, M. O. Bulavskiy, F. S. Fedorov, K. V. Larionov, A. P. Tsapenko, Z. I. Popov, P. Sorokin, A. S. Anisimov, H. Inani, *et al.*, "Highly efficient bilateral doping of single-walled carbon nanotubes," *Journal of Materials Chemistry C*, vol. 9, no. 13, pp. 4514–4521, 2021.

[70] K. C. To, S. Ben-Jaber, and I. P. Parkin, "Recent developments in the field of explosive trace detection," *ACS Nano*, vol. 14, no. 9, pp. 10804–10833, 2020.

[71] S. Stewart, M. A. Ivy, and E. V. Anslyn, "The use of principal component analysis and discriminant analysis in differential sensing routines,"

Chemical Society Reviews, vol. 43, no. 1, pp. 70–84, 2014.

[72] Y. Xu, X. Zhao, Y. Chen, and W. Zhao, "Research on a mixed gas recognition and concentration detection algorithm based on a metal oxide semiconductor olfactory system sensor array," *Sensors*, vol. 18, no. 10, p. 3264, 2018.

[73] N. R. Council, "Existing and potential standoff explosives detection techniques," tech. rep., 2004.

[74] K. A. Morrison, E. H. Denis, M. K. Nims, A. M. Broderick, R. C. Fausey, H. J. Rose, P. E. Gongwer, and R. G. Ewing, "Vapor pressures of rdx and hmx explosives measured at and near room temperature: 1, 3, 5-trinitro-1, 3, 5-triazinane and 1, 3, 5, 7-tetranitro-1, 3, 5, 7-tetrazocane," *The Journal of Physical Chemistry A*, vol. 125, no. 5, pp. 1279–1288, 2021.

[75] C. Tancharoen, W. Sukjee, P.-t. Yenchitsomanus, A. Panya, P. A. Lieberzeit, and C. Sangma, "Selectivity enhancement of mip-composite sensor for explosive detection using dnt-dengue virus template: a co-imprinting approach," *Materials Letters*, vol. 285, p. 129201, 2021.

[76] Y. Hashimoto, "Development of a miniature mass spectrometer and an automated detector for sampling explosive materials," *Mass Spectrometry*, vol. 6, no. 1, pp. A0054–A0054, 2017.

[77] L. Senesac and T. G. Thundat, "Nanosensors for trace explosive detection," *Materials Today*, vol. 11, no. 3, pp. 28–36, 2008.

[78] P.-C. Chen, S. Sukcharoenchoke, K. Ryu, L. Gomez de Arco, A. Badmaev, C. Wang, and C. Zhou, "2, 4, 6-Trinitrotoluene (TNT) chemical sensing based on aligned single-walled carbon nanotubes and ZnO nanowires," *Advanced Materials*, vol. 22, no. 17, pp. 1900–1904, 2010.

[79] M. Meyyappan, "Carbon Nanotube-Based Chemical Sensors," *Small*, vol. 12, no. 16, pp. 2118–2129, 2016.

[80] R. Tang, Y. Shi, Z. Hou, and L. Wei, "Carbon nanotube-based chemiresistive sensors," *Sensors*, vol. 17, no. 4, p. 882, 2017.

[81] J. Zhang and E. P. Fahrenthold, "Graphene nanoribbons as flexible docks for chemiresistive sensing of gas phase explosives," *Nanoscale*, vol. 12, no. 19, pp. 10730–10736, 2020.

[82] P. G. Collins, K. Bradley, M. Ishigami, and d. A. Zettl, "Extreme oxygen sensitivity of electronic properties of carbon nanotubes," *Science*, vol. 287, no. 5459, pp. 1801–1804, 2000.

[83] C. Huang, B. Huang, Y. Jang, M. Tsai, and C. Yeh, "Three-terminal cnts gas sensor for n2 detection," *Diamond and related materials*, vol. 14, no. 11-12, pp. 1872–1875, 2005.

[84] L. Valentini, F. Mercuri, I. Armentano, C. Cantalini, S. Picozzi, L. Lozzi, S. Santucci, A. Sgamellotti, and J. Kenny, "Role of defects on the gas sensing properties of carbon nanotubes thin films: experiment and theory," *Chemical Physics Letters*, vol. 387, no. 4, pp. 356–361, 2004.

[85] D. Ding, Z. Chen, S. Rajaputra, and V. Singh, "Hydrogen sensors based on aligned carbon nanotubes in an anodic aluminum oxide template with palladium as a top electrode," *Sensors and Actuators B: Chemical*, vol. 124, no. 1, pp. 12–17, 2007.

[86] J. Suehiro, S. Yamane, and K. Imasaka, "Carbon nanotube-based hydrogen gas sensor electrochemically functionalized with palladium," in *Sensors, 2007 IEEE*, pp. 554–557, IEEE, 2007.

[87] J. Novak, E. Snow, E. Houser, D. Park, J. Stepnowski, and R. McGill, "Nerve agent detection using networks of single-walled carbon nanotubes," *Applied Physics Letters*, vol. 83, no. 19, pp. 4026–4028, 2003.

[88] J. Zhao, A. Buldum, J. Han, and J. P. Lu, "Gas molecule adsorption in carbon nanotubes and nanotube bundles," *Nanotechnology*, vol. 13, no. 2, p. 195, 2002.

[89] N. Chakrapani, Y. M. Zhang, S. K. Nayak, J. A. Moore, D. L. Carroll, Y. Y. Choi, and P. M. Ajayan, "Chemisorption of acetone on carbon nanotubes," *The Journal of Physical Chemistry B*, vol. 107, no. 35, pp. 9308–9311, 2003.

[90] J. A. Robinson, E. S. Snow, S. C. Badescu, T. L. Reinecke, and F. K. Perkins, "Role of defects in single-walled carbon nanotube chemical sensors," *Nano Letters*, vol. 6, no. 8, pp. 1747–1751, 2006.

[91] A. Hankins, T. C. Willard, A. Y. Liu, and M. Paranjape, "Role of defects in the sensing mechanism of cntfet gas sensors," *Journal of Applied Physics*, vol. 128, no. 8, p. 084501, 2020.

[92] P. Ayala, A. Grüneis, T. Gemming, D. Grimm, C. Kramberger, M. H. Rümmeli, F. L. Freire Jr, H. Kuzmany, R. Pfeiffer, A. Barreiro, *et al.*, "Tailoring N-doped single and double wall carbon nanotubes from a nondiluted carbon/nitrogen feedstock," *The Journal of Physical Chemistry C*, vol. 111, no. 7, pp. 2879–2884, 2007.

[93] Y. Wang, X. Cui, Y. Li, L. Chen, H. Chen, L. Zhang, and J. Shi, "A copyrolysis route to synthesize nitrogen doped multiwall carbon nanotubes for oxygen reduction reaction," *Carbon*, vol. 68, pp. 232–239, 2014.

[94] K. McGuire, N. Gothard, P. Gai, M. Dresselhaus, G. Sumanasekera, and A. Rao, "Synthesis and Raman characterization of boron-doped single-walled carbon nanotubes," *Carbon*, vol. 43, no. 2, pp. 219–227, 2005.

[95] O. Stephan, P. Ajayan, C. Colliex, P. Redlich, J. Lambert, P. Bernier, and P. Lefin, "Doping graphitic and carbon nanotube structures with boron and nitrogen," *Science*, vol. 266, no. 5191, pp. 1683–1685, 1994.

[96] A. A. Koos, F. Dillon, E. A. Obraztsova, A. Crossley, and N. Grobert, "Comparison of structural changes in nitrogen and boron-doped multi-walled carbon nanotubes," *Carbon*, vol. 48, no. 11, pp. 3033–3041, 2010.

[97] J.-J. Adjizian, R. Leghrib, A. A. Koos, I. Suarez-Martinez, A. Crossley, P. Wagner, N. Grobert, E. Llobet, and C. P. Ewels, "Boron-and nitrogen-doped multi-wall carbon nanotubes for gas detection," *Carbon*, vol. 66, pp. 662–673, 2014.

[98] W. Muangrat, W. Wongwiriyapan, V. Yordsri, T. Chobsilp, S. Inpaeng, C. Issro, O. Domanov, P. Ayala, T. Pichler, and L. Shi, "Unravel the active site in nitrogen-doped double-walled carbon nanotubes for nitrogen dioxide gas sensor," *physica status solidi (a)*, vol. 215, no. 13, p. 1800004, 2018.

[99] P. Ajayan, V. Ravikumar, and J.-C. Charlier, "Surface reconstructions and dimensional changes in single-walled carbon nanotubes," *Physical Review Letters*, vol. 81, no. 7, p. 1437, 1998.

[100] A. Hashimoto, K. Suenaga, A. Gloter, K. Urita, and S. Iijima, "Direct evidence for atomic defects in graphene layers," *nature*, vol. 430, no. 7002, pp. 870–873, 2004.

[101] K. Suenaga, H. Wakabayashi, M. Koshino, Y. Sato, K. Urita, and S. Iijima, "Imaging active topological defects in carbon nanotubes," *Nature Nanotechnology*, vol. 2, no. 6, pp. 358–360, 2007.

[102] M. Bockrath, W. Liang, D. Bozovic, J. H. Hafner, C. M. Lieber, M. Tinkham, and H. Park, "Resonant electron scattering by defects in single-walled carbon nanotubes," *Science*, vol. 291, no. 5502, pp. 283–285, 2001.

[103] N. Neophytou, D. Kienle, E. Polizzi, and M. Anantram, "Influence of defects on nanotube transistor performance," *Applied Physics Letters*, vol. 88, no. 24, p. 242106, 2006.

[104] X. Zhang, Y. Gui, and Z. Dai, "A simulation of pd-doped swcnts used to detect sf6 decomposition components under partial discharge," *Applied Surface Science*, vol. 315, pp. 196–202, 2014.

[105] N. Kuganathan and A. Chroneos, "Ru-doped single walled carbon nanotubes as sensors for so2 and h2s detection," *Chemosensors*, vol. 9, no. 6, p. 120, 2021.

[106] S. Demir and M. F. Fellah, "A dft study on pt doped (4, 0) swcnt: Co adsorption and sensing," *Applied Surface Science*, vol. 504, p. 144141, 2020.

[107] J. Andzelm, N. Govind, and A. Maiti, "Nanotube-based gas sensors–role of structural defects," *Chemical Physics Letters*, vol. 421, no. 1-3, pp. 58–62, 2006.

[108] C. S. Choi and H. P. Boutin, "A study of the crystal structure of beta-cyclotetramethylene tetranitramine by neutron diffraction," *Acta Crystallographica Section B: Structural Crystallography and Crystal Chemistry*, vol. 26, no. 9, pp. 1235–1240, 1970.

[109] C. S. Choi and E. Prince, "The crystal structure of cyclotrimethylenetrinitramine," *Acta Crystallographica Section B: Structural Crystallog-*

raphy and Crystal Chemistry, vol. 28, no. 9, pp. 2857–2862, 1972.

[110] R. M. Vrcelj, J. N. Sherwood, A. R. Kennedy, H. G. Gallagher, and T. Gelbrich, "Polymorphism in 2-4-6 trinitrotoluene," *Crystal growth and design*, vol. 3, no. 6, pp. 1027–1032, 2003.

[111] S. Krompiewski, "Spin-polarized transport through carbon nanotubes," *Physica Status Solidi (B)*, vol. 242, no. 2, pp. 226–233, 2005.

[112] H. Santos, L. Chico, J. Alvarellos, and A. Latge, "Defect-enhanced rashba spin-polarized currents in carbon nanotubes," *Physical Review B*, vol. 96, no. 16, p. 165401, 2017.

[113] Y.-W. Son, M. L. Cohen, and S. G. Louie, "Electric field effects on spin transport in defective metallic carbon nanotubes," *Nano letters*, vol. 7, no. 11, pp. 3518–3522, 2007.

[114] Q. Vermesh, O. Grecu, M. Javey, A. Wang, Q. Dai, H. Peng, and S. Cho, "Toward large array of multiplex functionalized carbon nanotube sensors for highly sensitive and selective molecular detection," *Nanotechnology Letters 3 (3)*, pp. 347–351, 2003.

[115] M. D. Shirsat, T. Sarkar, J. Kakoullis Jr, N. V. Myung, B. Konnanath, A. Spanias, and A. Mulchandani, "Porphyrin-functionalized single-walled carbon nanotube chemiresistive sensor arrays for VOCs," *The Journal of Physical Chemistry C*, vol. 116, no. 5, pp. 3845–3850, 2012.

[116] G. Sumanasekera, C. Adu, S. Fang, and P. Eklund, "Effects of gas adsorption and collisions on electrical transport in single-walled carbon nanotubes," *Physical Review Letters*, vol. 85, no. 5, p. 1096, 2000.

[117] E. S. Muckley, A. J. Nelson, C. B. Jacobs, and I. N. Ivanov, "Multimodal probing of oxygen and water interaction with metallic and semiconducting carbon nanotube networks under ultraviolet irradiation," *Journal of Photonics for Energy*, vol. 6, no. 2, p. 025506, 2016.

[118] F. Rigoni, S. Tognolini, P. Borghetti, G. Drera, S. Pagliara, A. Goldoni, and L. Sangaletti, "Enhancing the sensitivity of chemiresistor gas sensors based on pristine carbon nanotubes to detect low-ppb ammonia concentrations in the environment," *Analyst*, vol. 138, no. 24, pp. 7392–7399, 2013.

[119] G. Chen, T. M. Paronyan, E. M. Pigos, and A. R. Harutyunyan, "Enhanced gas sensing in pristine carbon nanotubes under continuous ultraviolet light illumination," *Scientific Reports*, vol. 2, no. 1, pp. 1–7, 2012.

[120] W. H. Shin, H. M. Jeong, B. G. Kim, J. K. Kang, and J. W. Choi, "Nitrogen-doped multiwall carbon nanotubes for lithium storage with extremely high capacity," *Nano letters*, vol. 12, no. 5, pp. 2283–2288, 2012.

[121] B. Liu, X. Sun, Z. Liao, X. Lu, L. Zhang, and G.-P. Hao, "Nitrogen and boron doped carbon layer coated multiwall carbon nanotubes as

high performance anode materials for lithium ion batteries," *Scientific Reports*, vol. 11, no. 1, pp. 1–11, 2021.

[122] L. Bulusheva, A. Okotrub, A. Kurenya, H. Zhang, H. Zhang, X. Chen, and H. Song, "Electrochemical properties of nitrogen-doped carbon nanotube anode in li-ion batteries," *Carbon*, vol. 49, no. 12, pp. 4013–4023, 2011.

[123] T. C. Nagaiah, S. Kundu, M. Bron, M. Muhler, and W. Schuhmann, "Nitrogen-doped carbon nanotubes as a cathode catalyst for the oxygen reduction reaction in alkaline medium," *Electrochemistry Communications*, vol. 12, no. 3, pp. 338–341, 2010.

[124] L. Chan, K. Hong, D. Xiao, T. Lin, S. Lai, W. Hsieh, and H. Shih, "Resolution of the binding configuration in nitrogen-doped carbon nanotubes," *Physical Review B*, vol. 70, no. 12, p. 125408, 2004.

[125] P. Ayala, W. Plank, A. Grüneis, E. I. Kauppinen, M. H. Rümmeli, H. Kuzmany, and T. Pichler, "A one step approach to B-doped single-walled carbon nanotubes," *Journal of Materials Chemistry*, vol. 18, no. 46, pp. 5676–5681, 2008.

[126] E. Borowiak-Palen, T. Pichler, A. Graff, R. Kalenczuk, M. Knupfer, and J. Fink, "Synthesis and electronic properties of B-doped single wall carbon nanotubes," *Carbon*, vol. 42, no. 5-6, pp. 1123–1126, 2004.

[127] K. Ang, D. Kulathunga, and J. Reddy, "Buckling of defective carbon nanotube," in *Proceedings of the International Conference on Computing in Civil and Building Engineering*, Nottingham University Press, 2010.

[128] M. Sammalkorpi, A. Krasheninnikov, A. Kuronen, K. Nordlund, and K. Kaski, "Mechanical properties of carbon nanotubes with vacancies and related defects," *Physical Review B*, vol. 70, no. 24, p. 245416, 2004.

[129] L. Zhou and S.-Q. Shi, "Formation energy of Stone–Wales defects in carbon nanotubes," *Applied Physics Letters*, vol. 83, no. 6, pp. 1222–1224, 2003.

[130] Q. Wang, W. Duan, N. Richards, and K. Liew, "Modeling of fracture of carbon nanotubes with vacancy defect," *Physical Review B*, vol. 75, no. 20, p. 201405, 2007.

[131] Z. Zanolli and J.-C. Charlier, "Defective carbon nanotubes for single-molecule sensing," *Physical Review B*, vol. 80, no. 15, p. 155447, 2009.

[132] C. Gómez-Navarro, P. J. De Pablo, J. Gómez-Herrero, B. Biel, F. Garcia-Vidal, A. Rubio, and F. Flores, "Tuning the conductance of single-walled carbon nanotubes by ion irradiation in the anderson localization regime," *Nature materials*, vol. 4, no. 7, pp. 534–539, 2005.

[133] D. B. Mawhinney, V. Naumenko, A. Kuznetsova, J. T. Yates Jr, J. Liu, and R. Smalley, "Surface defect site density on single walled carbon

nanotubes by titration," *Chemical Physics Letters*, vol. 324, no. 1-3, pp. 213–216, 2000.

[134] G.-D. Lee, C. Wang, E. Yoon, N.-M. Hwang, and K. Ho, "The formation of pentagon-heptagon pair defect by the reconstruction of vacancy defects in carbon nanotube," *Applied Physics Letters*, vol. 92, no. 4, p. 043104, 2008.

[135] Y.-H. Zhang, K.-G. Zhou, K.-F. Xie, X.-C. Gou, J. Zeng, H.-L. Zhang, and Y. Peng, "Effects of stone-wales defect on the interactions between nh3, no2 and graphene," *Journal of nanoscience and nanotechnology*, vol. 10, no. 11, pp. 7347–7350, 2010.

[136] J. Kong, N. R. Franklin, C. Zhou, M. G. Chapline, S. Peng, K. Cho, and H. Dai, "Nanotube Molecular Wires as Chemical Sensors," *Science*, vol. 287, no. 5453, pp. 622–625, 2000.

[137] P. Qi, O. Vermesh, M. Grecu, A. Javey, Q. Wang, H. Dai, S. Peng, and K. Cho, "Toward large arrays of multiplex functionalized carbon nanotube sensors for highly sensitive and selective molecular detection," *Nano letters*, vol. 3, no. 3, pp. 347–351, 2003.

[138] L. Valentini, I. Armentano, J. Kenny, C. Cantalini, L. Lozzi, and S. Santucci, "Sensors for sub-ppm NO2 gas detection based on carbon nanotube thin films," *Applied Physics Letters*, vol. 82, no. 6, pp. 961–963, 2003.

[139] A. G. Bannov, O. Jasek, A. Manakhov, M. Marik, D. Necas, and L. Zajickova, "High-performance ammonia gas sensors based on plasma treated carbon nanostructures," *IEEE Sensors Journal*, vol. 17, no. 7, pp. 1964–1970, 2017.

[140] D.-K. Lim, K.-S. Jeon, H. M. Kim, J.-M. Nam, and Y. D. Suh, "Nanogap-engineerable raman-active nanodumbbells for single-molecule detection," *Nature Materials*, vol. 9, no. 1, pp. 60–67, 2010.

[141] A. Azad, S. Akbar, S. Mhaisalkar, L. Birkefeld, and K. Goto, "Solid-state gas sensors: A review," *Journal of the Electrochemical Society*, vol. 139, no. 12, pp. 3690–3704, 1992.

[142] S. S. Varghese, S. Lonkar, K. Singh, S. Swaminathan, and A. Abdala, "Recent advances in graphene based gas sensors," *Sensors and Actuators B: Chemical*, vol. 218, pp. 160–183, 2015.

[143] S. Zampolli, I. Elmi, F. Ahmed, M. Passini, G. Cardinali, S. Nicoletti, and L. Dori, "An electronic nose based on solid state sensor arrays for low-cost indoor air quality monitoring applications," *Sensors and Actuators B: Chemical*, vol. 101, no. 1-2, pp. 39–46, 2004.

[144] K. Goswami, D. P. Saini, S. M. Klainer, and C. H. Ejiofor, "Solid state sensor for carbon monoxide," Apr. 11 1995. US Patent 5,405,583.

[145] C. Piloto, F. Mirri, E. A. Bengio, M. Notarianni, B. Gupta, M. Shafiei, M. Pasquali, and N. Motta, "Room temperature gas sensing properties of

ultrathin carbon nanotube films by surfactant-free dip coating," *Sensors and Actuators B: Chemical*, vol. 227, pp. 128–134, 2016.

[146] E. Dilonardo, M. Penza, M. Alvisi, C. Di Franco, R. Rossi, F. Palmisano, L. Torsi, and N. Cioffi, "Electrophoretic deposition of Au NPs on MWCNT-based gas sensor for tailored gas detection with enhanced sensing properties," *Sensors and Actuators B: Chemical*, vol. 223, pp. 417–428, 2016.

[147] K. Datta, P. Ghosh, M. More, M. Shirsat, and A. Mulchandani, "Controlled functionalization of single-walled carbon nanotubes for enhanced ammonia sensing: A comparative study," *Journal of Physics D: Applied Physics*, vol. 45, no. 35, p. 355305, 2012.

[148] J. F. Fennell Jr, S. F. Liu, J. M. Azzarelli, J. G. Weis, S. Rochat, K. A. Mirica, J. B. Ravnsbaek, and T. M. Swager, "Nanowire chemical/biological sensors: Status and a roadmap for the future," *Angewandte Chemie International Edition*, vol. 55, no. 4, pp. 1266–1281, 2016.

[149] A. Hirsch, "Functionalization of single-walled carbon nanotubes," *Angewandte Chemie International Edition*, vol. 41, no. 11, pp. 1853–1859, 2002.

[150] A. Hirsch and O. Vostrowsky, "Functionalization of carbon nanotubes," in *Functional Molecular Nanostructures*, pp. 193–237, Springer, 2005.

[151] S. Gaikwad, G. Bodkhe, M. Deshmukh, H. Patil, A. Rushi, M. D. Shirsat, P. Koinkar, Y.-H. Kim, and A. Mulchandani, "Chemiresistive sensor based on polythiophene-modified single-walled carbon nanotubes for detection of NO2," *Modern Physics Letters B*, vol. 29, p. 1540046, 2015.

[152] T. Zhang, M. B. Nix, B.-Y. Yoo, M. A. Deshusses, and N. V. Myung, "Electrochemically functionalized single-walled carbon nanotube gas sensor," *Electroanalysis*, vol. 18, no. 12, pp. 1153–1158, 2006.

[153] Y. Li, G. Li, X. Wang, Z. Zhu, H. Ma, T. Zhang, and J. Jin, "Poly (ionic liquid)-wrapped single-walled carbon nanotubes for sub-ppb detection of CO2," *Chemical Communications*, vol. 48, no. 66, pp. 8222–8224, 2012.

[154] P. Slobodian, P. Riha, A. Lengalova, P. Svoboda, and P. Saha, "Multi-wall carbon nanotube networks as potential resistive gas sensors for organic vapor detection," *Carbon*, vol. 49, no. 7, pp. 2499–2507, 2011.

[155] X. Zhang, F. Meng, and B. Yang, "Use of hydroxyl-modified carbon nanotubes for detecting sf 6 decomposition products under partial discharge in gas insulated switchgear," *IEEE Transactions on Dielectrics and Electrical Insulation*, vol. 20, no. 6, pp. 2246–2253, 2013.

[156] K.-Y. Dong, J. Choi, Y. D. Lee, B. H. Kang, Y.-Y. Yu, H. H. Choi, and B.-K. Ju, "Detection of a co and nh 3 gas mixture using carboxylic acid-functionalized single-walled carbon nanotubes," *Nanoscale Research Letters*, vol. 8, no. 1, pp. 1–6, 2013.

[157] M. L. Y. Sin, G. C. T. Chow, G. M. K. Wong, W. J. Li, P. H. W. Leong, and K. W. Wong, "Ultralow-power alcohol vapor sensors using chemically functionalized multiwalled carbon nanotubes," *IEEE Transactions on Nanotechnology*, vol. 6, no. 5, pp. 571–577, 2007.

[158] R. Afrin and N. Shah, "Room temperature gas sensors based on carboxyl and thiol functionalized carbon nanotubes buckypapers," *Diamond and Related Materials*, vol. 60, pp. 42–49, 2015.

[159] F. H. Allen, O. Kennard, D. G. Watson, L. Brammer, A. G. Orpen, and R. Taylor, "Tables of bond lengths determined by X-ray and neutron diffraction. Part 1. Bond lengths in organic compounds," *Journal of the Chemical Society, Perkin Transactions 2*, no. 12, pp. S1–S19, 1987.

[160] J. Zhao, H. Park, J. Han, and J. P. Lu, "Electronic properties of carbon nanotubes with covalent sidewall functionalization," *The Journal of Physical Chemistry B*, vol. 108, no. 14, pp. 4227–4230, 2004.

[161] K. S. Kim, D. J. Bae, J. R. Kim, K. A. Park, S. C. Lim, J.-J. Kim, W. B. Choi, C. Y. Park, and Y. H. Lee, "Modification of electronic structures of a carbon nanotube by hydrogen functionalization," *Advanced Materials*, vol. 14, no. 24, pp. 1818–1821, 2002.

[162] K. Z. Milowska and J. A. Majewski, "Functionalization of carbon nanotubes with–ch n,–nh n fragments,–cooh and–oh groups," *The Journal of Chemical Physics*, vol. 138, no. 19, p. 194704, 2013.

[163] Y. Wang, Z. Yang, Z. Hou, D. Xu, L. Wei, E. S.-W. Kong, and Y. Zhang, "Flexible gas sensors with assembled carbon nanotube thin films for DMMP vapor detection," *Sensors and Actuators B: Chemical*, vol. 150, no. 2, pp. 708–714, 2010.

[164] S. Ghosh, S. M. Bachilo, R. A. Simonette, K. M. Beckingham, and R. B. Weisman, "Oxygen doping modifies near-infrared band gaps in fluorescent single-walled carbon nanotubes," *Science*, vol. 330, no. 6011, pp. 1656–1659, 2010.

[165] Q. Chen, L. Dai, M. Gao, S. Huang, and A. Mau, "Plasma activation of carbon nanotubes for chemical modification," *The Journal of Physical Chemistry B*, vol. 105, no. 3, pp. 618–622, 2001.

[166] S. Sorgenfrei, C. Chiu, C. Nuckolls, and K. Shepard, "Ultra-sensitive carbon nanotubes for single-molecule detection of dna hybridization kinetics using conductance-based correlation spectroscopy," in *2011 16th International Solid-State Sensors, Actuators and Microsystems Conference*, pp. 882–885, IEEE, 2011.

[167] J. W. Brown, A. Bauer, M. E. Polinkovsky, A. Bhumkar, D. J. Hunter, K. Gaus, E. Sierecki, and Y. Gambin, "Single-molecule detection on a portable 3d-printed microscope," *Nature Communications*, vol. 10, no. 1, pp. 1–7, 2019.

[168] M. P. Landry, H. Ando, A. Y. Chen, J. Cao, V. I. Kottadiel, L. Chio,

D. Yang, J. Dong, T. K. Lu, and M. S. Strano, "Single-molecule detection of protein efflux from microorganisms using fluorescent single-walled carbon nanotube sensor arrays," *Nature Nanotechnology*, vol. 12, no. 4, pp. 368–377, 2017.

[169] A. Goldoni, L. Petaccia, S. Lizzit, and R. Larciprete, "Sensing gases with carbon nanotubes: a review of the actual situation," *Journal of Physics: Condensed Matter*, vol. 22, no. 1, p. 013001, 2009.

[170] J. Kong, M. G. Chapline, and H. Dai, "Functionalized carbon nanotubes for molecular hydrogen sensors," *Advanced Materials*, vol. 13, no. 18, pp. 1384–1386, 2001.

[171] S. Chopra, K. McGuire, N. Gothard, A. Rao, and A. Pham, "Selective gas detection using a carbon nanotube sensor," *Applied Physics Letters*, vol. 83, no. 11, pp. 2280–2282, 2003.

[172] S. Hong and S. Myung, "A flexible approach to mobility," *Nature Nanotechnology*, vol. 2, no. 4, pp. 207–208, 2007.

[173] A. Elkadi, E. Decrossas, S.-Q. Yu, H. A. Naseem, and S. M. El-Ghazaly, "Controlling the energy band gap of aligned semiconducting single-walled carbon nanotubes for thz modulator," in *2012 7th European Microwave Integrated Circuit Conference*, pp. 270–273, IEEE, 2012.

[174] M. S. Dresselhaus, G. Dresselhaus, and P. C. Eklund, *Science of fullerenes and carbon nanotubes: their properties and applications*. Elsevier, 1996.

[175] L. Valentini, I. Armentano, D. Puglia, L. Lozzi, S. Santucci, and J. Kenny, "A deeper understanding of the photodesorption mechanism of aligned carbon nanotube thin films by impedance spectroscopy," *Thin Solid Films*, vol. 449, no. 1-2, pp. 105–112, 2004.

[176] S. Ghosh, S. M. Bachilo, R. A. Simonette, K. M. Beckingham, and R. B. Weisman, "Oxygen doping modifies near-infrared band gaps in fluorescent Single-Walled Carbon Nanotubes," *Science*, vol. 330, no. 6011, pp. 1656–1659, 2010.

[177] C. Qidao, D. Liming, G. Mei, H. Shaoming, and M. Albert, "Plasma activation of carbon nanotubes for chemical modification," *The Journal of Physical Chemistry B*, vol. 105, no. 3, pp. 618–622, 2001. doi: 10.1021/jp003385g.

[178] G. Sun, J. Kürti, M. Kertesz, and R. H. Baughman, "Variations of the geometries and band gaps of single-walled carbon nanotubes and the effect of charge injection," *The Journal of Physical Chemistry B*, vol. 107, no. 29, pp. 6924–6931, 2003.

[179] Y. Matsuda, J. Tahir-Kheli, and W. A. Goddard III, "Definitive band gaps for single-wall carbon nanotubes," *The Journal of Physical Chemistry Letters*, vol. 1, no. 19, pp. 2946–2950, 2010.

[180] J. Li, Y. Lu, Q. Ye, M. Cinke, J. Han, and M. Meyyappan, "Carbon nanotube sensors for gas and organic vapor detection," *Nano letters*, vol. 3, no. 7, pp. 929–933, 2003.

[181] A. Zahab, L. Spina, P. Poncharal, and C. Marliere, "Water-vapor effect on the electrical conductivity of a single-walled carbon nanotube mat," *Physical Review B*, vol. 62, no. 15, p. 10000, 2000.

[182] J. Wang, W. Jiang, B. Wang, Y. Gao, Z. Wang, and R.-Q. Zhang, "Chirality dependent spin polarization of carbon nanotubes," *New Journal of Physics*, vol. 18, no. 2, p. 023029, 2016.

[183] C.-K. Yang, J. Zhao, and J. P. Lu, "Complete spin polarization for a carbon nanotube with an adsorbed atomic transition-metal chain," *Nano Letters*, vol. 4, no. 4, pp. 561–563, 2004.

[184] N. B. Singh, B. Bhattacharya, and U. Sarkar, "Nickel decorated single-wall carbon nanotube as CO sensor," *Soft Nanoscience Letters*, vol. 3, no. 04, p. 9, 2013.

[185] U. Innovate, "Epsrc. a roadmap for quantum technologies in the uk," *Policy Paper*, 2015.

[186] "Sensing devices." `http://www.nist.gov/pml/electromagnetics/grp08/sensors.cfm`.

[187] J. Kitching, S. Knappe, and E. A. Donley, "Atomic sensors–a review," *IEEE Sensors Journal*, vol. 11, no. 9, pp. 1749–1758, 2011.

[188] C. Bonato, M. S. Blok, H. T. Dinani, D. W. Berry, M. L. Markham, D. J. Twitchen, and R. Hanson, "Optimized quantum sensing with a single

electron spin using real-time adaptive measurements," *Nature Nanotechnology*, vol. 11, no. 3, pp. 247–252, 2016.

[189] J. Maze, J. Taylor, and M. Lukin, "Electron spin decoherence of single nitrogen-vacancy defects in diamond," *Physical Review B*, vol. 78, no. 9, p. 094303, 2008.

[190] D. Toyli, D. Christle, A. Alkauskas, B. Buckley, C. Van de Walle, and D. Awschalom, "Measurement and control of single nitrogen-vacancy center spins above 600 k," *Physical Review X*, vol. 2, no. 3, p. 031001, 2012.

[191] A. Cooper, E. Magesan, H. Yum, and P. Cappellaro, "Time-resolved magnetic sensing with electronic spins in diamond," *Nature communications*, vol. 5, no. 1, pp. 1–7, 2014.

[192] T. D. Ladd, F. Jelezko, R. Laflamme, Y. Nakamura, C. Monroe, and J. L. OBrien, "Quantum computers," *Nature*, vol. 464, no. 7285, pp. 45–53, 2010.

[193] L. Rondin, J.-P. Tetienne, T. Hingant, J.-F. Roch, P. Maletinsky, and V. Jacques, "Magnetometry with nitrogen-vacancy defects in diamond," *Reports on Progress in Physics*, vol. 77, no. 5, p. 056503, 2014.

[194] F. Dolde, H. Fedder, M. W. Doherty, T. Nobauer, F. Rempp, G. Balasubramanian, T. Wolf, F. Reinhard, L. C. Hollenberg, F. Jelezko, *et al.*,

"Electric-field sensing using single diamond spins," *Nature Physics*, vol. 7, no. 6, pp. 459–463, 2011.

[195] V. M. Acosta, E. Bauch, M. P. Ledbetter, A. Waxman, L.-S. Bouchard, and D. Budker, "Temperature dependence of the nitrogen-vacancy magnetic resonance in diamond," *Physical Review Letters*, vol. 104, no. 7, p. 070801, 2010.

[196] P. Ovartchaiyapong, K. W. Lee, B. A. Myers, and A. C. B. Jayich, "Dynamic strain-mediated coupling of a single diamond spin to a mechanical resonator," *Nature Communications*, vol. 5, no. 1, pp. 1–6, 2014.

[197] E. Lewars, "Computational chemistry," *Introduction to the theory and applications of molecular and quantum mechanics*, p. 318, 2011.

[198] M. L. Klein and W. Shinoda, "Large-Scale Molecular Dynamics Simulations of Self-Assembling Systems," *Science*, vol. 321, no. 5890, pp. 798–800, 2008.

[199] D. Marx and J. Hutter in *Ab Initio Molecular Dynamics*, Cambridge University Press, 2009.

[200] X. Andrade, A. Castro, D. Zueco, J. Alonso, P. Echenique, F. Falceto, and A. Rubio, "Modified ehrenfest formalism for efficient large-scale ab initio molecular dynamics," *Journal of Chemical Theory and Computation*, vol. 5, no. 4, pp. 728–742, 2009.

[201] P. Grochowski and B. Lesyng, "Extended Hellmann–Feynman forces, canonical representations, and exponential propagators in the mixed quantum-classical molecular dynamics," *The Journal of Chemical Physics*, vol. 119, no. 22, pp. 11541–11555, 2003.

[202] E. P. Fahrenthold, "Nonholonomic Formulation of Ab Initio Molecular Dynamics," *Journal of Engineering Materials and Technology*, vol. 139, no. 3, p. 034501, 2017.

[203] J. Koo and E. Fahrenthold, "Discrete Hamilton's equations for arbitrary Lagrangian–Eulerian dynamics of viscous compressible flow," *Computer Methods in Applied Mechanics and Engineering*, vol. 189, no. 3, pp. 875–900, 2000.

[204] Y.-K. Park and E. P. Fahrenthold, "A kernel free particle-finite element method for hypervelocity impact simulation," *International Journal for Numerical Methods in Engineering*, vol. 63, no. 5, pp. 737–759, 2005.

[205] R. J. Rabb and E. P. Fahrenthold, "Impact dynamics simulation for multilayer fabrics," *International Journal for Numerical Methods in Engineering*, vol. 83, no. 5, pp. 537–557, 2010.

[206] J. Zhang *et al.*, *Computational design of gas phase explosive sensors*. PhD thesis, 2020.

[207] J. Bendall, A. Ilie, M. Welland, J. Sloan, and M. Green, "Thermal stability and reactivity of metal halide filled single-walled carbon nanotubes,"

The Journal of Physical Chemistry B, vol. 110, no. 13, pp. 6569–6573, 2006.

[208] J. Hansson, A. Nylander, M. Flygare, K. Svensson, L. Ye, T. Nilsson, Y. Fu, and J. Liu, "Effects of high temperature treatment of carbon nanotube arrays on graphite: increased crystallinity, anchoring and intertube bonding," *Nanotechnology*, vol. 31, no. 45, p. 455708, 2020.

[209] Z. Luo, A. Oki, L. Carson, L. Adams, G. Neelgund, N. Soboyejo, G. Regisford, M. Stewart, K. Hibbert, G. Beharie, *et al.*, "Thermal stability of functionalized carbon nanotubes studied by in situ transmission electron microscopy," *Chemical physics letters*, vol. 513, no. 1-3, pp. 88–93, 2011.

[210] P. G. Collins, "Defects and disorder in carbon nanotubes," *Oxford University Press: Oxford*, 2010.

[211] A. Choudhury and P. Kar, "Doping effect of carboxylic acid group functionalized multi-walled carbon nanotube on polyaniline," *Composites Part B: Engineering*, vol. 42, no. 6, pp. 1641–1647, 2011.

[212] M. Dion, H. Rydberg, E. Schroder, D. C. Langreth, and B. I. Lundqvist, "Van der Waals density functional for general geometries," *Physical review letters*, vol. 92, no. 24, p. 246401, 2004.

[213] S. Grimme, "Accurate description of van der Waals complexes by density functional theory including empirical corrections," *Journal of Computational Chemistry*, vol. 25, no. 12, pp. 1463–1473, 2004.

[214] T. Tsuzuki, S. Ogata, and M. Uranagase, "Large-scale DFT simulation of quinone molecules encapsulated in single-walled carbon nanotube for novel Li-ion battery cathode," *Computational Materials Science*, vol. 171, p. 109281, 2020.

[215] B. Akgenc, "Intriguing of two-dimensional Janus surface-functionalized MXenes: An ab initio calculation," *Computational Materials Science*, vol. 171, p. 109231, 2020.

[216] S. Grimme, "Semiempirical GGA-type density functional constructed with a long-range dispersion correction," *Journal of Computational Chemistry*, vol. 27, no. 15, pp. 1787–1799, 2006.

[217] D. Langreth, B. I. Lundqvist, S. D. Chakarova-Kack, V. Cooper, M. Dion, P. Hyldgaard, A. Kelkkanen, J. Kleis, L. Kong, S. Li, *et al.*, "A density functional for sparse matter," *Journal of Physics: Condensed Matter*, vol. 21, no. 8, p. 084203, 2009.

[218] K. Berland and P. Hyldgaard, "Structure and binding in crystals of cagelike molecules: Hexamine and platonic hydrocarbons," *The Journal of Chemical Physics*, vol. 132, no. 13, p. 134705, 2010.

[219] K. Berland and P. Hyldgaard, "Analysis of van der Waals density functional components: Binding and corrugation of benzene and C 60 on boron nitride and graphene," *Physical Review B*, vol. 87, no. 20, p. 205421, 2013.

[220] L. Sutton, *Tables of interatomic distances and configuration in molecules and ions*. No. 11, Chemical Society, 1965.

[221] P. Saxena, *Chemistry of interhalogen compounds*. Discovery Publishing House, 2007.

[222] F. Lovas, E. Tiemann, J. Coursey, S. Kotochigova, J. Chang, K. Olsen, and R. Dragoset, "Diatomic Spectral Database, NIST Standard Reference Database 114," 2005.

Vita

Manasi Doshi hails from the town of Junagadh in India. She graduated with her Bachelors degree in Mechanical Engineering in May 2016 from Nirma University. In the Fall of 2016, she started her PhD studies in Mechanical Engineering at the University of Texas at Austin.

Permanent address: Paritosh, 107 Raijinagar, Junagadh, Gujarat, India

This dissertation was typeset with LaTeX[†] by the author.

[†]LaTeX is a document preparation system developed by Leslie Lamport as a special version of Donald Knuth's TeX Program.